Analysis of B Meson Decays to Three Charged Pions

Yao Li

Dissertation submitted to the Faculty of the
Virginia Polytechnic Institute and State University
in partial fulfillment of the requirements for the degree of

Doctor of Philosophy
in
Physics

Leo E. Piilonen, Chair
Jonathan M. Link
Eric R. Sharpe
Jean J. Heremans

November 12, 2015
Blacksburg, Virginia

Keywords: Particle Physics, B Mesons Decay, CP Violation

Analysis of B Meson Decays to Three Charged Pions

Yao Li

ABSTRACT

Decays of B mesons to three-body charmless final states probe the properties of the weak interaction through their dependence on the complex quark couplings in the CKM matrix. They also test dynamical models for hadronic B decays. Based on a sample of 772×10^6 $B\bar{B}$ pairs collected by the Belle experiment at $\sqrt{s} = 10.58$ GeV, we present a study of direct CP violation in $B^\pm \to \pi^\pm\pi^+\pi^-$. The measured branching fraction ($\mathcal{B}$) and CP asymmetry value ($\mathcal{A}_{CP}$) are

$$\mathcal{B}(B^\pm \to \pi^\pm\pi^+\pi^-) = \left(18.9^{+5.1}_{-4.5} \pm 1.7\right) \times 10^{-6},$$

$$\mathcal{A}_{CP}(B^\pm \to \pi^\pm\pi^+\pi^-) = -0.10^{+0.27}_{-0.24} \pm 0.02,$$

where the first error on each value is statistical and the second is systematic.

This work received support from the Department of Energy (United States) and High Energy Accelerator Research Organization (Japan).

Acknowledgments

First of all, I would like to express my sincere gratitude to my advisor Professor Leo Piilonen for the support of my Ph.D research, for his patience, kindness, and immense knowledge.

Besides my advisor, I would like to thank the rest of my thesis committee: Dr. Jonathan Link, Dr. Eric Sharpe, and Dr. Jean Heremans, for their insightful comments and encouragement.

I would like to thank all the members of Belle Collaboration for their support and cooperation, especially Dr. Nakao Mikihiko, Dr. Yuuji Unno , Dr. Shohei Nishida , Dr. Junji Haba, Dr. Yoshihide Sakai , Dr. Eunil Won, Dr. Alexey Garmash, Dr. Marko Petric, and Dr. Paoti Chang. It was my great pleasure to work with the diligent and intelligent colleagues in HBD group, and many thanks to the conveners Dr. Tom Browder and Dr. Mohanty Gagan.

I am heartily thankful to Dr. Debabrata Mohapatra, who provided a lot of support and advice at the beginning of this project. I am particularly grateful for the assistance given by Dr. Xiaolong Wang, who always helped me when I met obstacles in the research.

Last but not the least, I would like to thank my parents and my wife Yanjie for their spiritual support, love, and understanding.

Contents

List of Figures

List of Tables

Chapter 1

Introduction

In this chapter, we review the theory and motivation for the study of charged B mesons decay. This is important for understanding the validity of the Standard Model (SM) [1] and may provide evidence for new physics beyond the Standard Model.

1.1 CKM Matrix

The masses and mixings of quarks have a common origin in the Standard Model. They arise from the contributions to the SM Lagrangian due to their Yukawa interactions with the Higgs condensate,

$$\mathcal{L}_Y = -Y^d_{ij}\overline{Q^I_{Li}}\phi d^I_{Rj} - Y^u_{ij}\overline{Q^I_{Li}}\epsilon\phi^* u^I_{Rj} + \text{h.c.}, \tag{1.1}$$

where h.c. means Hermitian conjugation, $Y^{u,d}$ are 3×3 complex matrices, ϕ is the Higgs field, $i,\ j \in \{1,\ 2,\ 3\}$ are generation indices, ϵ is the 2×2 antisymmetric tensor, Q^I_L are left-handed quark doublets, and d^I_R and u^I_R are right-handed down- and up-type quark singlets, respectively, in the weak-eigenstate basis. The physical states are obtained by diagonalizing $Y^{u,d}$ by four unitary matrices, $V^{u,d}_{L,R}$, as $M^f_{\text{diag}} = V^f_L Y^f V^{f\dagger}_R (v/\sqrt{2})$, where $f = u, d$. As a result, charged-current $W^\pm$ interactions couple to the physical u_{Lj} and d_{Lk} quarks with couplings

given by

$$\frac{-g}{\sqrt{2}}(\overline{u_L},\overline{c_L},\overline{t_L})\gamma^\mu W^+_\mu V_{\rm CKM}\begin{pmatrix} d_L \\ s_L \\ b_L \end{pmatrix} + \text{h.c.}, \tag{1.2}$$

where

$$V_{\rm CKM} \equiv V_L^u V_L^{d\dagger} = \begin{pmatrix} V_{ud} & V_{us} & V_{ub} \\ V_{cd} & V_{cs} & V_{cb} \\ V_{td} & V_{ts} & V_{tb} \end{pmatrix} \tag{1.3}$$

This Cabibbo-Kobayashi-Maskawa (CKM) matrix [2] is a 3×3 unitary matrix. It can be parameterized by three mixing angles and the CP-violating KM phase [3]. A standard choice of many possible conventions is [4]

$$V_{\rm CKM} = \begin{pmatrix} c_{12}c_{13} & s_{12}c_{13} & s_{13}e^{-i\delta} \\ -s_{12}c_{23} - c_{12}s_{23}s_{13}e^{i\delta} & c_{12}c_{23} - s_{12}s_{23}s_{13}e^{i\delta} & s_{23}c_{13} \\ s_{12}s_{23} - c_{12}c_{23}s_{13}e^{i\delta} & -c_{12}s_{23} - s_{12}c_{23}s_{13}e^{i\delta} & c_{23}c_{13} \end{pmatrix} \tag{1.4}$$

where $s_{ij} = \sin\theta_{ij}$, $c_{ij} = \cos\theta_{ij}$, and δ is the phase responsible for all CP-violating phenomena in flavor-changing processes in the SM. Since $s_{13} \ll s_{23} \ll s_{12} \ll 1$ from many experiments, it is convenient to exhibit this hierarchy using the Wolfenstein parameterization by defining [5, 6, 7]:

$$\begin{aligned} s_{12} = \lambda = \frac{|V_{us}|}{\sqrt{|V_{ud}|^2 + |V_{us}|^2}}, \quad s_{23} = A\lambda^2 = \lambda\left|\frac{V_{cb}}{V_{us}}\right|, \\ s_{13}e^{i\delta} = V_{ub}^* = A\lambda^3(\rho + i\eta) = \frac{A\lambda^3(\bar\rho + i\bar\eta)\sqrt{1 - A^2\lambda^4}}{\sqrt{1-\lambda^2}[1 - A^2\lambda^4(\bar\rho + i\bar\eta)]}. \end{aligned} \tag{1.5}$$

$V_{\rm CKM}$ can be written to $\mathcal{O}(\lambda^4)$ as

$$V_{\rm CKM} = \begin{pmatrix} 1 - \lambda^2/2 & \lambda & A\lambda^3(\rho - i\eta) \\ -\lambda & 1 - \lambda^2/2 & A\lambda^2 \\ A\lambda^3(1 - \rho - i\eta) & -A\lambda^2 & 1 \end{pmatrix} + \mathcal{O}(\lambda^4) \tag{1.6}$$

The unitarity of the CKM matrix imposes $\sum_i V_{ij}V_{ik}^* = \delta_{jk}$. The six vanishing combinations can be represented as triangles in the complex plane, of which the ones obtained

by taking scalar products of neighboring rows or columns are nearly degenerate. The most commonly used unitarity triangle arises from

$$V_{ud}V_{ub}^* + V_{cd}V_{cb}^* + V_{td}V_{tb}^* = 0 \tag{1.7}$$

by dividing each side by the best-known value, $V_{cd}V_{cb}^*$ (see FIG 1.1). Its vertices are exactly (0,0), (1,0), and $(\bar{\rho}, \bar{\eta})$. An important goal of flavor physics is to overconstrain the CKM elements, and many measurements can be conveniently displayed and compared in the $\bar{\rho}$, $\bar{\eta}$ plane. The angles of the unitarity triangle are

$$\phi_1 = \arg\left(-\frac{V_{cd}V_{cb}^*}{V_{td}V_{tb}^*}\right), \quad \phi_2 = \arg\left(-\frac{V_{td}V_{tb}^*}{V_{ud}V_{ub}^*}\right), \quad \phi_3 = \arg\left(-\frac{V_{ud}V_{ub}^*}{V_{cd}V_{cb}^*}\right) \tag{1.8}$$

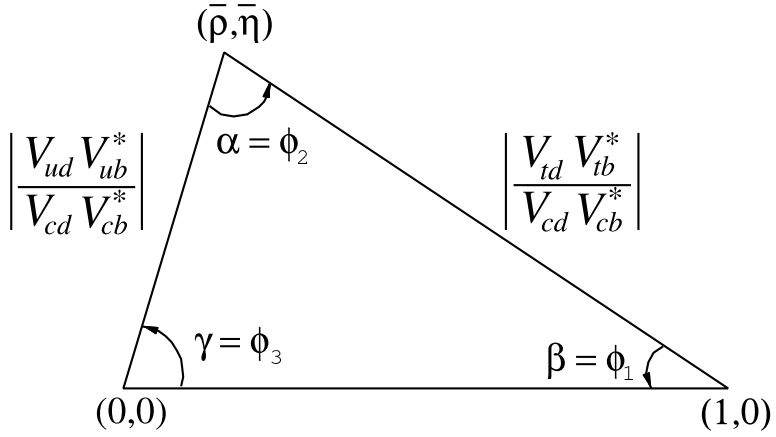

Figure 1.1: Sketch of the unitarity triangle

The CKM matrix elements can be most precisely determined using a global fit to all available measurements and imposing the SM constraints such as three-generation unitarity. The fit must also use theory predictions for hadronic matrix elements, some of which have significant uncertainties. There are several approaches to combining the experimental data. CKMfitter [7, 8] and Ref. [9] use frequentist statistics, while UTfit [10, 11] uses a Bayesian approach. The constraints implied by the unitarity of the three-generation CKM matrix significantly reduce the allowed range of some of the CKM elements. The fit for the Wolfenstein

parameters using the method of Ref [7, 8] gives

$$\begin{aligned} \lambda &= 0.22537 \pm 0.00061, \quad A = 0.814^{+0.023}_{-0.024}, \\ \bar{\rho} &= 0.117 \pm 0.021, \quad \bar{\eta} = 0.353 \pm 0.013. \end{aligned} \tag{1.9}$$

The fit results for the magnitudes of all nine CKM elements are

$$\begin{pmatrix} |V_{ud}| & |V_{us}| & |V_{ub}| \\ |V_{cd}| & |V_{cs}| & |V_{cb}| \\ |V_{td}| & |V_{ts}| & |V_{tb}| \end{pmatrix} = \begin{pmatrix} 0.97427 \pm 0.00014 & 0.22536 \pm 0.00061 & 0.00355 \pm 0.00015 \\ 0.22522 \pm 0.00061 & 0.97343 \pm 0.00015 & 0.0414 \pm 0.0012 \\ 0.00886^{+0.00033}_{-0.00032} & 0.0405^{+0.0011}_{-0.0012} & 0.99914 \pm 0.00005 \end{pmatrix} \tag{1.10}$$

The constraints on the apex of the unitarity triangle in the $\bar{\rho}, \bar{\eta}$ plane from various measurements and the global fit result are shown in FIG 1.2. The shaded 95% CL regions all overlap consistently around the global fit region. Most of the constraints come from measurements at the B factories.

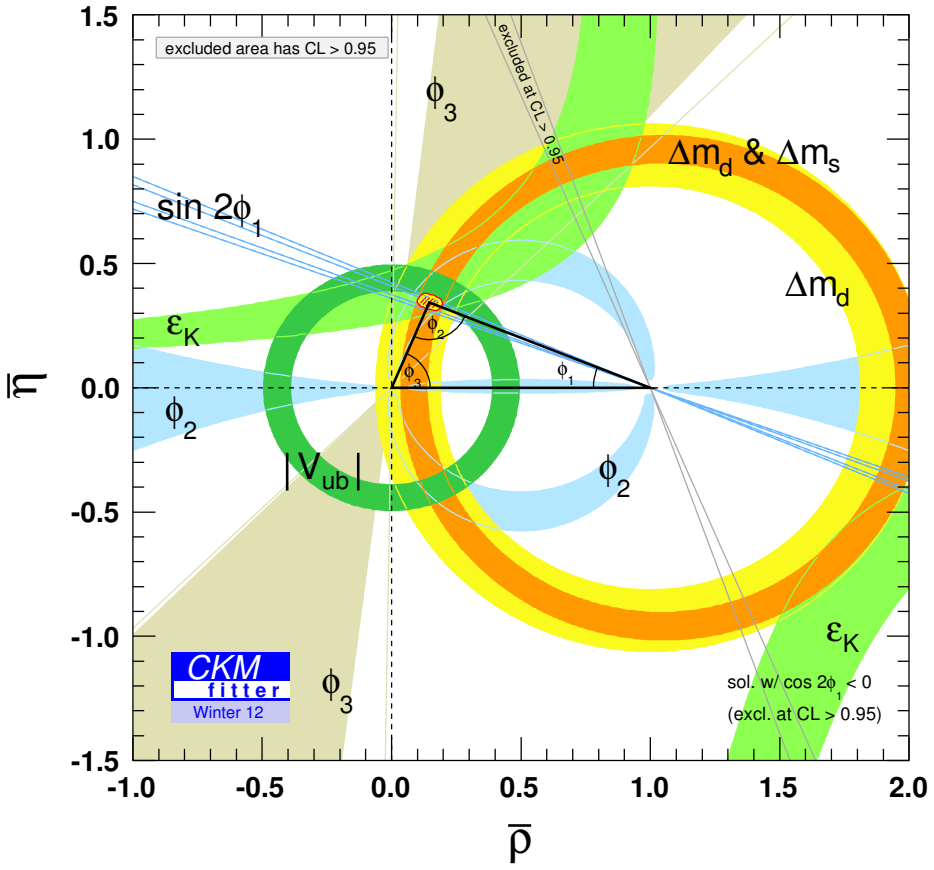

Figure 1.2: Constraints on the $\bar{\rho}$ and $\bar{\eta}$ in the Wolfenstein parameterization of the CKM matrix. [7]

1.2 CP Violation

The CP transformation combines charge conjugation C with parity P, where C transforms a particle into its antiparticle ($Q \to -Q$) and P reverses the spatial coordinates ($\vec{x} \to -\vec{x}$). The laws of nature would be the same for matter and antimatter if CP were exactly symmetric. Most phenomena are C- and P-symmetric, and therefore, also CP-symmetric. These symmetries are respected by the gravitational, electromagnetic, and strong interactions, but

not by the weak interaction. Although the weak interactions violate C and P separately, CP is still preserved in most weak interaction processes except in certain rare cases, such as B decays, that we study in this thesis. Within the Standard Model, CP symmetry is broken by the complex phase in the CKM matrix described in the previous section [3], which agrees with all measurements to date. Hadron decays via the weak interaction probe inter-generational flavor-changing CP violation and provide additional constraints on the flavor parameters of the Standard Model.

For charged hadron decays, the decay amplitudes of initial state M and its CP conjugate $\bar{M}$ to a multi-particle final state f and its CP conjugate $\bar{f}$ are

$$\begin{aligned} A_f &= \langle f|\mathcal{H}|M\rangle, \quad \bar{A}_f = \langle f|\mathcal{H}|\bar{M}\rangle, \\ A_{\bar{f}} &= \langle \bar{f}|\mathcal{H}|M\rangle, \quad \bar{A}_{\bar{f}} = \langle \bar{f}|\mathcal{H}|\bar{M}\rangle, \end{aligned} \tag{1.11}$$

where $\mathcal{H}$ is the Hamiltonian for weak interactions.

There are two types of phases that may appear in the decay amplitudes. Complex parameters in any Lagrangian term that contributes to the amplitude will appear in complex conjugate form in the CP-conjugate amplitude. Thus, their phases appear in A_f and $\bar{A}_{\bar{f}}$ with opposite signs. In the Standard Model, these phases occur only in the couplings of the $W^{\pm}$ bosons, and hence are called weak phases. A second type of phase can appear in scattering or decay amplitudes and it originates from the possible contribution from intermediate on-shell states in the decay process. Since these phases are generated by CP-invariant interactions, they are the same in A_f and $\bar{A}_{\bar{f}}$. Since the dominant rescattering is usually from strong interactions, the shifts are called strong phases. One can write each contribution a_i to A_f in three parts: its magnitude $|a_i|$, its weak phase ϕ_i, and its strong phase δ_i. For example, if there are two contributions, $A_f = a_1 + a_2$, then

$$\begin{aligned} A_f &= |a_1|e^{i(\delta_1+\phi_1)} + |a_2|e^{i(\delta_2+\phi_2)}, \\ \bar{A}_{\bar{f}} &= |a_1|e^{i(\delta_1-\phi_1)} + |a_2|e^{i(\delta_2-\phi_2)}, \end{aligned} \tag{1.12}$$

The CP asymmetry for charged hadron decays is defined as

$$\mathcal{A}_{f^\pm} \equiv \frac{\Gamma(M^- \to f^-) - \Gamma(M^+ \to f^+)}{\Gamma(M^- \to f^-) + \Gamma(M^+ \to f^+)} = \frac{|\bar{A}_{f^-}/A_{f^+}|^2 - 1}{|\bar{A}_{f^-}/A_{f^+}|^2 + 1}; \tag{1.13}$$

then, in the above example,

$$\mathcal{A}_f = -\frac{2|a_1 a_2| \sin(\delta_2 - \delta_1) \sin(\phi_2 - \phi_1)}{|a_1|^2 + |a_2|^2 + 2|a_1 a_2| \cos(\delta_2 - \delta_1) \cos(\phi_2 - \phi_1)} \tag{1.14}$$

To extract the weak phase difference $\phi_2 - \phi_1$ from the asymmetry, it is necessary to know the amplitude ratio $|a_1/a_2|$ and the strong phase difference $\delta_2 - \delta_1$. Both quantities depend on non-perturbative hadronic parameters that are difficult to calculate, but in some cases can be obtained from experiment.

1.3 The Decay Mode $B^\pm \to \pi^\pm\pi^+\pi^-$

The decays of B mesons to three body charmless final states offer the possibility for investigating the properties of the weak interaction by providing information on the complex quark couplings encoded in the CKM matrix elements [12]. Furthermore, such decays are useful to test phenomenological models of hadronic decays. Measurements of direct CP violation asymmetries and constraints on the magnitudes and the phases of the CKM matrix elements can be obtained from individual decay channels in $B^\pm \to \pi^\pm\pi^\pm\pi^\mp$ that are dominated by decays through intermediate resonances. Studies of $B^\pm \to \pi^\pm\pi^\pm\pi^\mp$ are also important to help towards the precise measurement of CKM unitarity-triangle angle ϕ_2. Moreover, a full Dalitz plot analysis of $B^\pm \to \pi^\pm\pi^\pm\pi^\mp$ allows us to check for effects from the interference of resonant and non-resonant contributions. It is particularly important to limit the possible effects of broad scalar structures and non-resonant contributions. Further knowledge about the presence or absence of these structures in $B^\pm \to \pi^\pm\pi^\pm\pi^\mp$ decays would be useful to understand their nature and involvement in these and other related hadronic B decays.

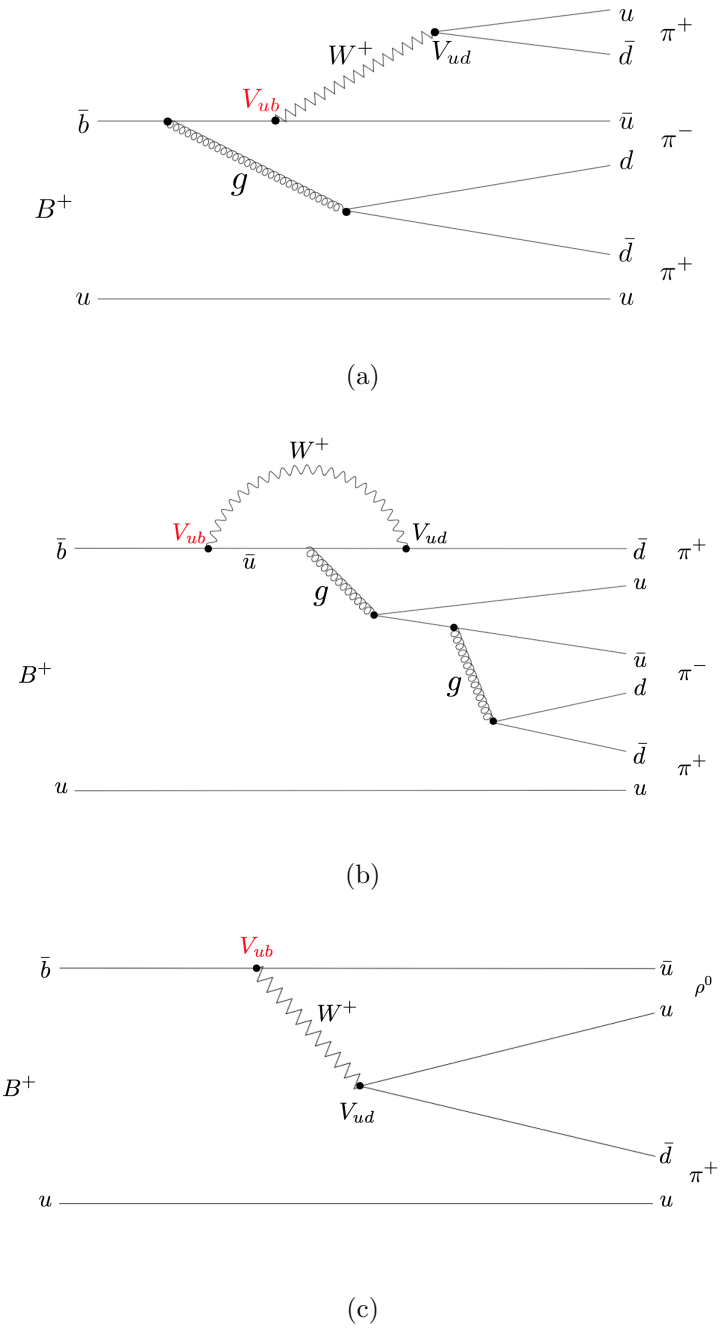

Figure 1.3: Examples of Feynman tree (a), penguin (b), and resonance (c) diagrams for the decay $B^+ \to \pi^+\pi^-\pi^+$. The resonance state (ρ^0 in this example) can decay to $\pi^+\pi^-$ via the strong or weak process.

1.4 Dalitz Plot for Three-body Decays

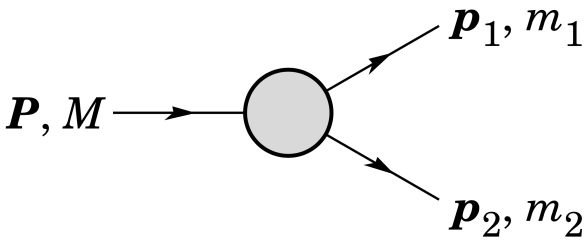

Figure 1.4: Definitions of variables for three-body decays.

For a given three-body decay as shown in FIG 1.4, we define

$$\begin{aligned} p_{ij} &= p_i + p_j \\ m_{ij}^2 &= p_{ij}^2; \end{aligned} \tag{1.15}$$

then

$$\begin{aligned} m_{12}^2 + m_{23}^2 + m_{13}^2 &= M^2 + m_1^2 + m_2^2 + m_3^2 \\ m_{12}^2 = (P - p_3)^2 &= M^2 + m_3^2 - 2ME_3, \end{aligned} \tag{1.16}$$

where E_3 is the energy of particle 3 in the rest frame of M. In the decay of a scalar B meson, the decay ratio is [1]

$$d\Gamma = \frac{1}{(2\pi)^3}\frac{1}{32M^3}\overline{|\mathcal{M}|^2}dm_{12}^2 dm_{23}^2 \tag{1.17}$$

where $\mathcal{M}$ is the invariant matrix element in the S-matrix [13]. For a given value of m_{12}^2, the range of m_{23}^2 is determined by its value when $\mathbf{p}_2$ is parallel or antiparallel to $\mathbf{p}_3$:

$$\begin{aligned} (m_{23}^2)_{\max} &= (E_2^* + E_3^*)^2 - \left(\sqrt{E_2^{*2} - m_2^2} - \sqrt{E_3^{*2} - m_2^3}\right)^2, \\ (m_{23}^2)_{\min} &= (E_2^* + E_3^*)^2 - \left(\sqrt{E_2^{*2} - m_2^2} + \sqrt{E_3^{*2} - m_2^3}\right)^2, \end{aligned} \tag{1.18}$$

where $E_2^* = (m_{12}^2 - m_1^2 + m_2^2)/2m_{12}$ and $E_3^* = (M - m_{12}^2 - m_3^2)/2m_{12}$ are the energies of particles 2 and 3 in the m_{12} rest frame. The two-dimensional distribution in m_{12}^2 and m_{23}^3 is

called a Dalitz plot [14]. If $\overline{|\mathcal{M}|^2}$ is constant, the allowed region of the plot will be uniformly populated with events. A non-uniformity in the plot gives immediate information on $|\mathcal{M}|^2$. For example, in the case of $B^+ \to \pi^+\pi^-\pi^+$, bands appear near $m_{\pi^+\pi^-} \simeq m_{\rho^0(770)}$, reflecting the appearance of the decay chain $B^+ \to \rho^0(770)\pi^+ \to \pi^+\pi^-\pi^+$.

Chapter 2

The Belle Experiment

The Belle experiment is conducted by the Belle Collaboration, including more than four hundred physicists investigating CP violation effects at the High Energy Accelerator Research Organization (KEK) in Tsukuba, Japan. In this chapter, we introduce the hardware and software in Belle [15, 16, 17, 18].

2.1 Production of $\Upsilon(4S)$

The Υ meson is a bound state of $b\bar{b}$ quarks with $J^{PC} = 1^{--}$, where J, P, C are spin, parity, and charge conjugation quantum numbers, respectively. The first observation of $\Upsilon(1S)$ was from proton-nucleon collisions by the CFS Collaboration in 1977 [19]. The experiments at the CESR and DORIS accelerator facilities confirmed the existence of Υ and measured its excited states. FIG 2.1 shows the e^+e^- hadronic cross section as a function of the center of mass energy [20].

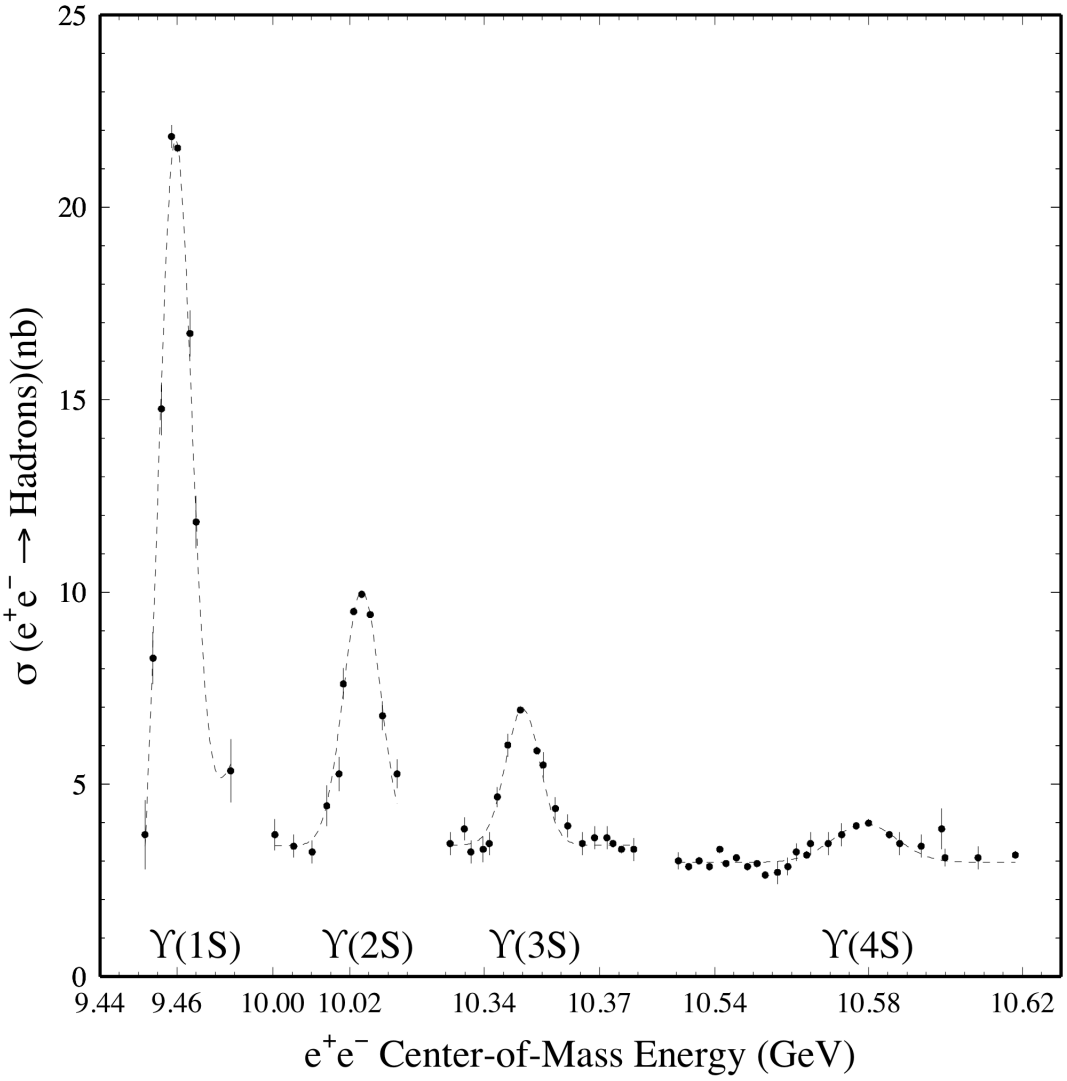

Figure 2.1: e^+e^- cross section in the invariant mass range 9.44 - 10.62 GeV/c^2

The energy of the $n = 4$ radial excitation $\Upsilon(4S)$ is 10579.4 ± 1.2 MeV, which is approximately 20 MeV above the threshold for $B\bar{B}$ production [1]. More than 96% of $\Upsilon(4S)$ mesons decay into the $B\bar{B}$ state, including $51.4 \pm 0.6\%$ as B^+B^- pairs and $48.6 \pm 0.6\%$ as $B^0\bar{B}^0$ pairs. In addition to the excited $\Upsilon(4S)$ state, the e^+e^- collision and annihilation also produces non-resonant hadronic states via $e^+e^- \to q\bar{q}$ ($q = u, d, s, c$), which is referred as "continuum", as well as lepton-pair final states $\ell^+\ell^-(\gamma)$. The relative rates are $uds : c\bar{c} : b\bar{b} : \tau^+\tau^- : \mu^+\mu^- : e^+e^- = 2.1 : 1.3 : 1.1 : 0.9 : 1.0 : 123.5$ (the e^+e^- production

being mainly from Bhabha events, with only 1% of them recorded by a pre-scaling factor in the trigger [21]), so the cross section of $\Upsilon(4S)$ production is roughly 1/3 that of the continuum. One other production mechanism is the two-photon collision, $e^+e^- \to e^+e^-X$, where X is a leptonic or hadronic final state produced by the interaction of two virtual photons.

2.2 The KEKB Accelerator

The KEKB collider, located at the KEK laboratory in Tsukuba, Japan, is shown schematically in FIG 2.2. The accelerated electrons and positrons, with respective energies of 8 and 3.5 GeV, are contained in the "High Energy Ring" (HER) and the "Low Energy Ring" (LER), respectively [22]. Each ring is 3.016 km in circumference and located 11 meters underground. The electrons and positrons attain their designated energy by the linear accelerator (LINAC) and are injected into KEKB in the Fuji area. The two storage rings intersect at the interaction point (IP) in the Belle detector located in Tsukuba Hall. Another cross-over of the two rings occurs at the Fuji area to ensure the same circumference. Several radio-frequency (RF) cavities are installed at the Fuji, Nikko, and Oho areas to compensate for synchrotron energy reduction of the beam caused by the radiation as it circulates. To reduce the amount of such radiation in the Belle detector, the two beams travel in the straight lines and collide at a crossing angle of ± 11 mrad rather than being bent into head-on collisions by a permanent dipole magnet inside the detector (as is done in BaBar). The center-of-mass energy of the two beams is tuned to the mass of the $\Upsilon(4S)$ meson [1]:

$$\sqrt{s} = 2\sqrt{E_{\rm HER}E_{\rm LER}} = 10.58 \text{ GeV} \tag{2.1}$$

The asymmetric energy of the positron and electron beams cause the boost of the $\Upsilon(4S)$:

$$\beta\gamma = \frac{E_{\rm HER} - E_{\rm LER}}{\sqrt{s}} = 0.425 \tag{2.2}$$

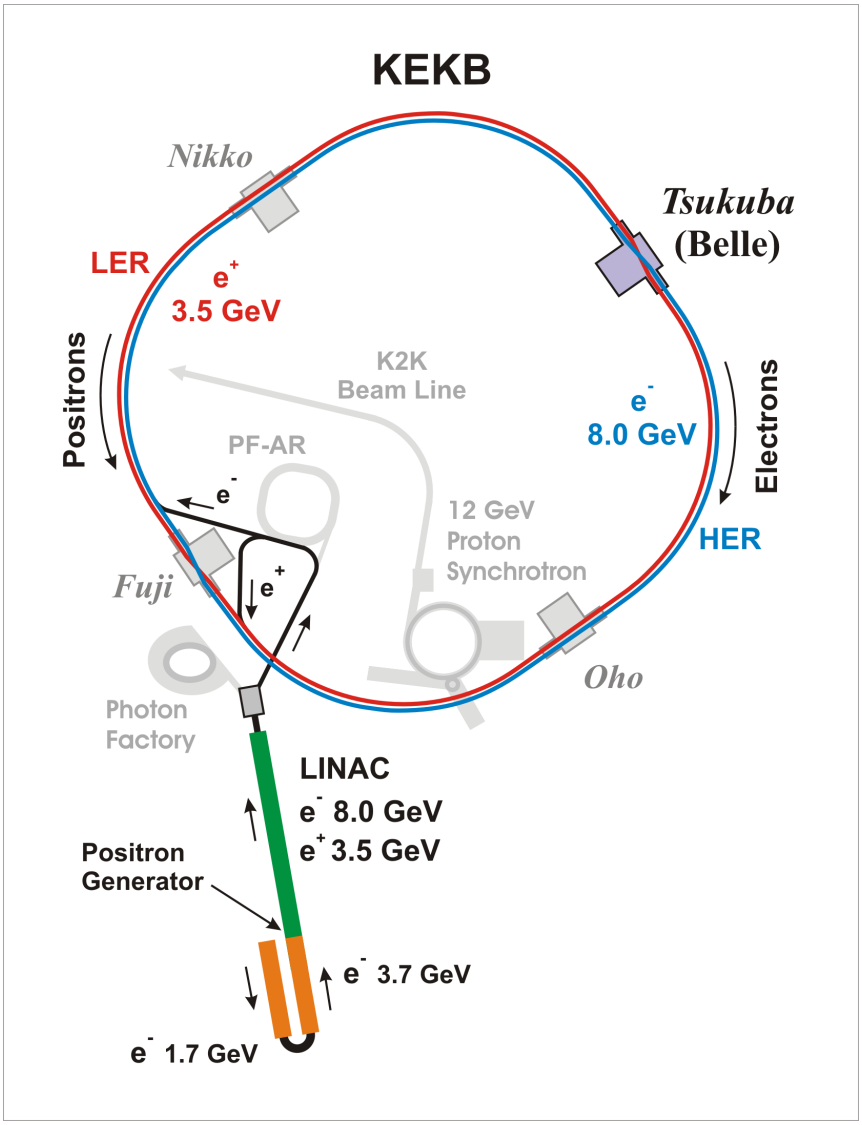

Figure 2.2: Schematic view of the KEKB configuration

Since the mass of the $\Upsilon(4S)$ is only slightly above the combined mass of the $B\bar{B}$ pair, the B mesons are produced almost at rest in the $\Upsilon(4S)$ frame. Note that $\beta\gamma$ is also the boost of the B mesons. The distance that the B mesons fly in the boost direction before they decay is 0.2 mm on average. TABLE 2.1 shows the summary of the parameters for KEKB [23].

The performance of the accelerator is evaluated by its luminosity $\mathcal{L}$:

$$R = \mathcal{L} \times \sigma \tag{2.3}$$

where R is the rate of the electron-positron collisions in Belle and σ is the total electron-positron cross section. The designed luminosity for KEKB was $10^{34}\text{cm}^{-2}\text{sec}^{-1}$ according to the formula:

$$\mathcal{L} = \frac{1}{2er_e}\xi_y \left(\frac{\gamma I}{\beta_y^*}\right)_{\pm} = (2.2 \times 10^{-34})\xi_y \left(\frac{\gamma I}{\beta_y^*}\right)_{\pm} \tag{2.4}$$

with the unit $\text{cm}^{-2}\text{s}^{-1}$. The included parameters in the formula are

- e: the elementary electric charge;
- r_e: the classical electron radius, in cm;
- ξ_y: the vertical beam tune shit parameter;
- β_y^*: the vertical β function [24] at the interaction point, in cm;
- γ: the Lorentz boost factor;
- I: the beam current, in A;
- E: the beam energy, in GeV.

This goal was surpassed by a factor of two, with a peak luminosity of $2.11 \times 10^{34}\text{cm}^{-2}\text{sec}^{-1}$ as shown in FIG 2.3 [25]. The overall integrated luminosity exceeded 1040 fb^{-1} when KEKB ceased operation in 2010.

Table 2.1: Machine Parameters of the KEKB (June 17, 2009)

	LER	HER	Unit
Circumference	3016		m
RF Frequency	508.88		MHz
Horizontal Emittance	18	24	nm
Beam current	1637	1188	mA
Number of bunches	1584+1		
Bunch current	1.03	0.75	mA
Bunch spacing	1.84		m
Bunch trains	1		
Total RF voltage V_C	8.0	13.0	MV
Synchrotron tune ν_s	-0.0246	-0.0209	
Betatron tune ν_x/ν_y	45.506/43.561	44.511/41.585	
beta's at IP β_x^*/β_y^*	120/0.59	120/0.59	cm
momentrum compaction α	3.31×10^{-4}	3.43×10^{-4}	
Estimated vertical beam size at IP from luminosity σ_y^*	0.94	0.94	μm
beam-beam parameters ξ_x/ξ_y	0.127/0.129	0.102/0.090	
Beam lifetime	133@1637	200@1188	min.@mA
Luminosity (Belle CsI)	21.08		$10^{33}/\mathrm{cm}^2/\mathrm{sec}$
Luminosity records per day /7days/30days	1.479/8.428/30.208		/fb

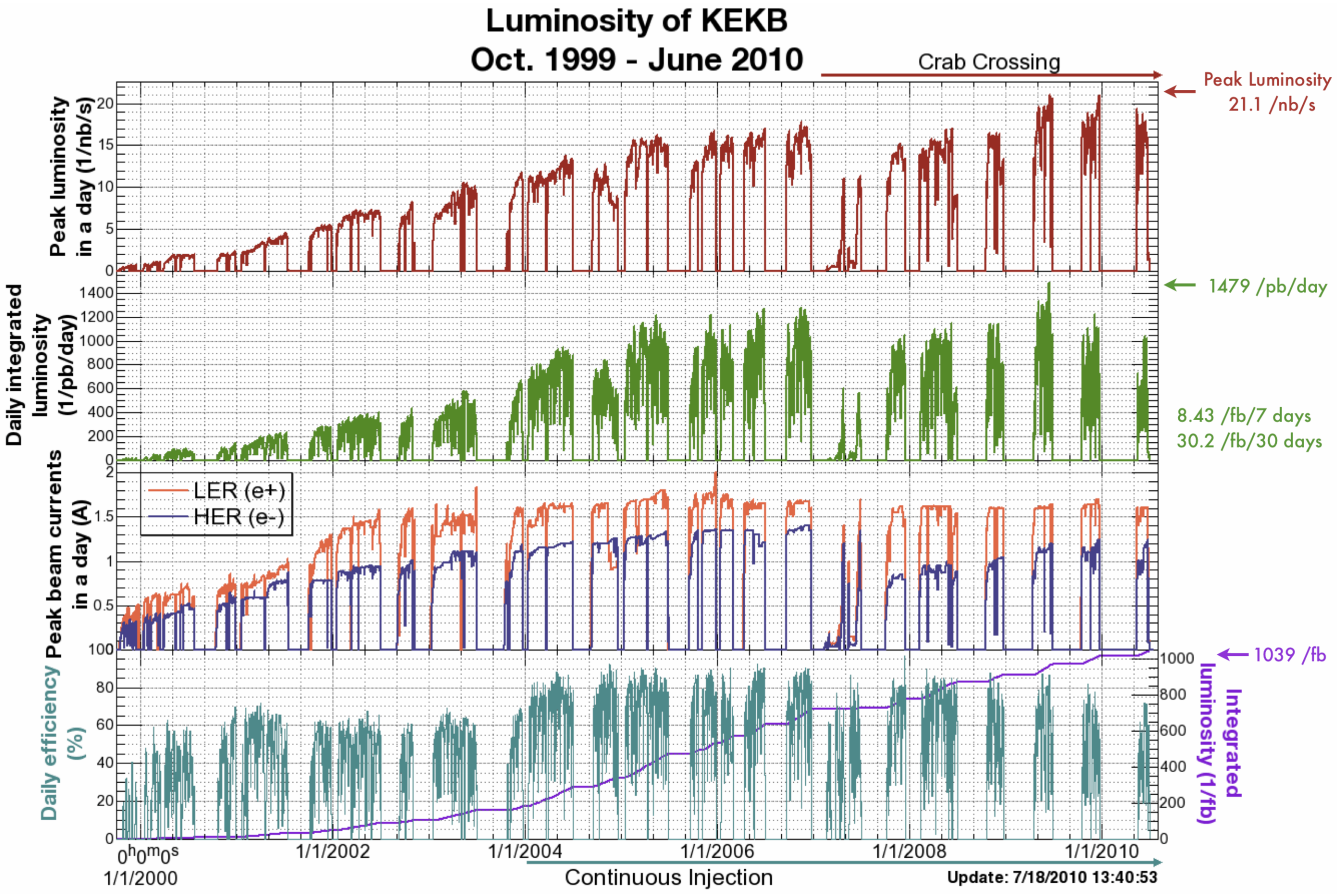

Figure 2.3: History of luminosity in KEKB

To pursue higher luminosity in KEKB, two superconducting crab cavities [26] were built and installed in the accelerator rings. The configuration of the two beams has a 22 mrad angle between the e^+ and e^- bunches when they collide. The crab cavities rotate the bunches relative to longitudinal alignment along the beam direction; thus, they can collide head-on rather than obliquely, as shown in FIG 2.4. This results in each positron bunch intersecting more of the counter-moving electron bunch. The improvement of the luminosity engendered by crab cavities is shown in FIG 2.5.

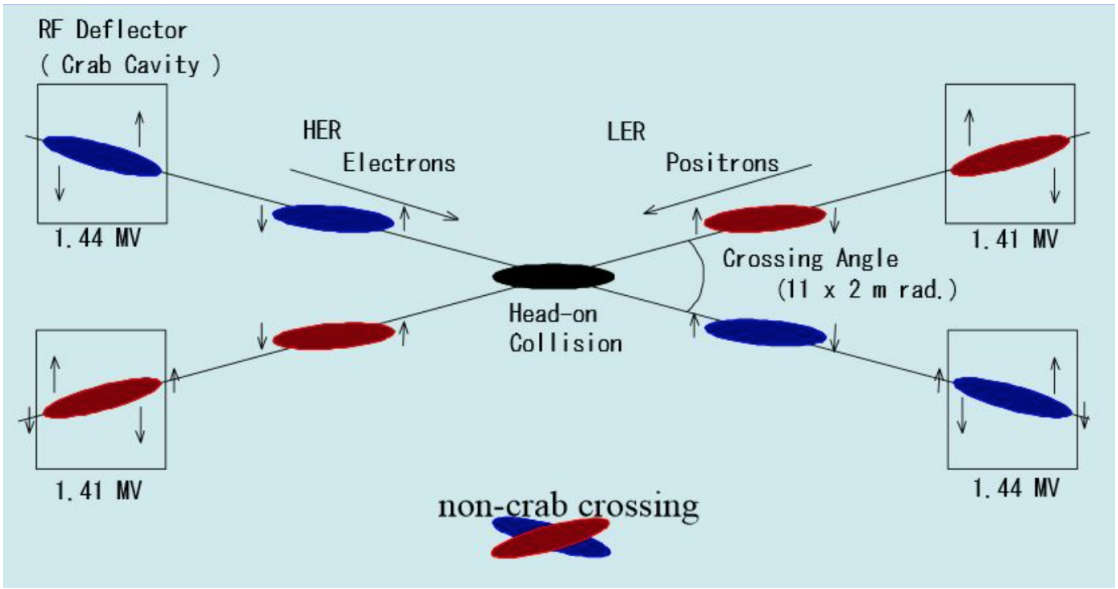

Figure 2.4: Crab cavities kick beam bunches sideway then the bunches collide head-on

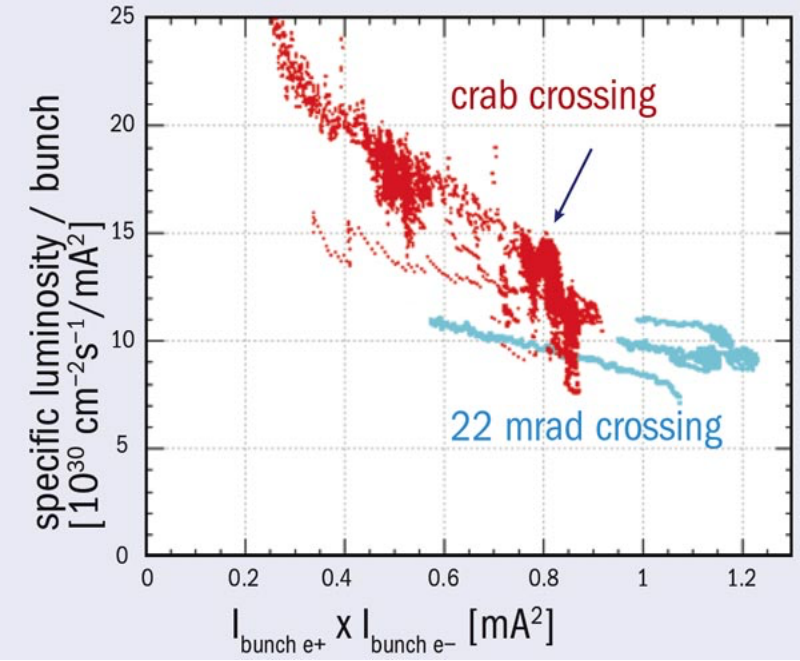

Figure 2.5: Luminosity vs. beam current plot shows clear luminosity improvement due to crab crossing.

2.3 The Belle Detector

The Belle Detector is a multi-layer particle detector surrounding the IP for measuring the properties of the decay particles from the created $B\bar{B}$ pairs. It consists of the following sub-detectors and elements: a double-walled cooled beryllium beam pipe, Extreme Forward Calorimeter (EFC), Silicon Vertex Detector (SVD), Central Drift Chamber (CDC), Aerogel Cherenkov Counter (ACC), Time of Flight Counter (TOF), Electromagnetic Calorimeter (ECL), solenoid magnet, K_L and Muon detector (KLM), trigger and Data Acquisition system (DAQ), and off-line software and computing facilities. The solenoid magnet between the ECL and the KLM generates 1.5 T magnetic field in all the inner sub-detectors and an oppositely directed magnetic field within the iron plates of the return yoke in which the KLM sits. A charged particle traveling inside the magnetic field moves along a helical path with the axis parallel to the field direction. The cutaway view of the Belle detector, with all the subdetectors mentioned above, is shown in FIG 2.6.

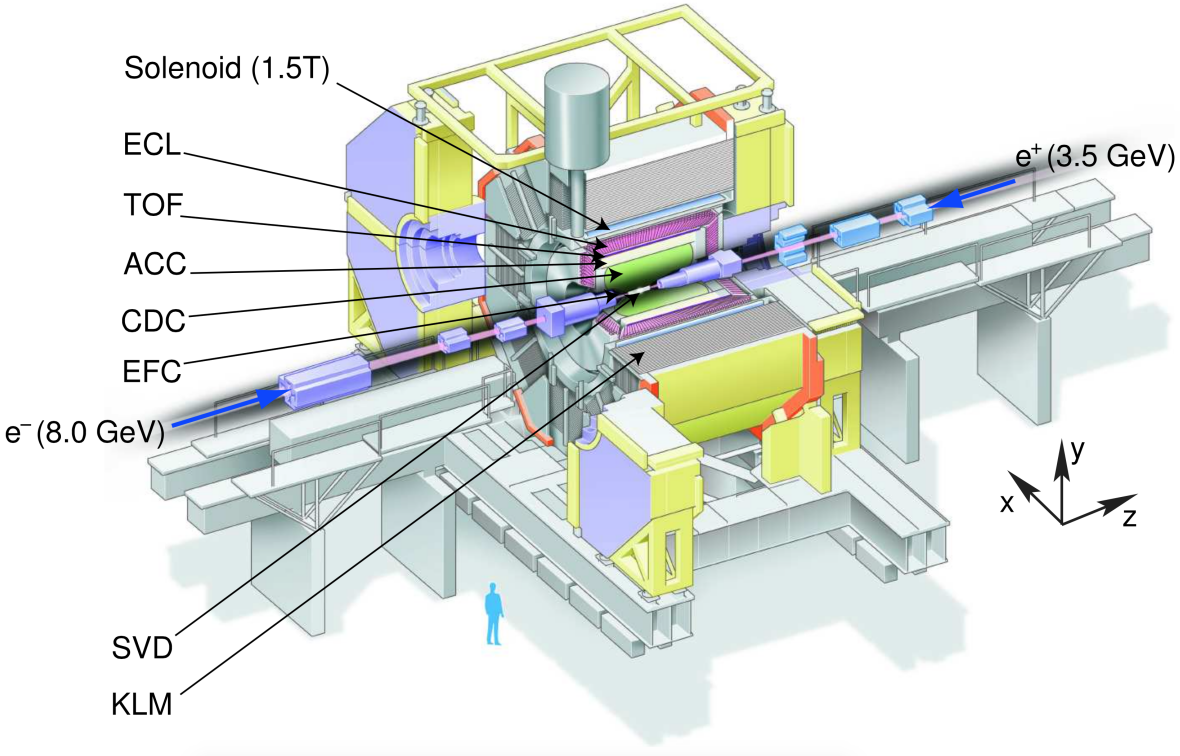

Figure 2.6: The 3-D cutaway view of the Belle detector

The detector coordinate system is defined as the following:

- The origin: the crossing point of the beams (IP).
- The x axis: the horizontal vector pointing away from the KEKB center.
- The y axis: the vertically upward direction.
- The z axis: the direction opposite the positron beam.
- The radial distance in the transverse plane : $r = \sqrt{x^2 + y^2}$.
- The polar angle θ, measured with respect to the z axis.
- The azimuthal angle ϕ, measured counterclockwise in the transverse plane with respect to the x axis.

The Belle detector can be divided into 3 sections: the barrel section, parallel to the beam axis, and the forward and backward endcaps, extending radially from the beam axis at the two ends of the detector, as shown in the side view of FIG 2.7. The polar angle coverage is shown in TABLE 2.2.

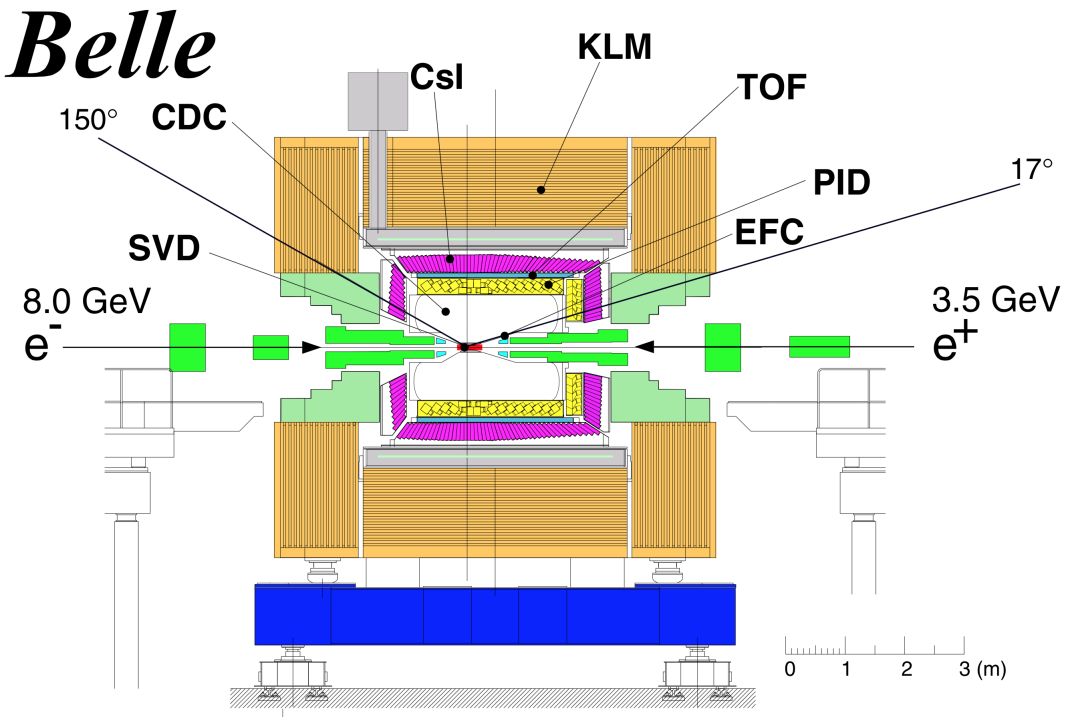

Figure 2.7: The side view of the Belle detector

Table 2.2: Polar angle coverage of the Belle detector in the three regions

Region	polar angle coverage
Barrel	$34° < \theta < 127°$
Forward endcap	$17° < \theta < 34°$
Backward end cap	$127° < \theta < 150°$

In the following sections, each subdetector is described briefly in the technical point of view; the pictures are taken from Ref. [15] unless stated otherwise.

2.3.1 The Beam Pipe

The beam pipe maintains the accelerator vacuum around both beams. The measurement of the decay-vertex distribution of the B mesons is strongly dependent on the vertex resolution, which improves proportional to the inverse of the radius of the innermost detector layer that is just outside the beam pipe [27]. Competing with this, a decrease of the radius of the beam pipe would cause an increase of beam-induced backgrounds: synchrotron radiation (SR) and showers from scattered beam particles by the residual gas or intra-beam scattering (Particle background) [28]. Higher beam currents also generate more heat, which would cause serious aging problem of the detector. Therefore, the beam pipe ("interaction point chamber") should be designed to lower the background and heating of the nearby detectors. The beam pipe is made of 2 nested cylinders of beryllium extending from $z = -4.6$ cm to $z = 10.1$ cm with radii 20.0 mm and 23.0 mm; the radial thickness of each layer is 0.5 mm. Helium gas flows in the gap between the cylinders for cooling. Mylar with a 20 μm-thick gold layer is wrapped around the outer cylinder to reduce the SR background. The cross-section view of the beam pipe is shown in FIG 2.8. During the SVD upgrade from SVD1 to SVD2 in 2003, a new beam pipe was installed with a smaller radius of 1.5 cm.

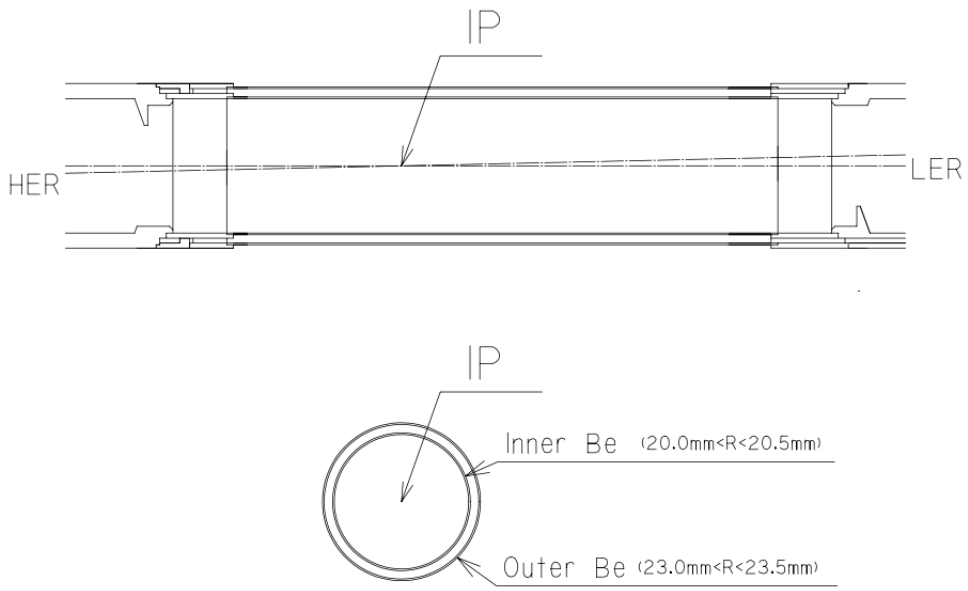

Figure 2.8: The configuration of the original beam pipe.

2.3.2 The Extreme Forward Calorimeter (EFC)

The EFC detector is designed to detect photons and electrons in the extreme forward ($6.4^\circ < \theta < 11.5^\circ$) and backward ($163.3^\circ < \theta < 171.2^\circ$) regions that are not covered by the electromagnetic calorimeter. It is installed around the beam pipe close to the IP where there is a significant high level of synchrotron radiation as well as Bhabha scattering of the beams. Radiation-hard bismuth germanate $Bi_4Ge_3O_{12}$ (BGO) crystals are used to detect the signals. As shown in FIG 2.9, the BGO crystals in the EFC are trapezoidal and are housed in a conical container that points to IP in both θ and ϕ. Both forward and backward detectors are segmented into 32 sections in the ϕ-direction and 5 sections in the θ-direction. The energy resolution of the EFC is 7.2% at 8 GeV and 5.8% at 3.5 GeV. There are many functions for the EFC, such as a passive shield to reduce background in the CDC, a beam monitor for the KEKB control, a luminosity monitor for the Belle experiment, and a tagging

device for two-photon physics.

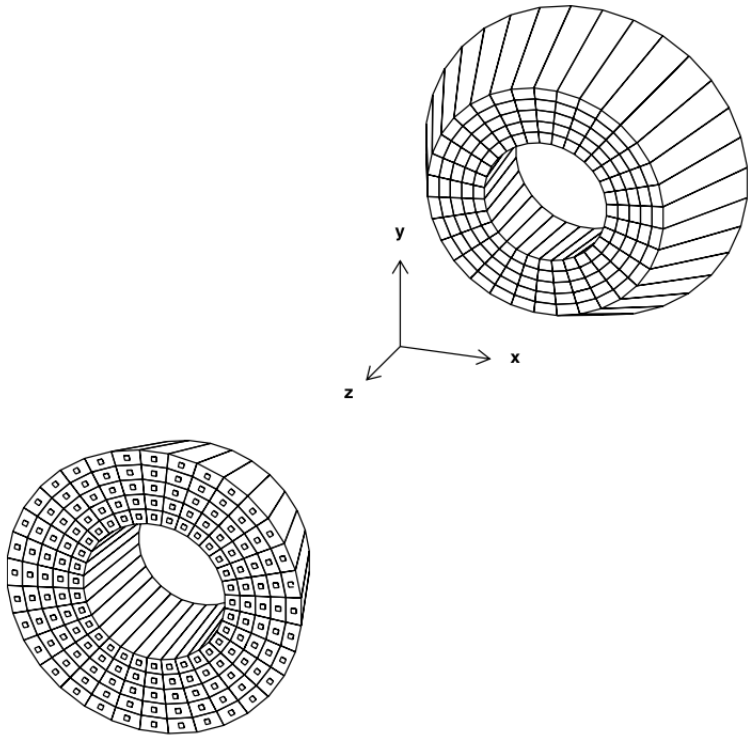

Figure 2.9: BGO crystals of the forward and backward EFC detectors.

2.3.3 The Silicon Vertex Detector (SVD)

The silicon vertex detector is designed to measure the separation between B^0 and $\bar{B}^0$ decay vertices, which can be translated into a lifetime difference that is exploited in the study of time-dependent CP violation [27]. To obtain the CP asymmetry parameters, the resolution of the SVD is 100 μm, which is better than the average flight distance of B mesons of approximately 200 μm in KEKB.

Double-sided silicon strip detectors (DSSDs), as shown in FIG 2.10, are utilized in the SVD since they provide good intrinsic resolution and low amount of material inside the detector acceptance. A charged particle traversing the depleted pn junction of the detector

creates holes (h^+) and electrons (e^-) along its trajectory. The e^-h^+ pairs initiate current in p^+ and n^+ stripes along the surface of the bulk. The p^+ stripes are aligned along the beam axis to measure the azimuthal angle ϕ, and the n^+ stripes are aligned perpendicular to the beam axis to measure z. The size of the DSSD is $57.5 \times 33.5 \times 0.3$ mm^3 with 1280 strips and 640 readout pads on each side.

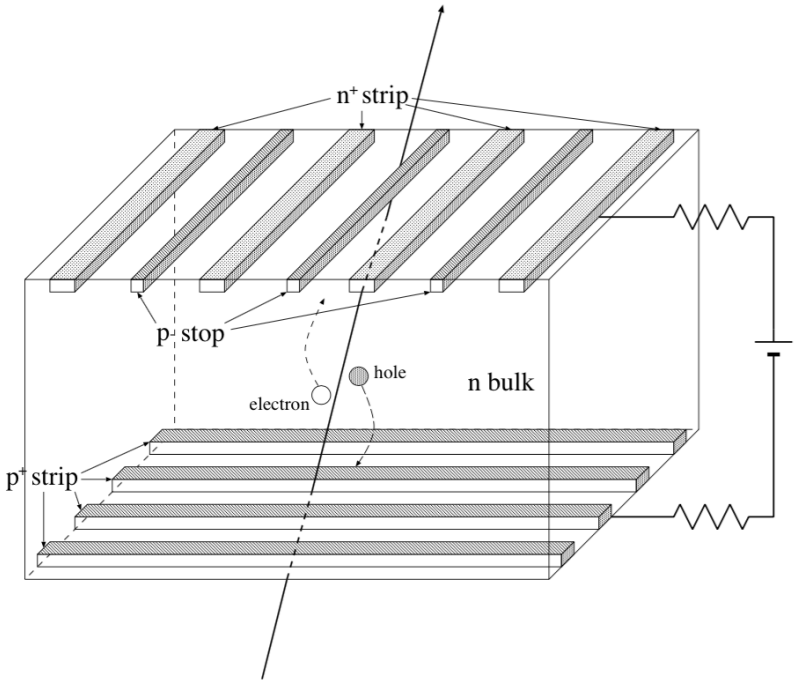

Figure 2.10: Schematic view of DSSD with illustration of a particle detection.

The SVD was upgraded in 2003 to replace damaged detectors and improve the performance. FIGs 2.11 and 2.12 [29] show the configurations of the old SVD (SVD1) and the upgraded SVD (SVD2). Since the radius of the beampipe decreased from 20 mm to 15 mm, the new innermost layer of SVD2 is closer to the the axis of the beam. Thus, it has to endure more intense irradiation. The SVD2 has a significant improvement in radiation tolerance, better spatial resolution from one extra layer of ladders, and larger solid angle coverage. Some specific characteristics of the SVD1 and SVD2 are shown in TABLE 2.3.

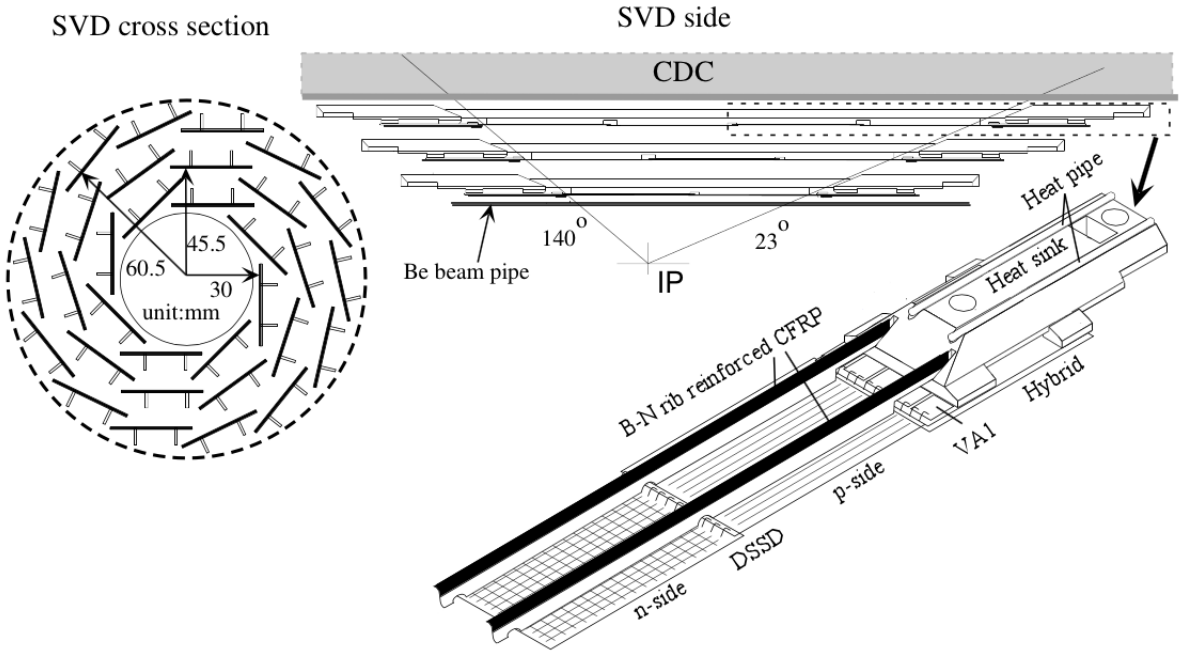

Figure 2.11: Configuration of SVD1.

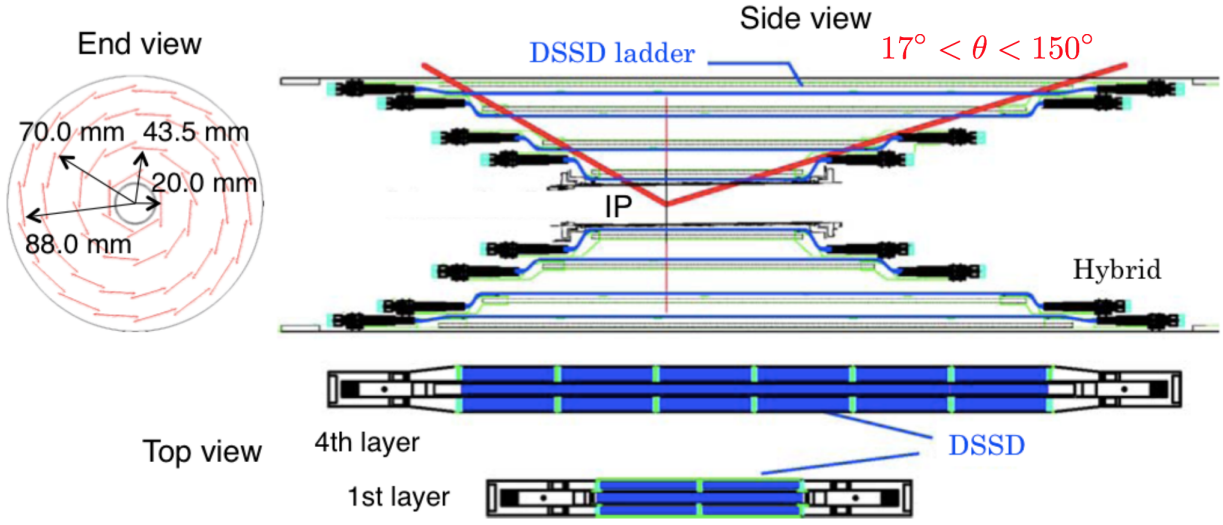

Figure 2.12: Configuration of SVD2.

Table 2.3: Characteristics of SVD1 and SVD2

	SVD1	SVD2
Beampipe radius (mm)	20	15
Number of layers	3	4
Number of DSSD ladders in layers 1/2/3/4	8/10/14/NA	6/12/18/18
Number of DSSDs in a ladder in layers 1/2/3/4	2/3/4/NA	2/3/5/6
Radii of layers 1/2/3/4 (mm)	30.0/45.5/60.5/NA	20.0/43.5/70.0/88.8
Angular coverage (acceptance)	$23^\circ < \theta < 140^\circ (0.86)$	$17^\circ < \theta < 150^\circ (0.92)$
Total number of channels	81920	110592
Strip pitch (μm) for z	84	75 (73 for layer 4)
Strip pitch (μm) for $r\phi$	25 (50 for readout)	50 (65 for layer 4)
DSSD thickness (μm)	300	300
Total material at $\theta = 90^\circ$ (%X0)	1.85	2.6
Radiation tolerance (MRad)	~ 1	> 20
Intrinsic DAQ deadtime/trigger (μs)	128	25.6

The impact parameter resolution is the most important parameter in characterizing the performance of the SVD. FIG 2.13 shows the impact parameter resolutions for the dz and dr in the SVD1 (green) and SVD2 (red). The data are obtained from cosmic ray events and e^+e^- collision data. These resolutions are given by

$$\sigma_{dz} = 42 \oplus 44/p\beta \sin(\theta)^{5/2} [\mu m] \quad \text{(for SVD1)} \tag{2.5}$$

$$\sigma_{dr} = 19 \oplus 54/p\beta \sin(\theta)^{3/2} [\mu m] \quad \text{(for SVD1)} \tag{2.6}$$

$$\sigma_{dz} = 28 \oplus 32/p\beta \sin(\theta)^{5/2} [\mu m] \quad \text{(for SVD2)} \tag{2.7}$$

$$\sigma_{dr} = 22 \oplus 36/p\beta \sin(\theta)^{3/2} [\mu m] \quad \text{(for SVD2)} \tag{2.8}$$

where p, β, and θ are the momentum (in GeV/c), velocity (relative to c), and polar angle of the track, respectively. It is clear that the resolution for a given momentum is better in SVD2 due to the smaller radii of the beampipe and the extra DSSD layer. More specific description of the SVD is presented in Ref [30].

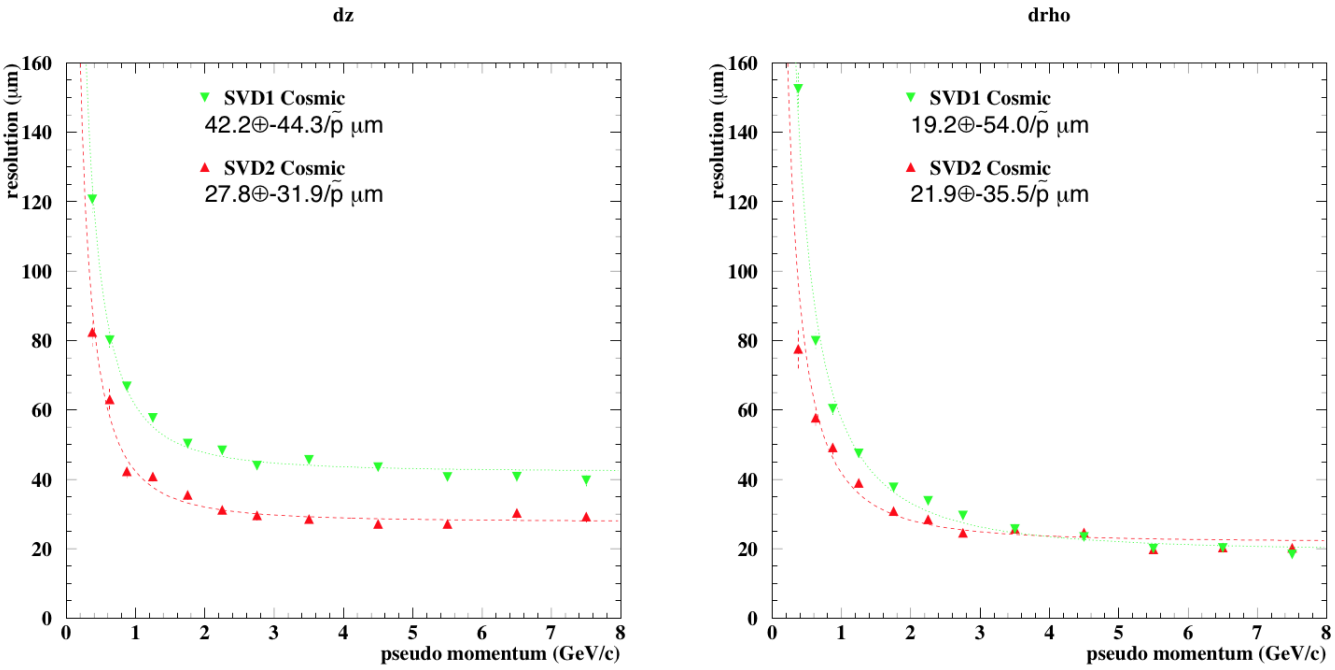

Figure 2.13: Impact parameter resolutions in z (left) and $r\phi$ (right) coordinates for SVD1 and SVD2.

2.3.4 The Central Drift Chamber (CDC)

The Central Drift Chamber reconstructs trajectories of charged particles by detecting the ionization of the gas, measures the specific (partial) ionization energy loss dE/dx for particle identification (for kaons, pions, protons, and electrons), and provides information on the hits for triggering.

The structure of the CDC is shown in FIG 2.14 from the side and end view. The CDC covers the region $17° < \theta < 150°$ and consists of 32 axial layers, 18 small angle stereo layers,

and 3 cathode strip layers for measuring the $r - \phi$ position with 10μm resolution and z positions with 2 mm resolution. The CDC contains 8400 drift cells; as the functional unit, each such cell consists of a sense wire surrounded by uninstrumented field wires along the beam direction as shown in FIG 2.15. The field wires are shared with the neighboring cells. In conjunction with the upgrade of the SVD, the inner radius of the CDC (77 mm) was increased to 140 mm by removing three inner layers and installing two layers of small-cell CDC (sCDC) modules instead.

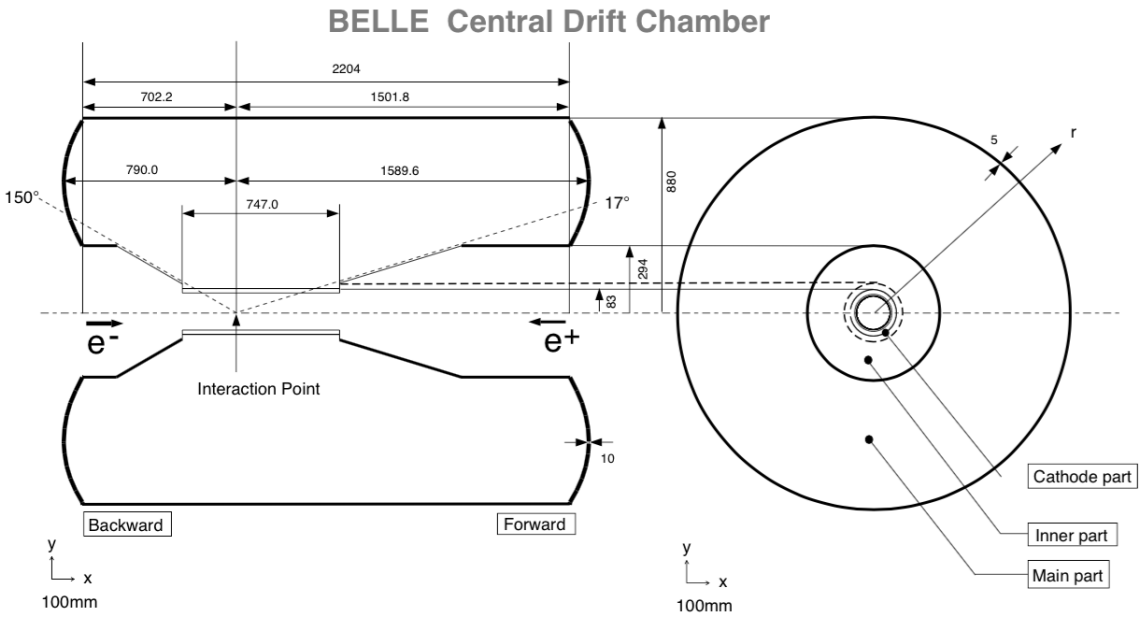

Figure 2.14: CDC side-view (left) and end-view (right).

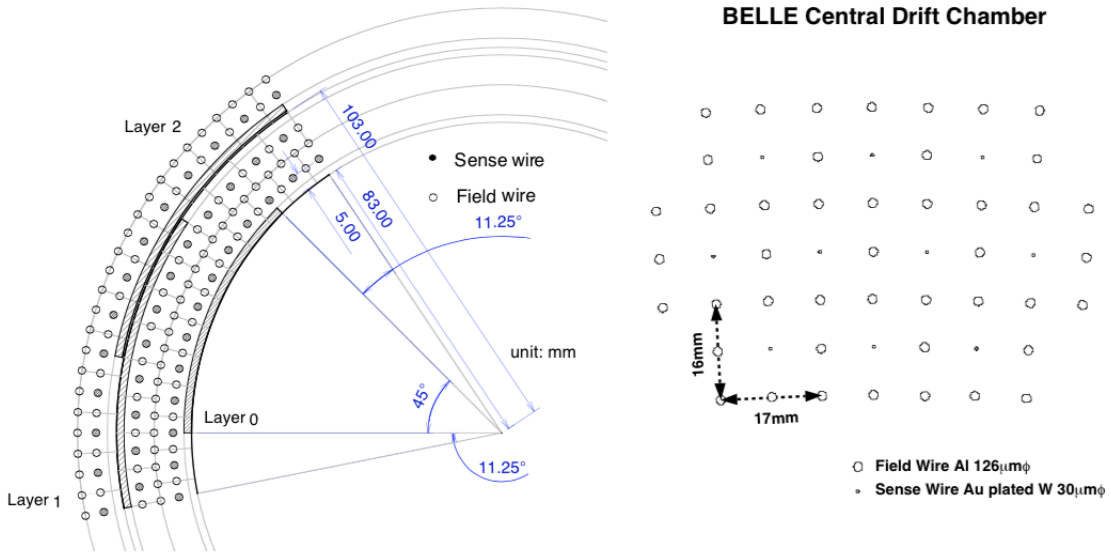

Figure 2.15: Cross section of the cell structure in CDC.

The CDC is filled with a mixture of 1 : 1 helium and ethane gas, which has a long radiation length of 640 m, to minimize the multiple Coulomb scattering and improve the momentum resolution [31]. The electron density from the ionization of ethane improves the resolution of the ionization-energy-loss measurement. A charged particle traveling in the CDC ionizes the gas along its direction of motion. The ionized electrons and positive ions are attracted to the anode sense wire and cathode field wires, respectively. Further ionization by these accelerating charges due to the high electromagnetic field near the wire gives rise to avalanches of electrons and positive ions. An electrical pulse is induced when the avalanche reaches the sense wire. The pulse height is related to the energy deposited through the ionization of the gas, and the drift time reflects the distance of the original ionization point to the wire. From the pulse-height information the loss of energy dE/dx is used as an ingredient in the particle identification.

The reconstruction of a track using the CDC information provides the three-dimensional momentum of the track at the IP. This information is encoded in the form of an ideal helix

aligned with the solenoidal magnetic field. The helix can be determined by 5 parameters: three parameters for the circular motion in a plane and the other two for the motion in a straight line. The transverse momentum (p_T) resolution, defined as $\sqrt{2}(p_T^{\rm down} - p_T^{\rm up})/(p_T^{\rm down} + p_T^{\rm up})$, is shown in FIG 2.16. The distribution of dE/dx versus the momentum of particles is shown in FIG 2.17. Since the loss of energy depends on the velocity of a particle with certain momentum, the dE/dx distributions with different masses of particles are separated. Thus, the CDC is used for π/K identification for momenta below 0.8 GeV/c with 3-σ separation. Further technical details of the CDC can be found in Ref [32].

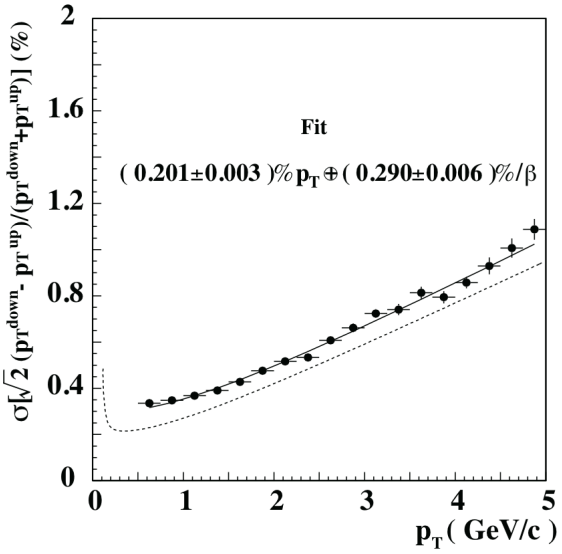

Figure 2.16: Resolution of the transverse momentum for cosmic rays in the CDC. The fitted result and ideal expectation for highly relativistic ($\beta \simeq 1$) particles are shown by the solid and dotted curve, respectively.

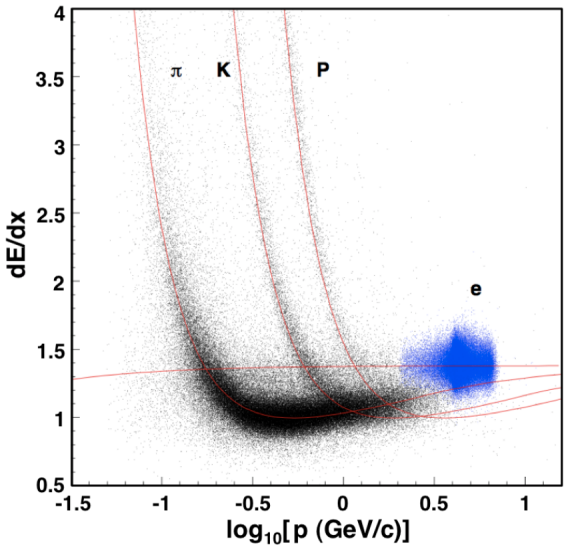

Figure 2.17: Particle identification from dE/dx measurement in CDC.

2.3.5 The Aerogel Cherenkov Counter (ACC)

The silica Aerogel Cherenkov Counter is crucial for distinguishing charged pions from kaons with the momentum between 1.2 GeV/c and 3.5 GeV/c [27]. When a charged particle moves faster than the phase velocity of light in the medium, Cherenkov light is emitted in the form of a wavefront at a fixed angle with respect to the trajectory of the particle. Specifically, the condition for the emission of the Cherenkov light is

$$n > \frac{1}{\beta} = \sqrt{1 + \left(\frac{m}{p}\right)^2}, \quad \text{or} \quad m < p\sqrt{n^2 - 1} \tag{2.9}$$

where n is the refractive index of the medium, and m, p, and β are the mass, momentum, and speed (in units of the speed of light) of the particle, respectively. The ACC does not measure the Cherenkov cone angle. Instead, it is a binary device that is sensitive to the presence or absence of Cherenkov light. For a given momentum measured by the other detectors, a certain selection of n will generate Cherenkov radiation for pions but not for kaons, which achieves the K/π discrimination.

The ACC spans the polar angle region of $17° < \theta < 127°$ with barrel ($34° < \theta < 127°$) and forward end-cap ($17° < \theta < 34°$) as shown in FIG 2.18 [27]. The barrel ACC consists of 960 counter modules segmented into 60 cells in the ϕ direction. Five types of aerogel with graded refractive indices of $n = 1.010, 1.013, 1.015, 1.020, 1.028$ are arranged in the barrel ACC according to the polar angle. The forward end-cap ACC contains 228 counter modules arranged into 5 concentric layers; the refractive index of the aerogel is 1.030. The generated Cherenkov photons are detected by fine-mesh photo-multiplier tubes (FM-PMT) in each counter module. Three different sizes of FM-PMT, with radii of 1, 1.25 or 1.5 inches, are used in the counter modules according to the refractive index to obtain roughly constant photon yield in all counters. The counter modules in the barrel and end-cap are shown in FIG 2.19. Further information on the ACC can be found in Refs. [33] and [34].

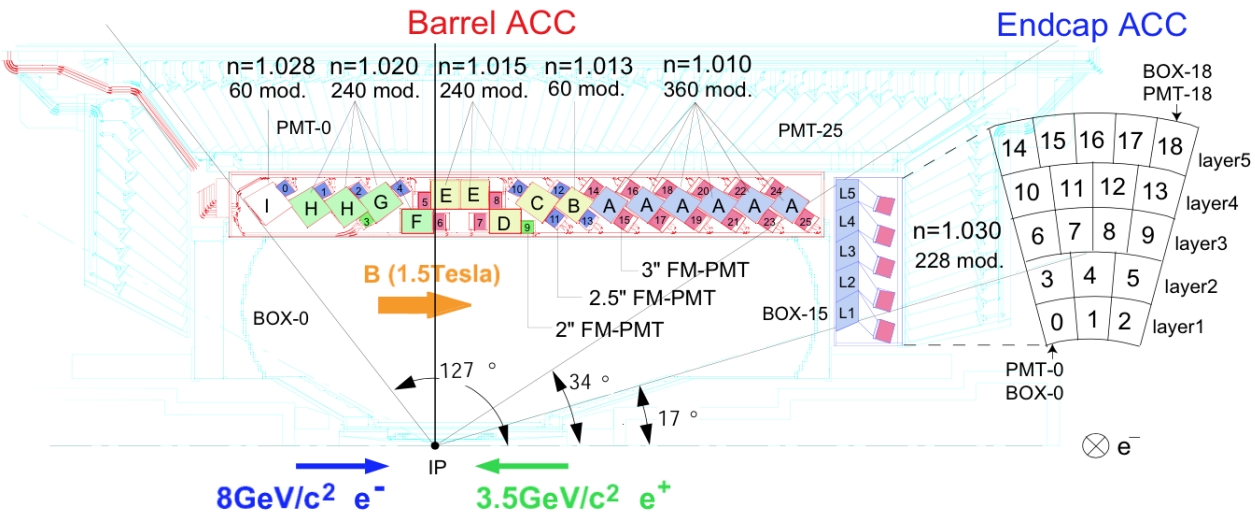

Figure 2.18: Configuration of the ACC detector.

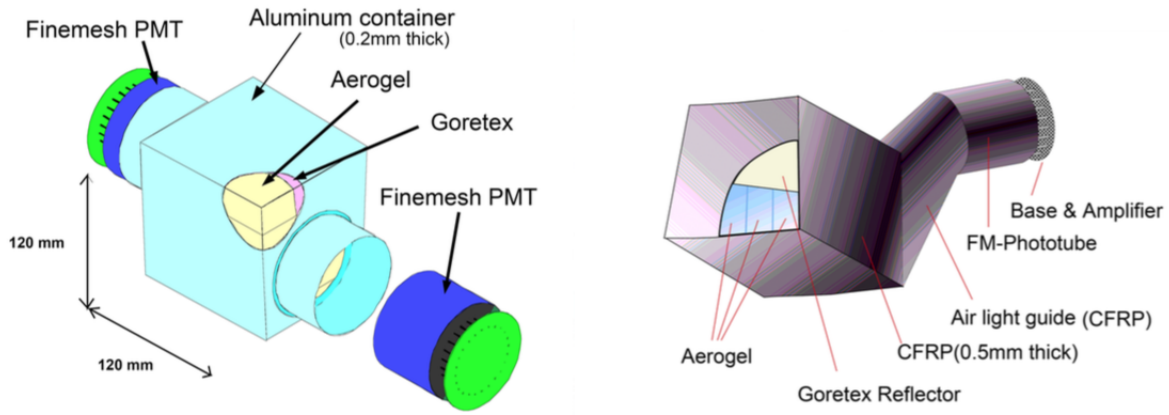

Figure 2.19: Schematic view of ACC modules for barrel (left) and end-cap (right).

2.3.6 The Time-of-Flight Counter (TOF)

The time of flight counter performs charged particle identification in the momentum range of 0.8 to 1.2 GeV/c by measuring the velocity of particles using the known distance from the IP and measured time of flight with a timing resolution of 100 ps. The TOF also provides a fast and accurate timing signal for the trigger system. The flight time T for a particle of mass m with flight length L is

$$T = \frac{L}{c}\sqrt{1 + \left(\frac{mc}{p}\right)^2}. \tag{2.10}$$

Since the momentum of the particle can be measured by the CDC and the distance L can be obtained by the track helix parameters from the CDC, the mass of the particle can be calculated according to EQ (2.10) to identify the type of the particle.

The TOF system, which covers the polar region of $33° < \theta < 121°$ (i.e., barrel only), is comprised of 64 modules concentric with the z-axis at $r = 1.2$ m. One module, as shown in FIG 2.20, consists of two trapezoidally shaped TOF counters and one Trigger Scintillation Counter (TSC), separated radially by 1.5 cm. The plastic scintillators in the TOF emit light pulses after excitation by the passage of an energetic charged particle. The TSC module

rejects photon-conversion backgrounds in the trigger through an anti-coincidence between TOF and TSC counters. The FM-PMTs, mounted directly on the ends of the scintillator, collects the scintillation light from the counter.

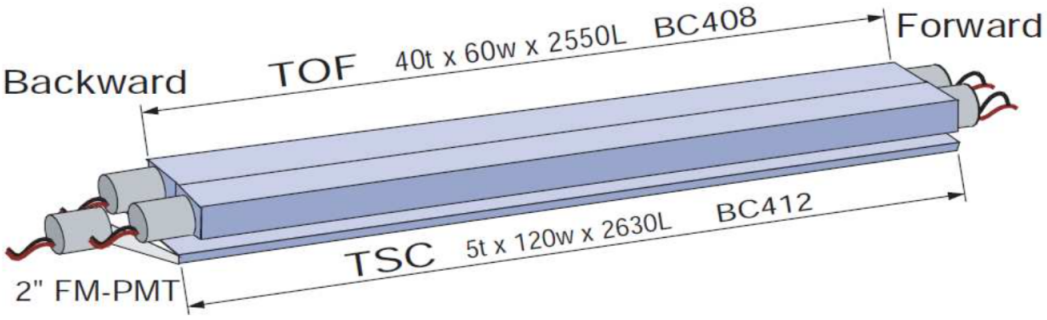

Figure 2.20: Overview of a TOF/TSC module.

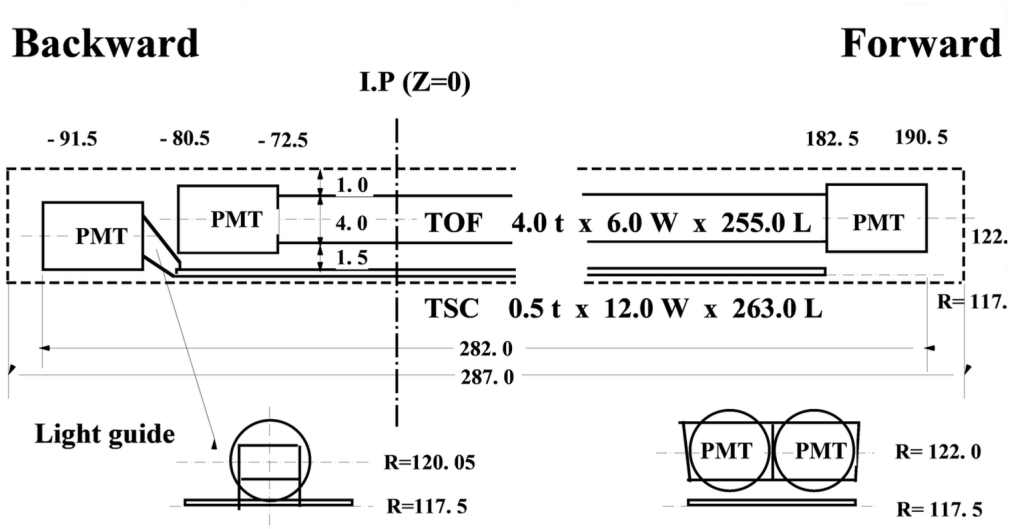

Figure 2.21: Structure of a TOF/TSC module. The unit of the numbers in the figure is mm.

The performance of the TOF for K/π separation as a function of momentum is shown in FIG 2.22, which demonstrates clear 2-σ separation for particle momentum up to 1.25 GeV/c. The mass distribution in FIG 2.23 shows a comparison between real data and MC simulation for a timing resolution of 100 ps. The evident peaks shows clear separation among pions,

kaons, and protons. More specific information about the TOF can be found in Ref [35].

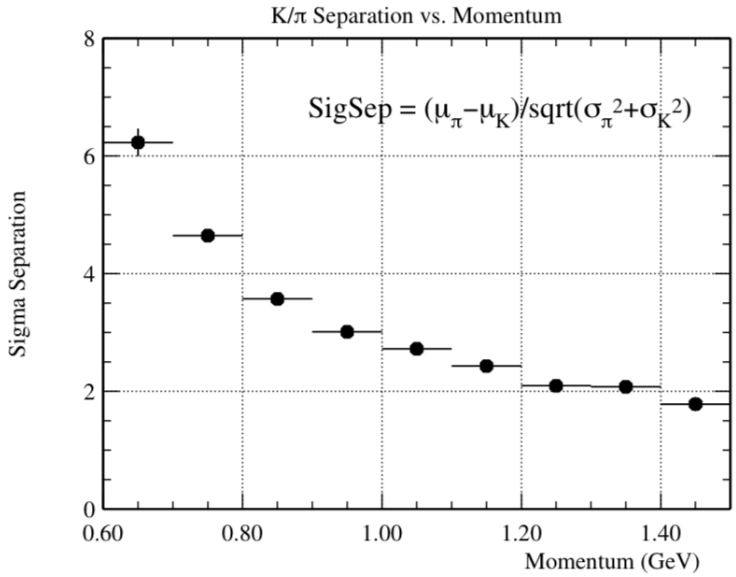

Figure 2.22: Performance of TOF for K/π separation as a function of momentum. In the legend, μ_π and μ_K are pion and kaon hypothesis probabilities, respectively, while σ_π and σ_K are the time resolutions for these hypotheses.

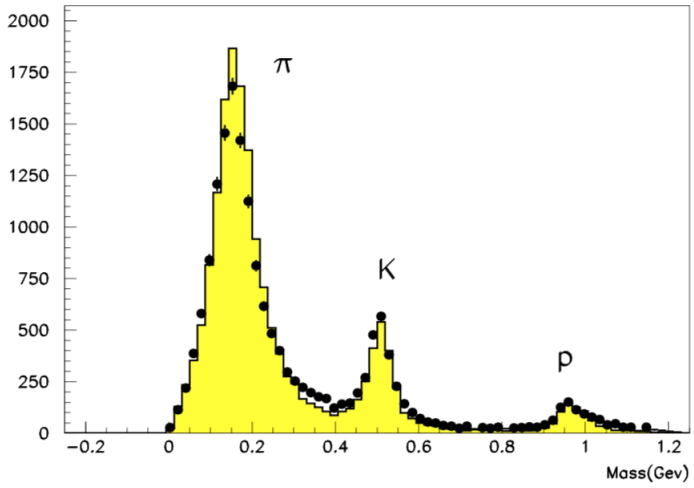

Figure 2.23: Mass distribution from the TOF measurements for particle momenta below 1.2 GeV/c.

2.3.7 The Electromagnetic Calorimeter (ECL)

The Electromagnetic Calorimeter is designed to measure the energy and directions of photons from π^0 and radiative B decays with high efficiency and resolution. Another purpose of the ECL is the identification of electrons through the presence of an electromagnetic shower (which does not occur for the other charged-particle species). The energy and the opening angle of two decay photons from a high momentum neutral pion need to be measured precisely for the reconstruction of the neutral pion. Thus, a fine-grained segmentation is required in the ECL.

The ECL, as shown in FIG 2.24, consists of 8736 crystals. Each trapezoidal crystal is tower-shaped with a depth of 30 cm and a front surface (nearest the IP) of about 5×5 cm^2. The specific geometrical parameters are summarized in TABLE 2.4; the structure of a crystal counter is shown in FIG 2.25. The energy of a photon or electron is measured by the crystal luminescence following the electromagnetic shower it deposits in the CsI(Tl) crystals through Bremsstrahlung and pair creation. The crystal are arranged that they all point to the IP but with a tilt of about 2° in both θ and ϕ to avoid having any inter-crystal crack point directly to the IP. At least 80% of the energy of a photon entering the center of one crystal is deposited in that crystal. The surrounding 5×5 array of crystals captures the rest of the shower's energy. The range of energy that can be measured in the ECL is $0.02 < E_\gamma < 5.40$ GeV with a relative energy resolution of

$$\frac{\sigma_E}{E} = \sqrt{1.34^2 + \left(\frac{0.066}{E}\right)^2 + \left(\frac{0.81}{E^{1/4}}\right)^2} \tag{2.11}$$

and an absolute position resolution of

$$\sigma_{\rm pos} = \frac{0.5{\rm cm}}{\sqrt{E}}, \tag{2.12}$$

where the unit of E is GeV. Since the shape and total energy of electron showers evidently differ from those of other charged particles, the charged pions, in particular, can be distinguished from electrons as illustrated in FIG 2.26. The peak on the left is from minimum-ionizing particles which do not shower electromagnetically in the ECL.

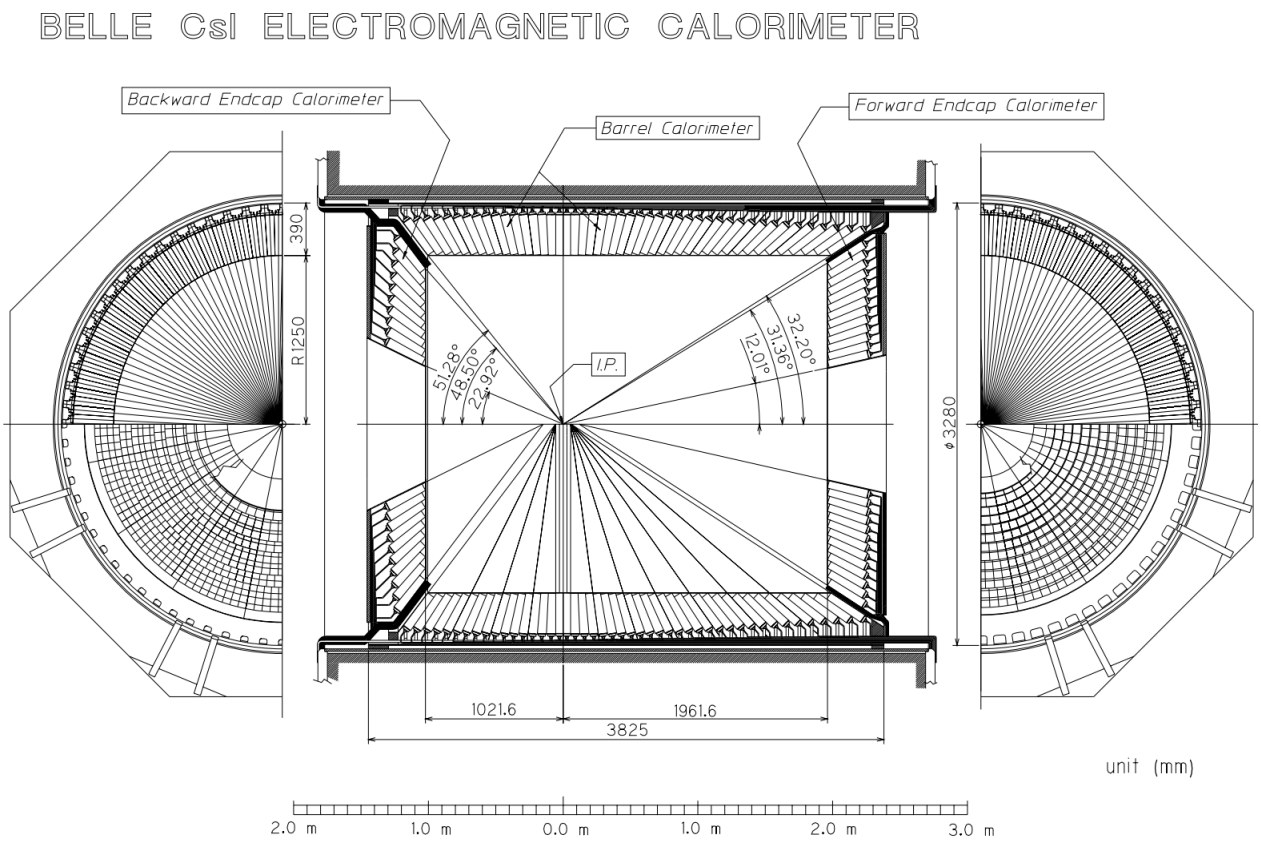

Figure 2.24: The configuration of ECL.

Table 2.4: Geometrical parameters of the ECL

	θ coverage	θ seg	ϕ seg	No. of crystals	position
Forward end-cap	$12.4 - 31.4°$	13	48-144	1152	$z = 1961.6$ mm
Barrel	$32.2 - 128.7°$	46	144	6624	$r = 1250$ mm
Backward end-cap	$130.7 - 155.1°$	10	64-144	960	$z = -1021.6$ mm

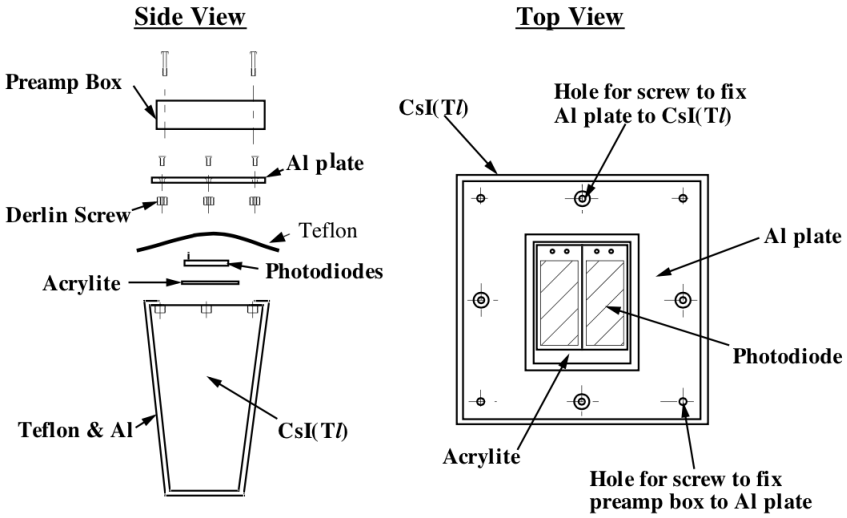

Figure 2.25: Mechanical assembly of the ECL counter.

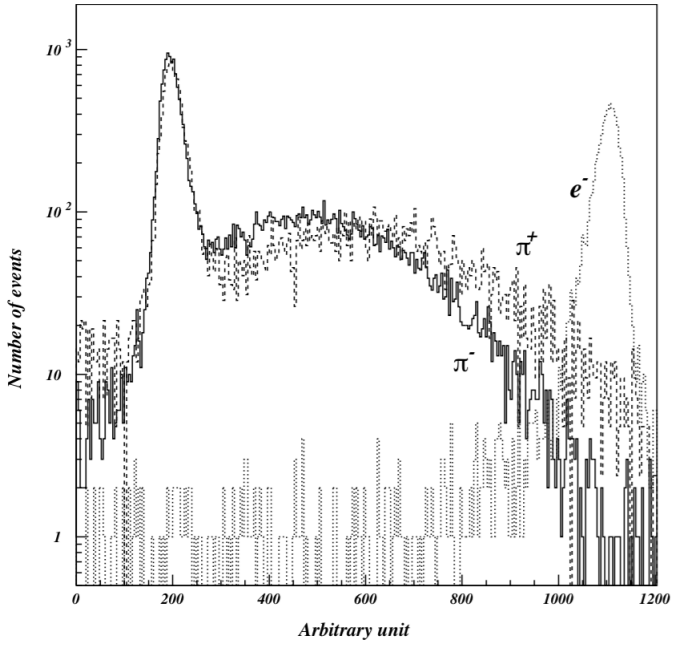

Figure 2.26: Distributions of the energy deposit by e^-, π^+ and π^- at 1 GeV/c.

2.3.8 The K_L and Muon Detector (KLM)

The K_L and muon detector, as the outermost sub-detector, is designed to detect K_L mesons as well as muons with momentum higher than 0.6 GeV/c [36]. The barrel region covers an angular range $45° < \theta < 125°$ and the end-caps extend the range to $20° < \theta < 155°$. The KLM consists of alternating layers of charged particle detectors and iron plates. There are 15 detector layers and 14 iron layers in the octagonal barrel region, and 14 detector layers in each of the end-caps. One detector panel, as shown in FIG 2.27, is a super-layer of two glass-electrode Resistive Plate Counters (RPC) [37] between two planes of orthogonal cathode strips. An ionizing particle moving in the gas-filled gap of the RPC initiates a streamer in the gas (a mixture of Ar, C_4H_{10} and CH_2FCF_3) that results in a local discharge of the glass plates; the resulting streamer induces signals on the external orthogonal cathode strips. These signals, which then travel down the transmission-like strips to external readout electronics, picked up by the 2 stripes provide a 3-D location information for particle tracking. The schematic view of the KLM modules in the barrel and end-cap are shown in FIG 2.28. The spacers are arranged to guide the gas flow through the RPC to provide uniform gas composition throughout the volume. There are 240 and 122 RPC modules in the barrel and end-caps, respectively.

A K_L particle traveling from the IP traverses approximately one interaction length, primarily in the ECL, before arriving at the KLM. The iron plates in the KLM provide an additional 3.9 interaction lengths to generate a hadronic shower of ionizing particles; the location of this shower, together with the IP as the implicit origin, determines the flight direction of the K_L. Muons with energy higher than 0.6 GeV can reach the KLM and traverse it with only small deflections and minimum-ionizing energy loss; thus, they can be distinguished from charged pions and kaons of the same momentum. For the muon with momentum greater than 1.5 GeV/c, the identification efficiency is more than 90% with a hadronic fake rate of less than 5%.

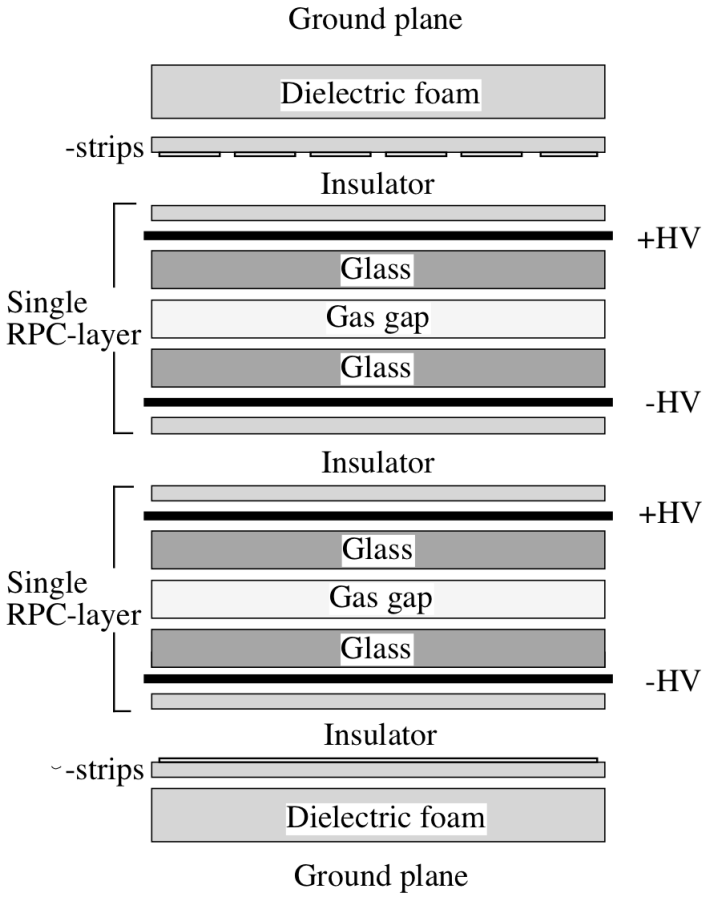

Figure 2.27: Cross section of a KLM super-layer.

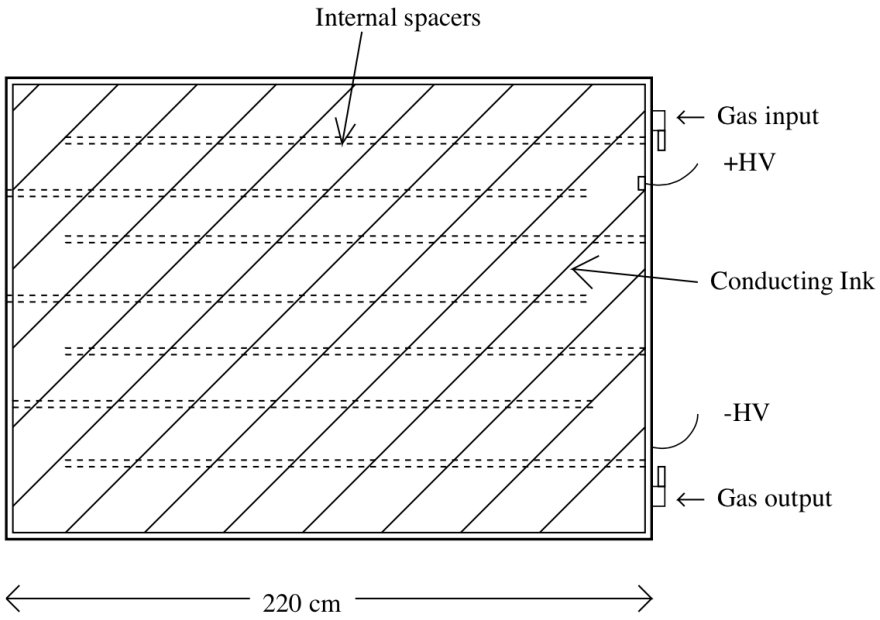

(a)

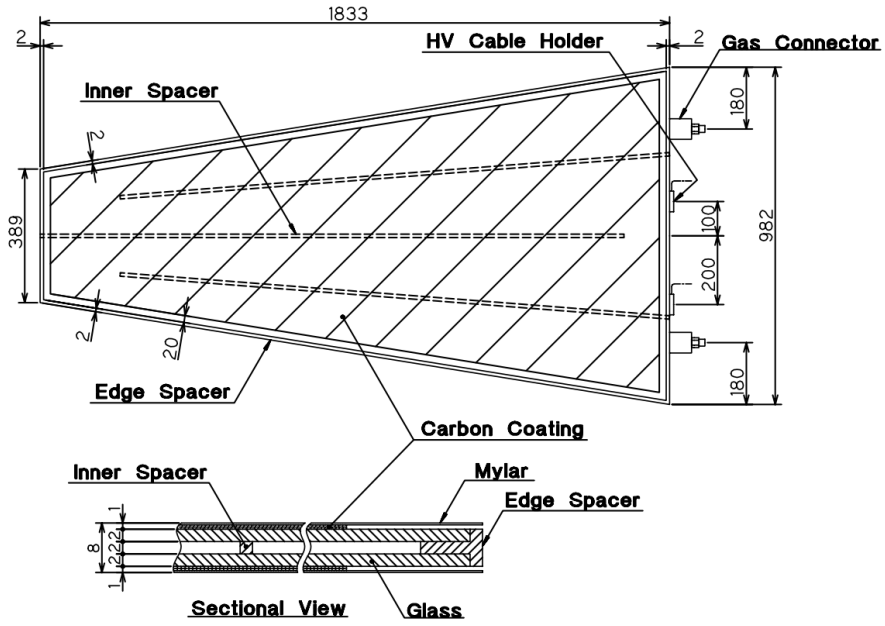

(b)

Figure 2.28: Internal spacer arrangement of RPC for (a) barrel and (b) end-cap.

2.3.9 The Solenoid Magnet and Iron Structure

The solenoid magnet, which contains all the sub-detectors except the KLM, generates a nearly uniform magnetic field of 1.5 T parallel to the beam direction. Its main parameters are shown in TABLE 2.5. The overall structure of the cryostat and the schematic drawing of the coil cross-section are shown in FIG 2.29 [15]. The profile of the axial component of the magnetic field in the vicinity of the beam line is shown in FIG 2.30. The QCS-R and QCS-L in the figure are two superconducting magnet complexes to steer the electron and positron beams; inside each, there is a small compensation solenoid to cancel the effects of Belle's solenoidal field on the beams. The iron yoke surrounding and supporting the Belle detector functions as the return path of magnetic flux and the hadronic-shower material for the KLM. The weight of the iron yoke is 608 t and 524 t for the barrel and end-caps, respectively.

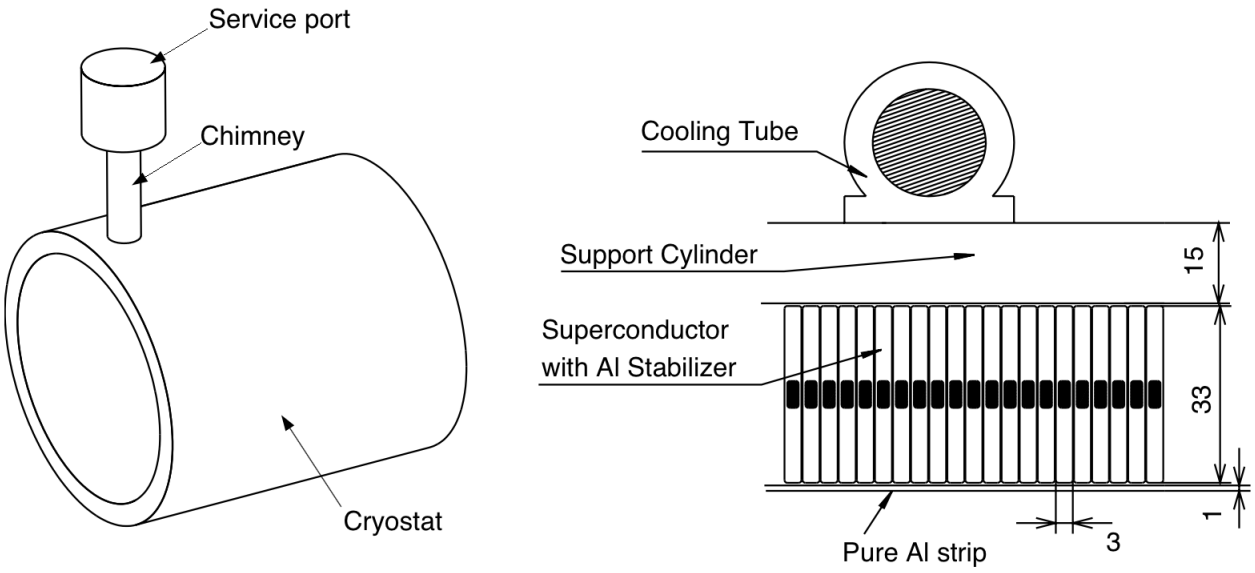

Figure 2.29: An outlook of the solenoid (left) and the cross section view of the coil (right).

Table 2.5: Parameters of the solenoid coil

Cryostat	Radius: outer/inner	2.00 m / 1.70 m
General	Central field	1.5 T
	Total weight	23 t
	Effective cold mass	$\sim$ 6 t
	Length	4.41 m
	Liquid helium cryogenics	Forced low tow phase
	Cool down time	$\leq$ 6 day
	Quench recovery time	$\leq$ 1 day
Coil	Effective radius	1.8 m
	Length	3.92 m
	Conductor dimensions	3×33 mm^2
	Superconductor	NbTi/Cu
	Stabilizer	99.99% aluminum
	Nominal current	4400 A
	Inductance	3.6 H
	Stored energy	35 MJ
	Typical charging time	0.5 h

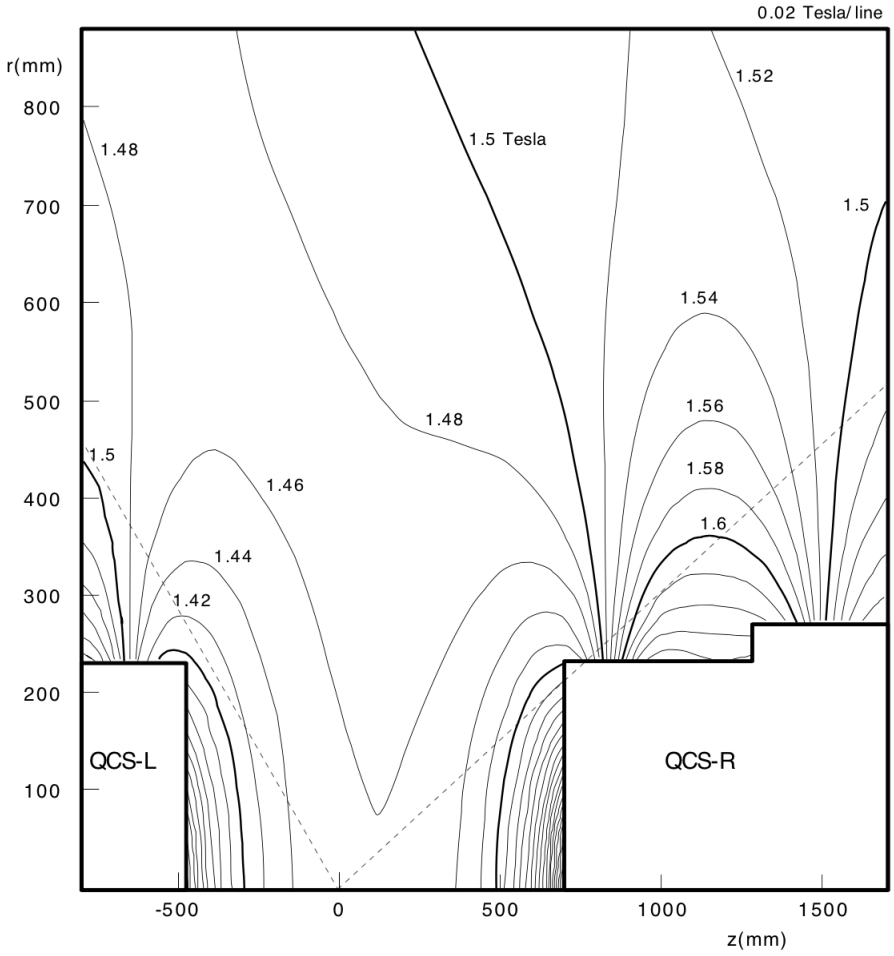

Figure 2.30: Contour plot of magnetic fields in the vicinity of the IP.

2.3.10 Summary of the Belle Detector

TABLE 2.6 summarizes the main characteristics of the Belle detector, including the performances of combined tracking, charged-particle identification and neutral-particle reconstruction. The Belle detector attained—and in many cases exceeded—its design performance and was robust enough to accommodate the increase in the luminosity over the course of its decade of operation.

Table 2.6: Summary of the main characteristics of the Belle detector.

Function	Abbreviation	Type	θ Coverage	Illustrative Performance
Tracking	SVD	Silicon 3/4 layers[a]	$[17°; 150°]$	Single hit resolution: 12 μm ($R\phi$) 19 μm (z)
	CDC	Two-sided Drift chamber	$[17°; 150°]$	Single hit resolution: 130 μm ($R\phi$) 200-1400 μm (z) $\sigma(dE/dx) \sim 7\%$
Particle ID	TOF	Time of flight scintillator	$[34°; 130°]$	$\sigma_t = 100$ ps
	ACC	Threshold Cherenkov with aerogel	$[17°; 127°]$	$N_{\text{p.e.}} \geq 6$[b]
Calorimetry	ECL	CsI(Tl)	$[12.4°; 31.4°]$ $[32.2°; 128.7°]$ $[130.7°; 155.1°]$	$\sigma_E/E \sim 1.7\%$[c]
Muon and K_L^0 detector	KLM	RPC	$[20°; 155°]$	$\sigma_\theta = \sigma_\phi = 30$mrad for K_L^0
PID Algorithms	$\mu^\pm$ (KLM) K/π (TOF, ACC, CDC) $e^\pm$ (CDC,ECL)			$\langle\mu$ eff$\rangle = 90\%$[g] $\langle\mu\pi$ misID$\rangle = 2\%$ $\langle K$ eff$\rangle \geq 85\%$ $\langle\pi$ misID eff$\rangle \leq 10\%$ $\langle e$ eff$\rangle = 90\%$ $\langle\pi$ misID$\rangle \sim 0.3\%$
Tracking	(CDC, SVD)			$\sigma_{p_T}/p_T = 0.0019 p_T[\text{GeV}/c]$ $\oplus\ 0.0030/\beta$
Neutrals	(ECL)			$\sigma(m_{\pi^0}) = 4.8$ MeV/c^2 [h]

(a) Until summer 2003, Belle used a 3 layer SVD. (b) Number of photo-electrons. (c) For Bhabha events. (d) L3 trigger was operated partially from 2004 to 2007. (e) The maximal trigger rate is determined at the end of the DAQ chain. (f) For $B\bar{B}$ events. (g) For momenta above 0.8 GeV/c. (h) For π^0's reconstructed from photons in hadronic events.

2.4 The Trigger System

The trigger system decides whether the an event recorded by the detector should be saved by the data acquisition system (DAQ). Many processes such as cosmic ray events, interactions in the beam pipe, synchrotron radiation or interactions between the beam and residual gas in the vacuum chamber, are undesired. Physical events of interest are beam-collision-

induced hadronic events for physics analysis as well as QED events for detector calibration and luminosity measurement. The trigger identifies the signatures of such processes in the information streaming continuously from some of the sub-detectors and issues a signal to all sub-detectors to record their data when a matching pattern is found; this record defines an event. At the design luminosity ($\mathcal{L} = 10^{34}\text{cm}^{-2}\text{s}^{-1}$), the total rate of events is about 220 Hz including approximately 100 Hz of interesting events. The trigger and data-recording system is designed to operate up to 500 Hz to accommodate increasing luminosity and higher-than-expected background. The trigger rate for each experiment (i.e., run period) in Belle is shown in FIG 2.31. The noise-to-signal ratio (N/S) was roughly 5.6 in experiment 7 and about 1 or less after experiment 37 due to the cleaner environment of the more mature KEKB operation in the later years.

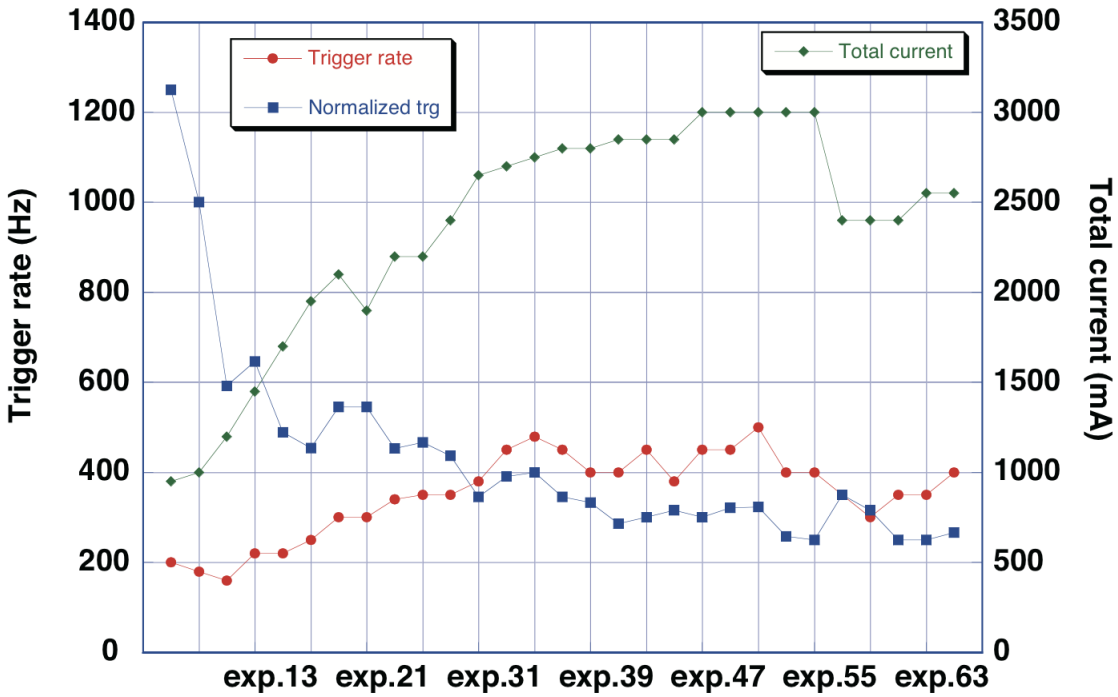

Figure 2.31: Average trigger rate as a function of the experiment number in Belle.

The Belle trigger system consists of the level-1 hardware trigger, the level-3 software trigger implemented by an online computer farm, and a level-4 trigger that operates in the

offline Belle computing system before full event reconstruction, as shown in FIG 2.32.

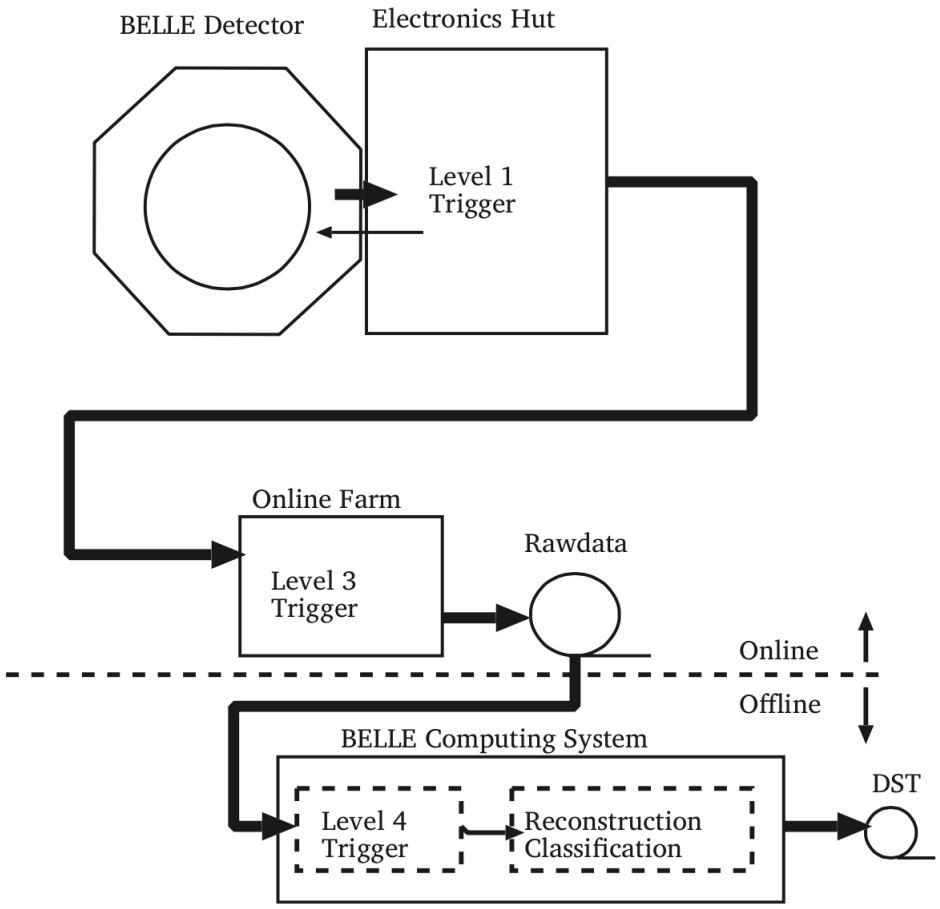

Figure 2.32: A schematic representation of the Belle trigger system.

2.4.1 The Level-1 (L1) Trigger

The Global Decision Logic (GDL) as a central trigger system obtains the trigger signals from each sub-detector and makes the level-1 decision [38], as shown in FIG 2.33. Assuming the time for beam crossing is at $t = 0$, the sub-triggers arrive at the GDL at $t = 1.85$ μs and the trigger decision is issued by $t = 2.2$ μs. The trigger timing is provided by the TOF or, in its absence, the ECL. The CDC and TOF trigger on charged particles by providing their $r - \phi$

and $r - z$ track trigger signals and the information on hit multiplicity and topology [39]. The ECL generates two triggers based on total energy deposition and a cluster multiplicity that is sensitive to different types of hadronic events [40]. The EFC subdetector triggers on Bhabha and two-photon events. The KLM detector trigger provides a signal when muons are detected. The individual trigger efficiency is between 90% and 97% for $B\bar{B}$ [41]. Since the triggers from the sub-detectors are independent, the efficiency for the overlap of these triggers is greater than 99% for the physics processes of interest in Belle.

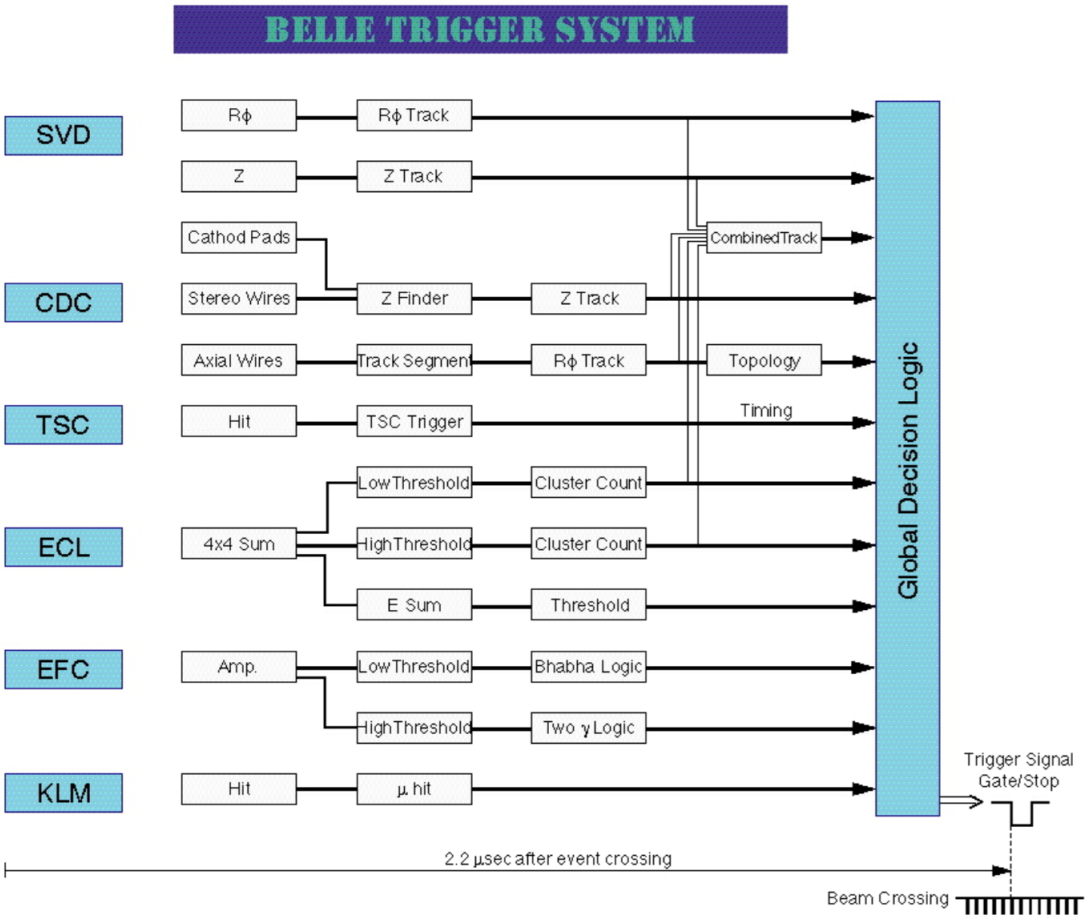

Figure 2.33: Schematic view of the L1 trigger system.

2.4.2 The Level-3 (L3) and Level-4 (L4) Trigger

The level-3 trigger reduce the number of events that pass L1 (except for events that fire the Bhabha or random trigger). The L3 trigger performs a fast track reconstruction and only accepts the event if it has at least one track with $|z| < 5$ cm from the interaction point and energy deposited in the ECL above 3.0 GeV. The L3 software retains more than 99% of the τ pairs and hadronic events while lowering the event rate by 50-60%.

In the off-line analysis of recorded data, the level-4 trigger performs a full reconstruction using a fast tracker and rejects tracks not originating from the IP [42]. The L4 trigger rejects around 78% of events for the "data summary tape" (DST) production while keeping almost 100% of the $B\bar{B}$ events. Although the events rejected by the L4 trigger still remain in the raw data, the CPU time for DST production is reduced. Only the first experiments are processed using the level-4 trigger.

2.5 The Data Acquisition System (DAQ)

The data acquisition system records the events passes the on-line trigger system with a rate of up to 500 Hz with a dead time below 10% [43] . A distributed parallel system is segmented into seven subsystems to handle the data from each of the sub-detectors, as shown in FIG 2.34. The pulse-height (energy-deposition) data from each subsystem except the KLM are converted by a charge-to-time (Q-to-T) converter and a time-to-digital converter (TDC). For the SVD detector, the resulting pulse shape is read out by flash analogue-to-digital converters (FADC) instead of a TDC (which provides only the time of the leading edge of a pulse). The sequence controller (SEQ) generates a stop signal to the TDCs when the final trigger signal from the GDL is received. Then, the signals from the subsystems are transferred and combined by the event builder. The output is sent to an online computer farm where the data is passed through the level-3 trigger filtering-system and combined to the offline structure. The quality of the data is monitored in real time by the online data

quality monitor (DQM) in the online farm. The data is then sent to the mass storage system of the KEK computing center via optical fibers and stored on tape. A typical hadronic $B\bar{B}$ or $q\bar{q}$ event has a data size of around 30 kB, corresponding to a maximum data transfer rate of 15 MB/s at the highest trigger rate.

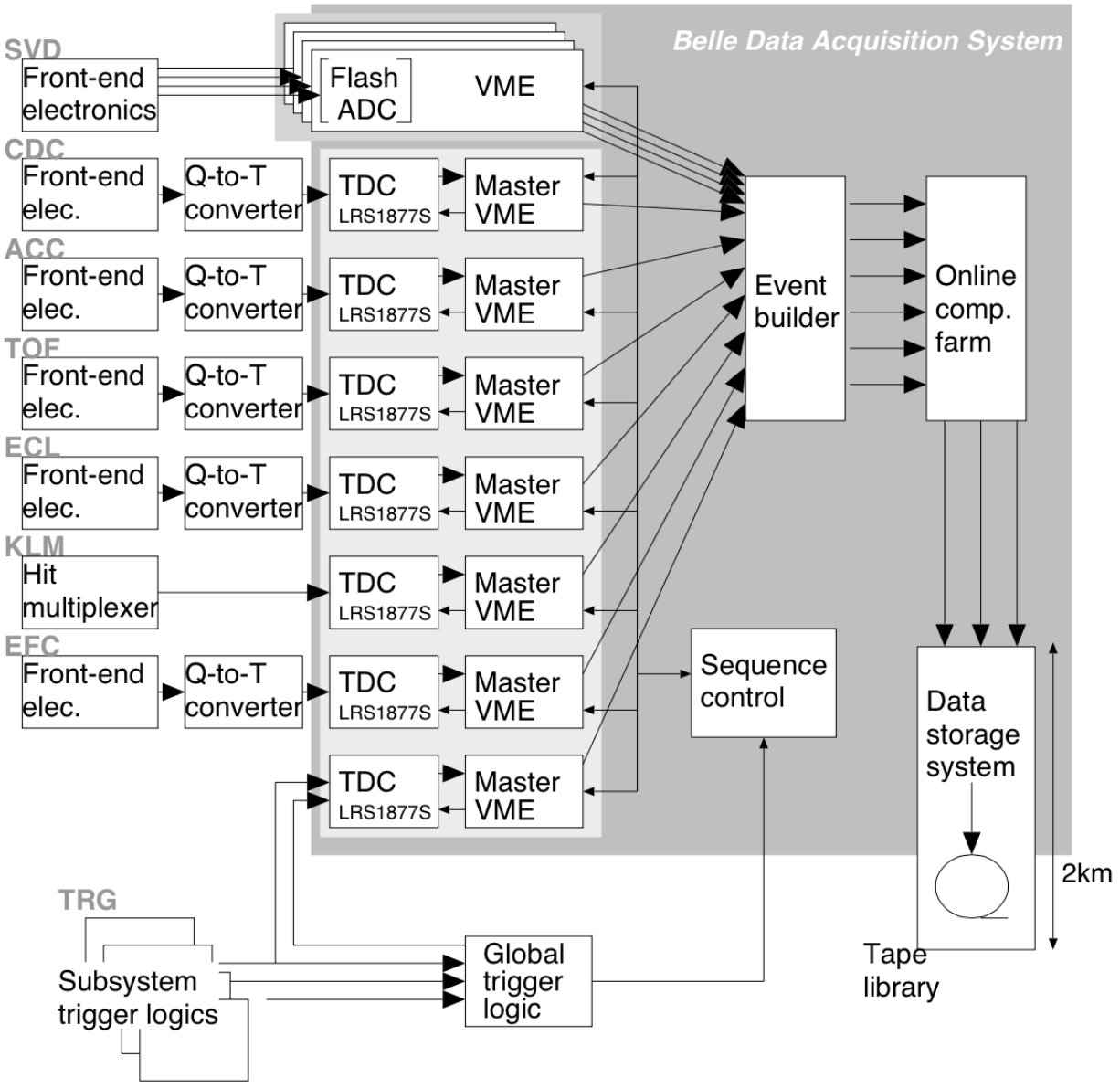

Figure 2.34: The configuration of the Belle DAQ system at the beginning of the experiment.

Since the original DAQ system was implemented with 1990s information technology, maintenance of the system was difficult in the long term because of obsolescence of components and performance limitations exposed by the increasing luminosity of KEKB [44]. In addition, the FASTBUS-based readout system had a readout dead time of more than 10% at the design maximum trigger rate of 500 Hz. The trigger rate at the beginning of data taking was 200 Hz and the dead time was manageable then, but the trigger-rate increase was foreseen at higher luminosity. Since 2001, Belle upgraded of the system: the event builder and VME-based online computer farm were replaced with a set of Linux PC servers (EFARM) connected via Fast Ethernet fibers. The real time reconstruction farm (RFARM) directly fed by the event builder was introduced. The improvement of the FASTBUS readout was also made to reduce the readout dead time by a factor of four. An improvement to the back-end system was made when a second EFARM and RFARM were added in order to have sufficient bandwidth and processing power to cope with the expected increase in luminosity. A new TDC to replace the FASTBUS equipment was developed, based on a common pipeline readout module (COPPER) developed in KEK. By 2009, five detector subsystems were upgraded from FASTBUS to COPPER, resulting in a reduction in dead time to less than 1%. FIG 2.35 shows the Belle DAQ configuration at the end of data taking.

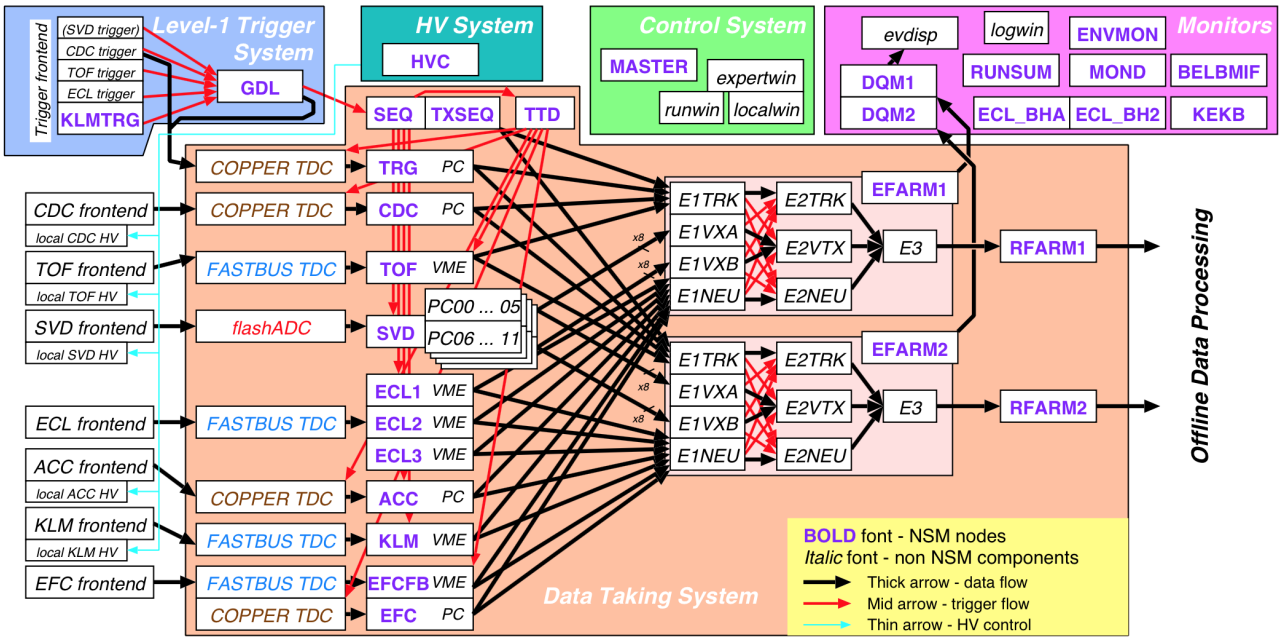

Figure 2.35: The DAQ system at the end of data taking.

2.6 Data Processing

The data accepted by the trigger system are converted from raw data to fully reconstructed events and then stored on the data summary tapes (DST). The three-momentum of a track at the IP is calculated to create physics objects. The charged tracks are reconstructed from the signals of the CDC and then extrapolated outwards to the ACC, TOF, ECL and KLM or inwards to the SVD to search for any corresponding signals. When signals are recorded in the KLM and ECL but there is no association possible to any CDC tracks, the particle is treated as a neutral particle such as photon or K_L meson. Moreover, once the particle-ID likelihoods are determined and particle identification is done, the particle's four-vector is calculated. A variety of flags and ancillary variables are determined that can be used for further analysis. All the information is stored in the DSTs using the PANTHER compressed-data format [45].

Events are further classified in skims of "mini-DSTs" (MDSTs), which are subsamples

of the total data set and are submitted to a handful of loose selection criteria in order to enhance the fraction of specific physics processes. Most analyses, including this one, are performed on the HadronB(J) data skim, which contains the standard hadronic-final-state events [46].

2.7 Software

A lot of software has been developed for the data acquisition, simulation, and analysis in Belle. The data processing and analysis code, called Belle AnalysiS Framework (BASF) [47], was developed in C++ with an extensive use of helper tools such as the Class Library for High Energy Physics (CLHEP) [48].

Comparing the distributions of real data to expectations is an important part of data analysis. Due to the complexity of the detector response and various physics processes that may mimic the signal being studied, the physics process and detector response are modeled using a Monte Carlo simulation instead of analytically derived formulae. There are two stages for producing MC data: the generation of four-vectors from physics processes and the simulation of the detector response. The first step uses the QQ generator [49] developed by the CLEO collaboration to study B meson decays from the $\Upsilon(4S)$ resonance. It incorporates particle properties and event production rates from experiments in the form of world averages and also relevant information from the KEKB accelerator. For newer analyses, the modern EvtGen [50] package is used to generate the particle physics processes with more accurate descriptions of the decay products' phase-space and angular distributions. The generated events are passed to GSIM, which is a BASF module simulating the interactions between the final state daughters and the detector material (including the sensitive detector elements). The simulated data is reconstructed in the same way as real data, with the final MDSTs containing the additional event generator information. Background hits are added by taking random trigger events and overlaying their noise hits onto the MC events.

Chapter 3

Data Sample and Signal Reconstruction

3.1 The Data Sample

This analysis uses the full $\Upsilon(4S)$ data set of $711\,\mathrm{fb}^{-1}$, corresponding to 772×10^6 $B\bar{B}$ pairs. Signal and background Monte Carlo (MC) samples are produced for comparison using the EvtGen program and GSIM. The decay modes for the signal MC contains non-resonant $\pi^{\pm}\pi^{+}\pi^{-}$ (uniform in phase space) and 3 resonances: ρ^0, $\rho(2S)^0$, $f_0(1270)$. We generated and simulated 3.86×10^6 signal events (compared to the expected 6028 in the real data) for Belle experiment 7-65. We also generated and simulated 3.86×10^6 events for each $B\bar{B}$ background ($B^{\pm} \to \bar{D}^0 h^{\pm}$, $B^{\pm} \to J/\psi h^{\pm}$, $B^{\pm} \to \psi(2S) h^{\pm}$, and $B^{\pm} \to K^0_S h^{\pm}$, where h means a kaon or pion). Additional samples from generic $B\bar{B}$ MC, $q\bar{q}$ MC, and rare-B MC are used to study the background suppression and selection algorithms. The generic $B\bar{B}$ MC simulates all the significant B decay modes tabulated by the Particle Data Group [1]. The $q\bar{q}$ MC simulates all the $e^+e^- \to q\bar{q}$ (u, d, s, c) modes for the continuum-background study. The rare-B MC simulates all the rare B decay backgrounds that might contaminate the signal; in this sample, the dominant B decay modes have been removed. The numbers of

generated events for each kind of MC simulation are shown in TABLE 3.1. One MC stream corresponds to the luminosity of the real data in experiments 7 to 63.

Table 3.1: Number of Events in Each Type of MC Simulation

Type of MC Simulation	Number of Events	Number of Streams
Signal MC	3.86×10^6	640
$B^{\pm} \to \bar{D}^0 h^{\pm}$	3.86×10^6	43
$B^{\pm} \to J/\psi h^{\pm}$	3.86×10^6	77
$B^{\pm} \to \psi(2S) h^{\pm}$	3.86×10^6	945
$B^{\pm} \to K^0_S h^{\pm}$	3.86×10^6	576
Generic B		10
Generic $q\bar{q}$		6
Rare B		50

3.2 Reconstruction of Signal Candidate and Data Skim

We use the *cabs*3 package in basf for the reconstruction of B mesons [51]. In the decay $B^+ \to \pi^+\pi^-\pi^+$, two distinct π^+ tracks are different objects, but since they are taken from the same list of particles, one must avoid using the same π^+ twice when forming the B^+ parent. The *cabs*3 package solves this problem and takes care of the charge-conjugated decay chain implicitly as well.

Analyzing the whole dataset repeatedly is inefficient since it takes much time and occupies large disk space. Therefore, we first skim the real data for our specific analysis by applying some loose cuts. Three tracks with "$++-$" or "$--+$" charges are combined to reconstruct a B candidate if its beam constrained mass (M_{bc}) and energy difference between beam energy and reconstructed energy (ΔE) are in the proper range. For the skim of the real data, we require 5.2 GeV/$c^2 < M_{bc} <$ 5.3 GeV/c^2 and $|\Delta E| < 0.5$ GeV. The passing ratio for SVD1

and SVD 2 experiments are 3.1% and 4.5%, respectively. For the skim of generic MC data, some extra conditions are included: $|\Delta E| < 0.3$ GeV, track vertex $|dr| < 1$ cm, $|dz| < 5$ cm, and π/K likelihood ratio $\mathcal{L}_{\pi/K} > 0.1$. The passing ratio for the generic MC is approximately 1.13%.

Chapter 4

Background Suppression

4.1 Continuum Background Suppression

The dominant background comes from $e^+e^- \to q\bar{q}$ ($q = u, d, s$, or c) continuum events. We study several event-shape variables to distinguish signal and continuum events and combine PDF values of these variables for a given event into a single likelihood. In the $\Upsilon(4S)$ rest frame, the event shape for $B\bar{B}$ events and continuum events are spherical and jet-like, respectively. We use the standard Belle technique to reduce the continuum events based on an event-shape likelihood ratio. Using the daughter particles of the signal B candidate and all the other particles in the event (which are assumed to originate from the purported "tagging" B meson in the event), we calculate the following variables: the KSFW likelihood ratio (klr), the cosine of the signal B meson direction in the center of mass (CM) frame ($\cos\theta_B$), the axial distance between the vertex of the signal B candidate and that of the tagging B meson (Δz), and the flavor tagging quality $q \cdot r$ of the tagging B meson ($q \cdot r$). The cosine of the angle between the thrust axis of the B decay and that of the other particle in the event ($\cos\theta_T$) could also be used but our study shows that there is a strong correlation between $\cos\theta_T$ and the KSFW likelihood ratio (see Appendix A) and so it does not provide any additional discrimination. Therefore, we do not use $\cos\theta_T$ here.

4.1.1 KSFW Likelihood Ratio

The KSFW (Kakuno-san's modified Super Fox Wolfram moments [52, 53]) variable is defined as

$$\text{KSFW} = \sum_{l=0}^{4} \sum_{m=c,n,\nu} \alpha_{l,m} (R_l^{so})_m + \sum_{l=0}^{4} \beta_l R_l^{oo} + \gamma \sum_{n=1}^{N} |(P_t)_n| \tag{4.1}$$

The various terms are described below:

R_l^{so} is defined as

$$R_l^{so} = \begin{cases} \dfrac{\sum_{j,k} Q_j Q_k |p_k| P_l(\cos\theta_{jk})}{E_{e^+e^-} - E_B} & (l = 1, 3) \\ \\ \dfrac{\sum_{j,k} |p_j| P_l(\cos\theta_{jk})}{E_{e^+e^-} - E_B} & (l = 0, 4) \end{cases} \tag{4.2}$$

- $P_l(\cos\theta_{jk})$ are Legendre polynomials of the cosine of the angle between the j^{th} and k^{th} tracks, with j and k running over signal-B and other-B tracks, respectively.
- $p_j(Q_j)$ and $p_k(Q_k)$ are the momentum (charge) of corresponding particles.
- $E_{e^+e^-}$ and E_B are the energy in the center of mass frame of e^+e^- and B, respectively.

R_l^{so} is calculated by subdividing the particles from the other B into charged (c), neutral (n), and the missing momentum (ν), which leads to the following three classes:

- $(R_l^{so})_c$ (for $l = 0$ to 4), using only charged tracks of the other B
- $(R_l^{so})_n$ (for $l = 0, 2, 4$), using only photons of the other B
- $(R_l^{so})_\nu$ (for $l = 0, 2, 4$), using only missing momentum of the other B

The parameters $\alpha_{l,c}$, $\alpha_{l,n}$, $\alpha_{l,\nu}$ are the Fisher coefficients for the charged, neutral, and missing-momentum categories, respectively. There are total 11 parameters for $l = 0, 1, 2, 3$ and 4.

R_l^{oo} can be defined identically to R_l^{so} but the summations over j and k both run over charged tracks from the other B. β_l are the 5 Fisher coefficients.

$\sum_{n=1}^{N} |(P_t)_n|$ is the scalar sum of the transverse momenta P_t of all particles in the event multiplied by a Fisher coefficient γ. The n represents particle index, and N is the number of particles in the event.

Therefore, there are a total of 17 parameters used to define the KSFW, which are determined from the signal and continuum MC simulation. The ROOKSFW package [53] is used to train the discriminant (i.e., to determine the optimal values of the 17 Fisher coefficients using pure MC samples of signal and continuum background) and then to calculate the moments and the likelihood klr for a given event to be signal or continuum background. The normalized distributions of klr for signal and continuum background are shown in FIG 4.2.

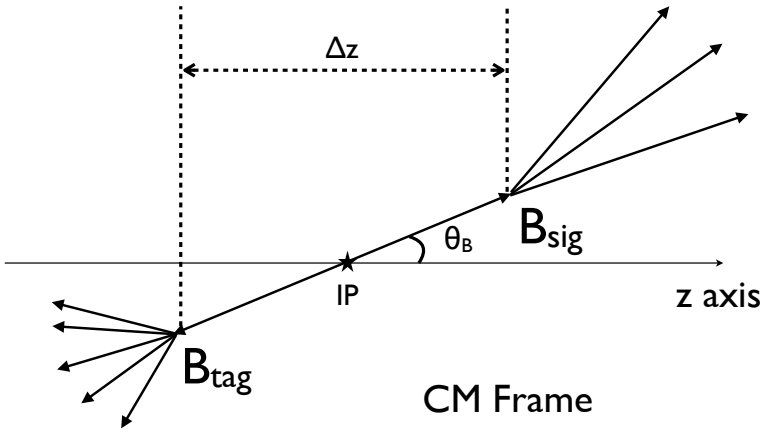

Figure 4.1: Δz and θ_B in the center of mass frame

4.1.2 B Flight Direction

$\cos\theta_B$ is the cosine of the angle between the B-flight direction and the beam axis in the CM frame, as shown in FIG 4.1. For the $\Upsilon(4S) \to B\bar{B}$ decay, the polar angle distribution of the B candidate, having spinless daughters arising from a spin-1 parent, follows a $1 - \cos^2\theta$

distribution in the CM frame. In contrast, the false B candidates formed as random combinations in continuum events emerge uniformly in solid angle. The normalized distributions of $\cos\theta_B$ for signal and continuum background are shown in FIG 4.2.

4.1.3 Vertex Separation

Δz is the vertex separation between the candidate B and the tagging B as shown in FIG 4.1. The absolute value of Δz tends to be larger for the signal events than the continuum events since the B mesons have longer lifetime and so give longer vertex separation along the z (boost) axis in the CM frame. For the events with $|\Delta z| \geq 0.2$ cm, the reconstruction of the vertex is not valid and so this information is not included in the continuum-suppression algorithm. The ratio of the events without Δz to the total number of events is shown in TABLE 4.1. The normalized distributions of Δz for signal and continuum background are shown in FIG 4.2.

Table 4.1: Ratio of events with invalid Δz

	Signal	Continuum
SVD1	9.20%	11.50%
SVD2	6.56%	9.14%

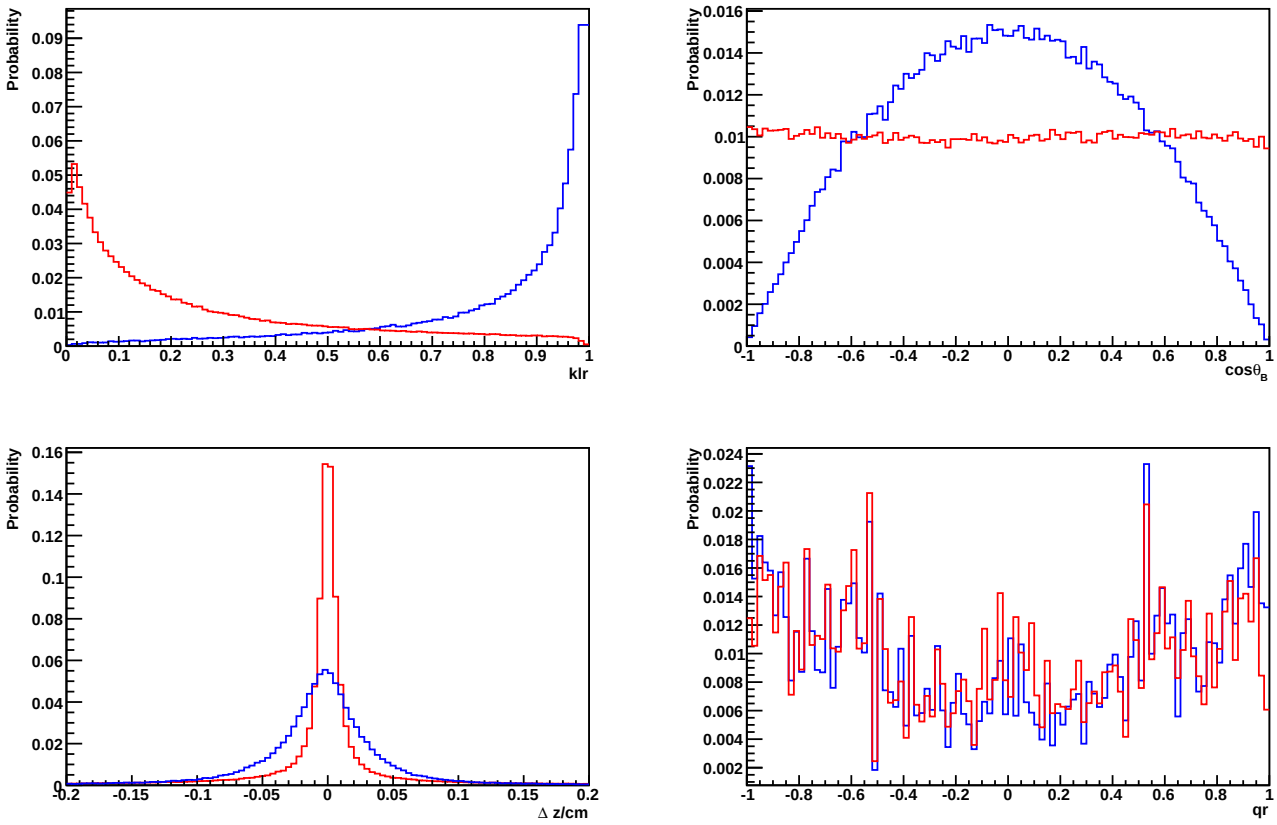

Figure 4.2: Normalized distributions of KSFW likelihood ratio, $\cos\theta_B$, Δz and quality of B flavor tag $q \cdot r$. The blue and red curves represent signal and continuum, respectively.

4.1.4 Flavor Tagging Quality

$q \cdot r$ is the charge-signed (q) quality of the B flavor tag r. The normalized distributions for signal and continuum background are shown in FIG 4.2. There is no significant distinction between signal and continuum background for $q \cdot r$. Therefore, it is not included in our combined likelihood for continuum background suppression.

4.1.5 Likelihood Ratio

We fit the data from signal and continuum MC (exp 17 for SVD1, exp 45 for SVD2) to get PDFs of klr, $\cos\theta_B$, and Δz. For a given event, we obtain the continuum-suppression likelihood $\mathcal{L}$ as the product of the three PDF values if Δz is available and less than 0.2 cm; otherwise, , $\mathcal{L}$ only incorporates the klr and $\cos\theta_B$ PDF values. The combined likelihood $\mathcal{L}_S$ for signal (or $\mathcal{L}_B$ for continuum background) is calculated as:

$$\mathcal{L}_S = \begin{cases} P_S^{SVD1}(klr) \times Q_S^{SVD1}(\cos\theta_B) \times R_S^{SVD1}(\Delta z) & (\text{for } \Delta z < 0.2\text{cm for SVD1}) \\ P_S^{SVD1}(klr) \times Q_S^{SVD1}(\cos\theta_B) & (\text{for } \Delta z \geq 0.2\text{cm for SVD1}) \\ P_S^{SVD2}(klr) \times Q_S^{SVD2}(\cos\theta_B) \times R_S^{SVD2}(\Delta z) & (\text{for } \Delta z < 0.2\text{cm for SVD2}) \\ P_S^{SVD2}(klr) \times Q_S^{SVD2}(\cos\theta_B) & (\text{for } \Delta z \geq 0.2\text{cm for SVD2}) \end{cases} \tag{4.3}$$

and $\mathcal{L}_B$ is calculated in a corresponding fashion by replacing signal PDFs with background PDFs. Using the signal and continuum background likelihoods, we calculate the likelihood ratio ($\mathcal{R}$) for each event

$$\mathcal{R} = \frac{\mathcal{L}_S}{\mathcal{L}_S + \mathcal{L}_B} \tag{4.4}$$

The $\mathcal{R}$ distributions for signal and continuum MC for events from exp 25 for SVD1 and exp 49 for SVD2 are shown in FIG 4.3.

4.1.6 Figure of Merit for Likelihood Ratio

We need to obtain the smallest statistical error fraction $\delta N_S/N_S$, where N_S is the number of signal events. Since $\delta N_S \approx \sqrt{N_S + N_B}$ in the signal region, we maximize the figure of merit $N_S/\sqrt{N_S + N_B}$. For a given $\mathcal{R}$ minimum cut, we calculate the scaled number of passed events for signal and continuum background (N_S and N_B), then scan through the range $\mathcal{R} \in (0, 1)$ with a step size of $\Delta\mathcal{R} = 0.1$ to obtain the figure of merit distribution in FIG 4.4. The summary of the optimal $\mathcal{R}_{\min}$ cut and its efficiency for SVD1 or SVD2, with or without Δz, is shown in TABLE 4.2.

Table 4.2: Summary of continuum-suppression likelihood ratio cut

Mode	$\mathcal{R}_{\rm min}$ cut	Efficiency for signal (%)	Efficiency for $q\bar{q}$ (%)
SVD1 with Δz	0.952	39.1	0.78
SVD1 w/o Δz	0.910	43.0	1.66
SVD2 with Δz	0.961	38.0	0.66
SVD2 w/o Δz	0.919	40.4	1.42

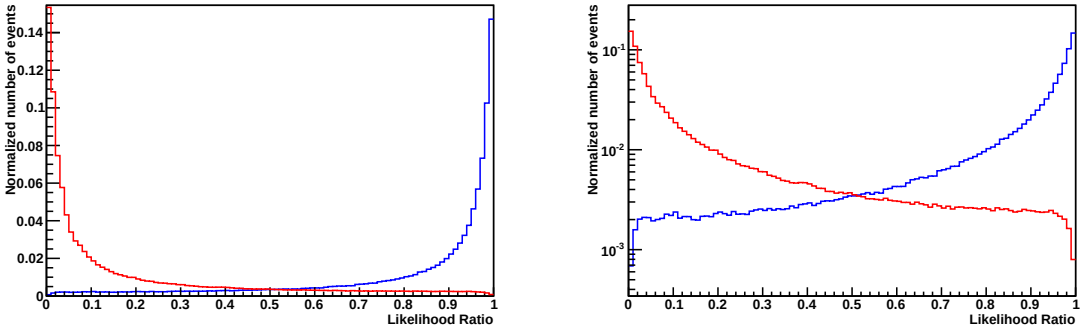

Figure 4.3: The distributions of likelihood ratio for signal (blue) and continuum background (red) with linear scale (left) and logarithmic scale (right).

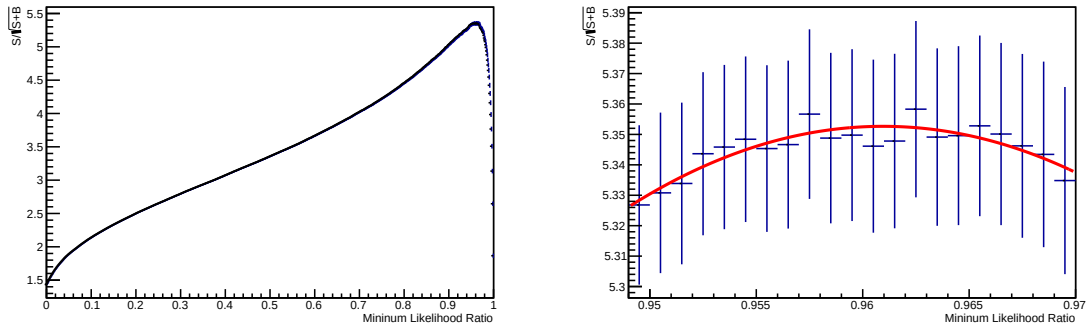

Figure 4.4: Figure of merit for the $\mathcal{R}_{\rm min}$ cut in the entire range (left) and near the peak (right) to locate the optimal value.

4.2 $B\bar{B}$ Background Suppression

4.2.1 $B\bar{B}$ Background

In additional to the continuum background, we also have backgrounds from $B\bar{B}$ events. There are 4 major $B\bar{B}$ background involved: $B^{\pm} \to \bar{D}^0 h^{\pm}$, $B^{\pm} \to J/\psi h^{\pm}$, $B^{\pm} \to \psi(2S) h^{\pm}$, and $B^{\pm} \to K^0_S h^{\pm}$, where $h^{\pm}$ is charged pion or kaon. We use MC data for those modes and make additional cuts on the tracks forming the B candidate as the prerequisite: π/K likelihood $L_{\pi/K} > 0.3$, and electron-identification likelihood $L_{e/\pi} < 0.9$.

$B^{\pm} \to \bar{D}^0 h^{\pm}$ Background

The branching fraction for $B^{\pm} \to \bar{D}^0 \pi^{\pm}$ and $B^{\pm} \to \bar{D}^0 K^{\pm}$ are $(4.81 \pm 0.15) \times 10^{-3}$ and $(3.70 \pm 0.17) \times 10^{-4}$, respectively [1]. Then $\bar{D}^0$ can decay to $\pi^+\pi^-((1.402 \pm 0.026) \times 10^{-3})$, $K^+K^-((3.96 \pm 0.08) \times 10^{-3})$, $K^+\pi^-((3.88 \pm 0.05) \times 10^{-2})$, or $\pi^+K^-((1.380 \pm 0.028) \times 10^{-4})$. The PID likelihood cut $L_{\pi/K} > 0.3$ eliminates $\sim 90\%$ true kaons and $\sim 8\%$ true pions for each track. Then the ratio for the number of events for the final states ($\pi\pi\pi$, $\pi\pi K$, πKK and KKK) can be estimated as shown in TABLE 4.3.

Table 4.3: $B^{\pm} \to \bar{D}^0 h^{\pm}$ final states comparison. The ratio shows the amount of each mode corresponding to one $\pi\pi\pi$ event in the final state.

Final state (unordered)	Ratio	Ratio after $L_{\pi/K}$ cut
$\pi\pi\pi$	$\equiv 1.0$	$\equiv 1.0$
$\pi\pi K$	28	3.0
πKK	5.0	0.059
KKK	0.22	0.00028

The number of $\pi\pi K$ events is approximately 3 times that of $\pi\pi\pi$ events, and very few

πKK and KKK events remain. The Dalitz plot for all these modes is shown in FIG B.1(a). The curved horizontal band is caused by $\pi\pi K$ events with misassignment of the pion mass to the true kaon(s). The PDFs describing the Dalitz plot , M_{bc}, and ΔE for this background are shown in Appendix B.1.

$B^{\pm} \to J/\psi h^{\pm}$ Background

In the decay $B^{\pm} \to J/\psi h^{\pm}$, J/ψ decays to $l^{+}l^{-}$ and the leptons may be misidentified as pions. After applying the lepton-ID requirements, approximately 40% of such events remain. The Dalitz plot is shown in FIG B.4(a). The PDFs describing the Dalitz plot, M_{bc}, and ΔE for these backgrounds are shown in Appendix B.2.

$B^{\pm} \to \psi(2S) h^{\pm}$ Background

In the decay $B^{\pm} \to \psi(2S)h^{\pm}$, $\psi(2S)$ may decay to $l^{+}l^{-}$ and the leptons may again be misidentified as pions. After applying the lepton-ID requirements, approximately 37% of such events remain. The Dalitz plot is shown in FIG B.6(a). The PDFs describing the Dalitz plot, M_{bc}, and ΔE for this background are shown in Appendix B.3.

$B^{\pm} \to K^{0}_{S} h^{\pm}$ Background

Following the decay $B^{\pm} \to K^{0}_{S} h^{\pm}$, K^{0}_{S} decays half the time to $\pi^{+}\pi^{-}$ giving the $\pi\pi h$ final state as a source of background. After applying the pion-kaon likelihood cut, approximately 94% of such events remain since the branching fraction for $B^{\pm} \to K^{0}_{S}\pi^{\pm}$ is much higher than that for $B^{\pm} \to K^{0}_{S}K^{\pm}$. The Dalitz plot is shown in FIG B.7(a). The PDFs describing the Dalitz plot, M_{bc}, and ΔE for this background are shown in Appendix B.4.

4.2.2 Cut Method vs. No-Cut Method for $B\bar{B}$

The 4 modes of $B\bar{B}$ background can be removed by cutting the corresponding bands in the Dalitz plot. An alternative method models each mode with the proper PDF and then uses a fitting method over the entire Dalitz plot to extract the signal. A sensitivity study is performed to determine the preferred method.

Cut Method

In each mode, the horizontal band and vertical band in the Dalitz plot is projected onto vertical (m_{23}^2) axis and horizontal (m_{12}^2) axis, respectively. Then we fit the projection with a 1-D analytical function and determine the range around the central value that covers $\sim 99\%$ area under the curve. The cuts for each mode are shown in TABLE 4.4 and FIG 4.5.

Table 4.4: Summary of cuts on Dalitz plot for $B\bar{B}$ background

Mode	Low Cut (GeV/c^2)	High Cut (GeV/c^2)
$B^{\pm} \to \bar{D}^0 h^{\pm}$ horizontal band	1.550	1.920
$B^{\pm} \to \bar{D}^0 h^{\pm}$ vertical band	1.660	1.960
$B^{\pm} \to J/\psi h^{\pm}$ horizontal band	3.024	3.158
$B^{\pm} \to J/\psi h^{\pm}$ vertical band	3.020	3.158
$B^{\pm} \to \psi(2S) h^{\pm}$ vertical band	3.578	3.753
$B^{\pm} \to K_S^0 h^{\pm}$ horizontal band	0.474	0.522

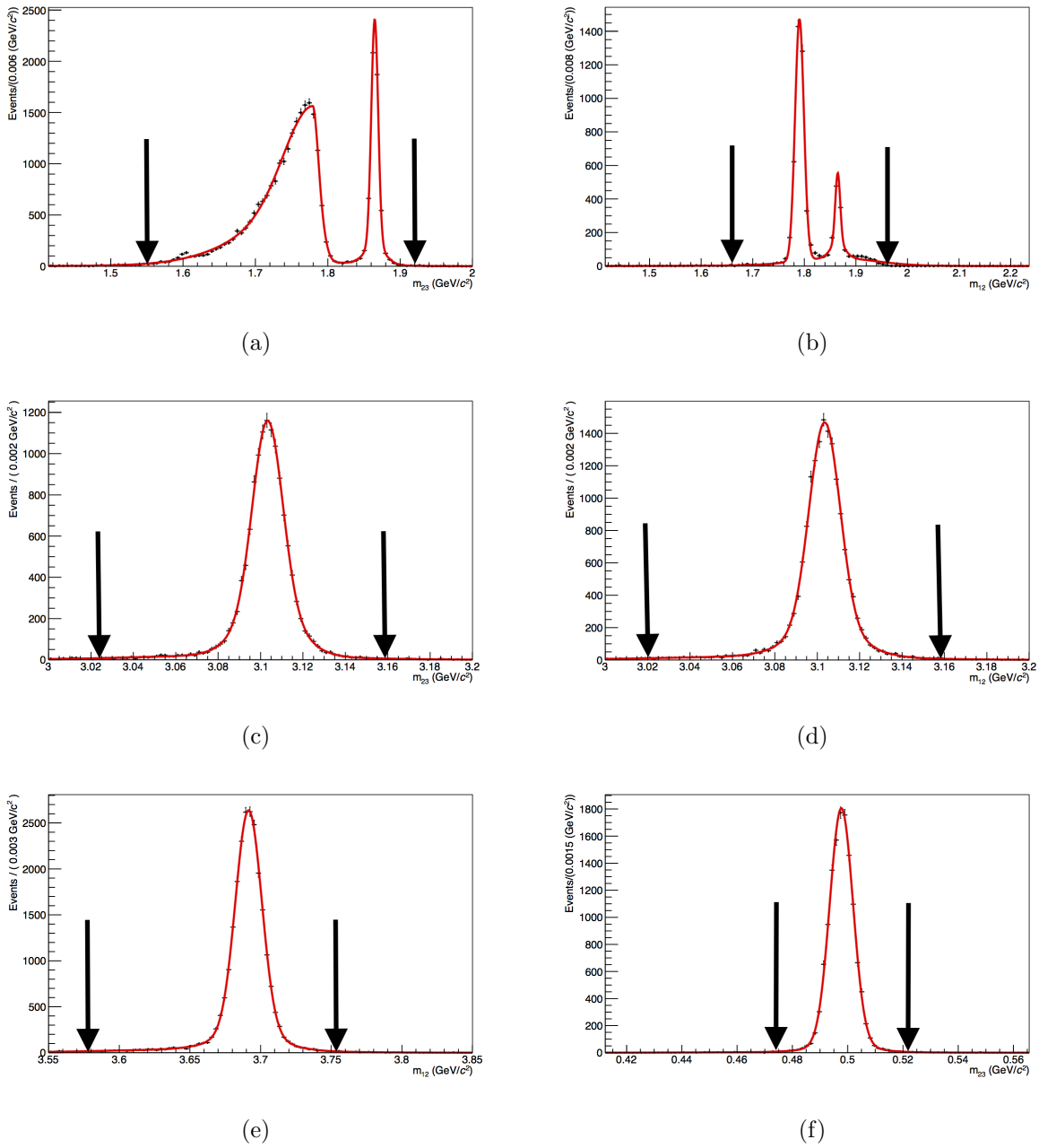

Figure 4.5: Cuts on $B\bar{B}$ background Dalitz plot in each mode are shown as arrows in each plot: (a) cuts on $B^{\pm} \to \bar{D}^0 h^{\pm}$ horizontal band; (b) cuts on $B^{\pm} \to \bar{D}^0 h^{\pm}$ vertical band; (c) cuts on $B^{\pm} \to J/\psi h^{\pm}$ horizontal band; (d) cuts on $B^{\pm} \to J/\psi h^{\pm}$ vertical band; (e) cuts on $B^{\pm} \to \psi(2S) h^{\pm}$; (f) cuts on $B^{\pm} \to K^0_S h^{\pm}$.

No-Cut Method

The cut method removes most of the $B\bar{B}$ background events in the several bands in the Dalitz plot but also suppresses the signal efficiency—and so worsens the statistical accuracy—by removing some signal events in those regions. The no-cut method avoids this problem by fitting the MC data for each $B\bar{B}$ background mode and obtain the parameters of all the analytical functions needed to describe the Dalitz plot. The Dalitz-plot PDFs for all of the $B\bar{B}$ backgrounds are shown in Appendix B. Using these PDFs along with those for signal and continuum background, we can extract the signal in a fit to the entire Dalitz region.

Sensitivity Study

To decide which method is preferred, we perform a sensitivity study for each. In a pseudo-experiment, we synthesize a certain amount of data (according to the branching fraction and luminosity) from the 4-D PDFs (Dalitz plot, M_{bc}, and ΔE) in each mode, then fit this data sample using the 4-D PDFs to extract the signal yield. For CP sensitivity, we treat B^+ and B^- separately.

To study the stability of the fit, we sample the initial number of events in each mode according to the Poisson distribution and repeat the fitting procedure for 1000 pseudo-experiments. In each case we compare the number of events for B^+ and B^- before and after the fitting, then calculate the asymmetry:

$$\mathcal{A}_{CP} = \frac{N_{B^-} - N_{B^+}}{N_{B^-} + N_{B^+}}, \tag{4.5}$$

where N_{B^+} and N_{B^-} are the fitted signal yields for positive and negative B charge, respectively. The results before and after the fitting are

$$\mathcal{A}_{CP} = \begin{cases} (7.0 \pm 0.6) \times 10^{-3} & \text{(before fitting)} \\ (5.7 \pm 0.6) \times 10^{-3} & \text{(after fitting)} \end{cases} \tag{4.6}$$

We repeat the fitting procedure but start from different initial $\mathcal{A}_{CP}$ value by adjusting N_{B^+} and N_{B^-} to make $\mathcal{A}_{CP}$ to be either twice the nominal value or approximately 0 to obtain 3

points for the linearity test of the no-cut method. The linear fit to these 3 points is shown in FIG 4.6.

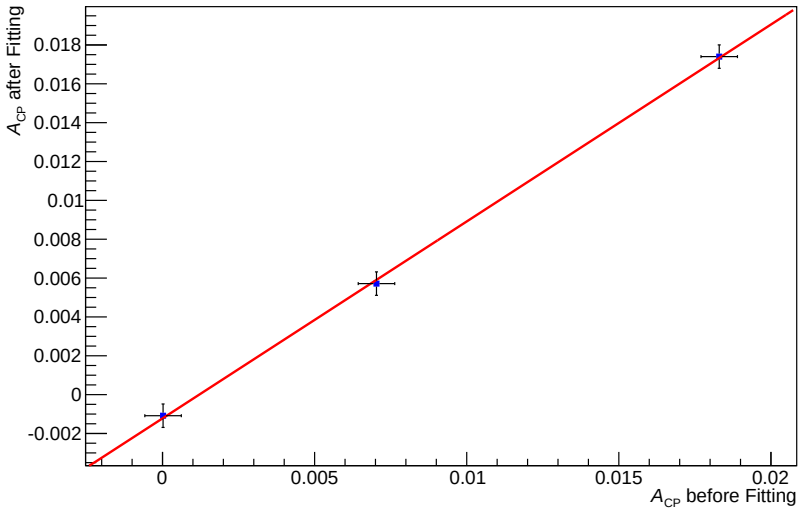

Figure 4.6: Linear fit on $\mathcal{A}_{\mathrm{CP}}$ for no-cut method.

Similarly, we repeat the steps above for the cut method and obtain the 3-point linear fit as shown in FIG 4.7.

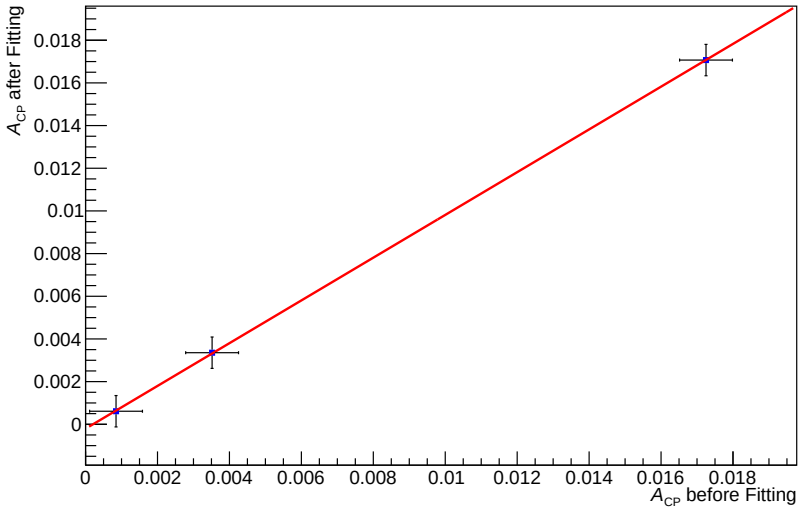

Figure 4.7: Linear fit on $\mathcal{A}_{\mathrm{CP}}$ for cut method.

The comparison between the linearity tests are shown in TABLE 4.5.

Table 4.5: Linearity tests' 3-point linear-fit results for no-cut and cut methods

Method	Slope	Intercept
No-cut	1.014 ± 0.065	$(-1.22 \pm 0.74) \times 10^{-3}$
Cut	1.002 ± 0.083	$(-0.20 \pm 0.85) \times 10^{-3}$

In both cases, the linearity of $\mathcal{A}_{\mathrm{CP}}$ before and after the fitting procedure demonstrates the validity of the fitting procedure. The linear function should be close to $y = x$ which means the fitting result reflects the original data affectively. Therefore, the cut method with slope closer to 1 and intercept closer to 0 is the preferred method for the signal extraction.

4.3 Rare B Decay Background

4.3.1 Background from Charged Rare B Decay Modes

We skim the 50 streams of charged rare B MC data from Exp 7 to 65 with the requirements $M_{bc} > 5.2$ GeV/c^2 and $|\Delta E| < 0.3$ GeV. Then we apply continuum background suppression; approximately 28% of the skimmed data passes. We then apply the cuts on PID, track information, and the Dalitz plot. We also apply the "isTrueB" cut which only keeps non-signal rareB backgrounds according to the MC generation information. The distribution of M_{bc} and ΔE after those cuts are shown in FIG 4.8.

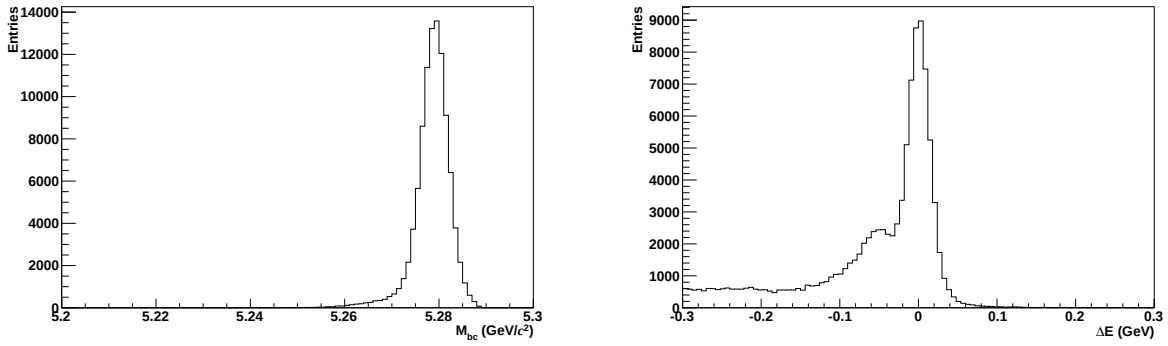

(a) (b)

Figure 4.8: (a)M_{bc} and (b) ΔE distributions for charged rare B decay modes after continuum and $B\bar{B}$ background suppression.

In the ΔE distribution, there is a peak at $\Delta E = 0$ that will contaminate the signal. This peak is due to several modes like $B^{\pm} \to X^0 h^{\pm}$ and $X^0 \to h'^{+} h''^{-}$ with charged hhh final states in the charged rare B decay. We note that there are 7 such modes in the Particle Date Group (PDG) table [1] with an intermediate neutral particle given by X^0's are $f_0(1710)$, $f_0(1370)$, $f_0(600)$, $\rho(770)^0$, $\rho(1450)^0$, $\rho(1700)^0$, and $f_2(1270)$. The ΔE distributions for these modes are shown in Appendix C. After removing those modes from the rare-B MC data set, the M_{bc}, ΔE and Dalitz plots are shown in FIG 4.9. The peak at $\Delta E = 0$ is no longer

present.

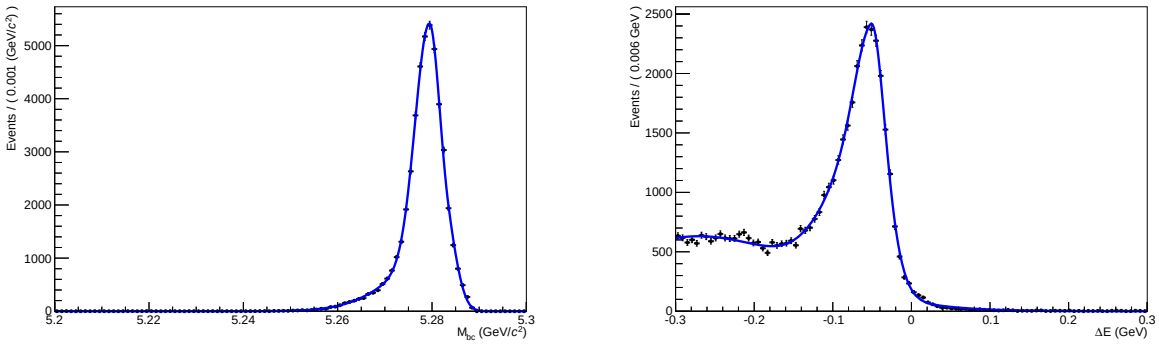

(a) (b)

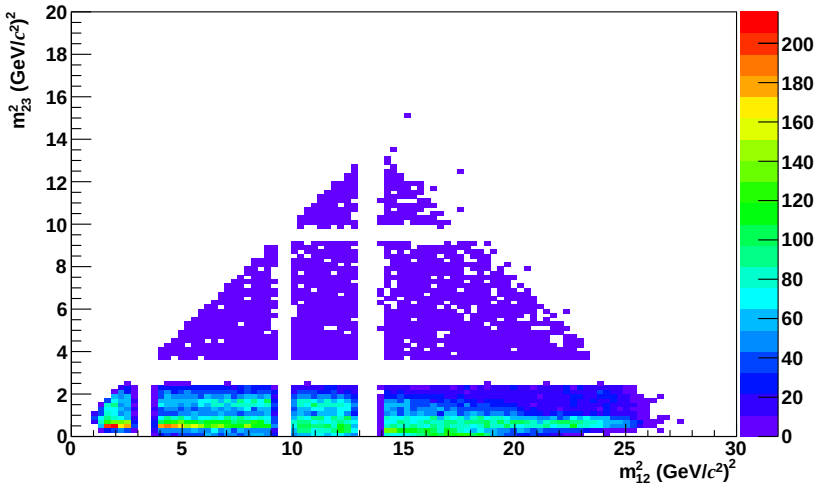

(c)

Figure 4.9: Distributions for charged rare B decay after continuum suppression, $B\bar{B}$ background suppression, and removal of rare B modes with ΔE centered at 0: (a) M_{bc} and its fitting function; (b) ΔE and its fitting function; (c) Dalitz plot.

4.3.2 Background from Neutral Rare B Decay Modes

For the events from the rare decay modes of the neutral B meson, we obtain a few charged B candidates mis-reconstructed by the incorrect combination of three charged tracks. We

follow the same selection steps as for the charged rare B sample. The M_{bc}, ΔE and Dalitz plots are shown in FIG 4.10.

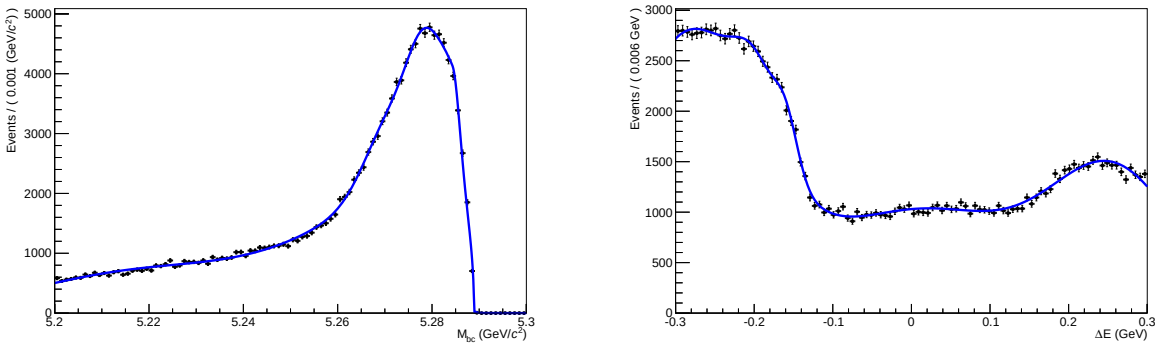

(a) (b)

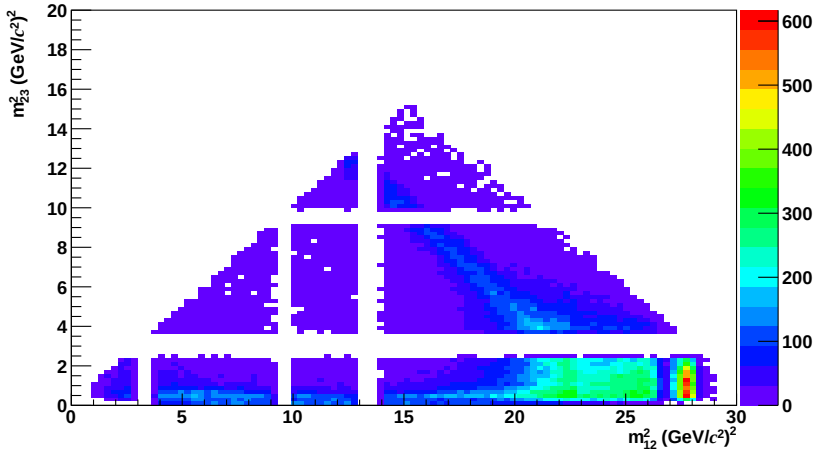

(c)

Figure 4.10: Distributions for neutral rare B decay after background suppression: (a) M_{bc} and its fitting function; (b) ΔE and its fitting function; (c) Dalitz plot.

Chapter 5

Signal Extraction

5.1 Selection Criteria

In addition to the likelihood ratio cut for continuum suppression and the cuts on Dalitz plot to remove major $B\bar{B}$ background, TABLE 5.1 summarizes all the other selection criteria for the real data. We apply the same conditions on MC simulation data to obtain the PDFs describing the signal and background remaining in the real data.

Table 5.1: Summary of selection criteria in addition to continuum and $B\bar{B}$ suppression

Category	Requirement
Charged tracks	$\lvert dr\rvert < 0.2$ cm
	$\lvert dz\rvert < 3$ cm
	$p_T > 0.1$ GeV
Particle ID	$L_\pi/(L_\pi + L_K) > 0.6$
	electron likelihood < 0.9

From the Monte Carlo simulation for each mode, we model the signal and each type of background over the two-dimensional $M_{bc} - \Delta E$ region of 5.2 GeV/c^2 $< M_{bc} <$ 5.3 GeV/c^2,

-0.3 GeV $< \Delta E < 0.3$ GeV. Then we extract the signal yields from the real data by using an unbinned maximum likelihood fit.

5.2 Probability Density Function

5.2.1 PDFs for Signal

We model the M_{bc} and ΔE distributions from the signal Monte Carlo simulation, which are shown in FIG 5.1 and FIG 5.2, using a Gaussian function and a Breit-Wigner function [54]. The The Breit-Wigner function is

$$f(E) = \frac{k}{(E^2 - M^2)^2 + M^2\Gamma^2} \tag{5.1}$$

where k is a constant of proportionality:

$$k = \frac{2\sqrt{2}M\Gamma\gamma}{\pi\sqrt{M^2 + \gamma}} \quad \text{with } \gamma = \sqrt{M^2(M^2 + \Gamma^2)}. \tag{5.2}$$

The Breit-Wigner function is a Gaussian-like function with peak at $E = M$ and width Γ but with broader tails. It is frequently used to model resonances in high-energy physics.

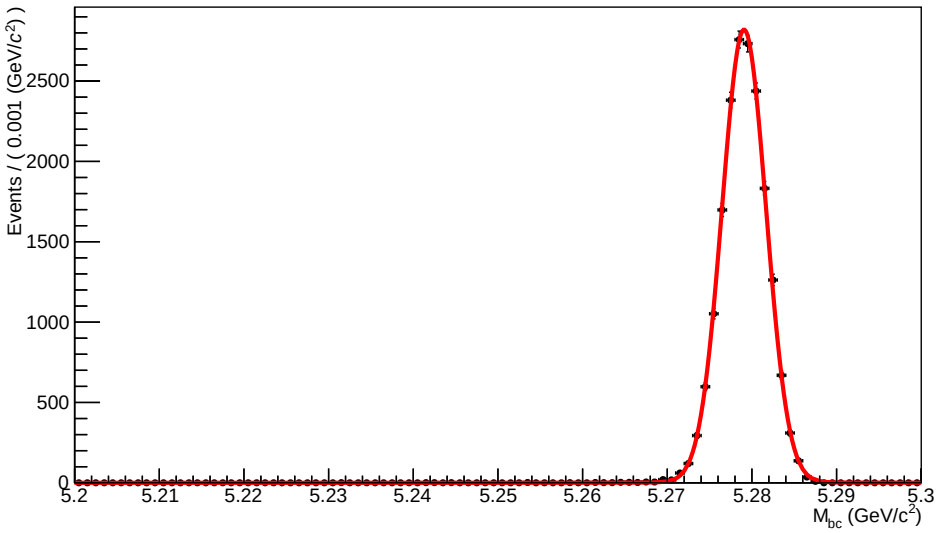

Figure 5.1: PDF for M_{bc} of signal

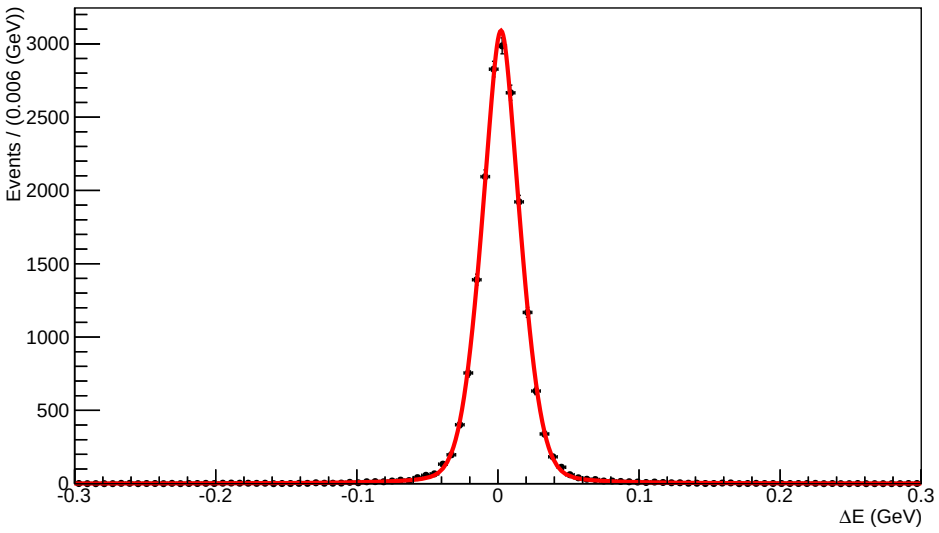

Figure 5.2: PDF for ΔE of signal

The 2-D scatter plot for M_{bc}-ΔE of signal is shown in FIG 5.3. Since there is no correlation between M_{bc} and ΔE, we use the product of M_{bc} PDF and ΔE PDF to model the

signal.

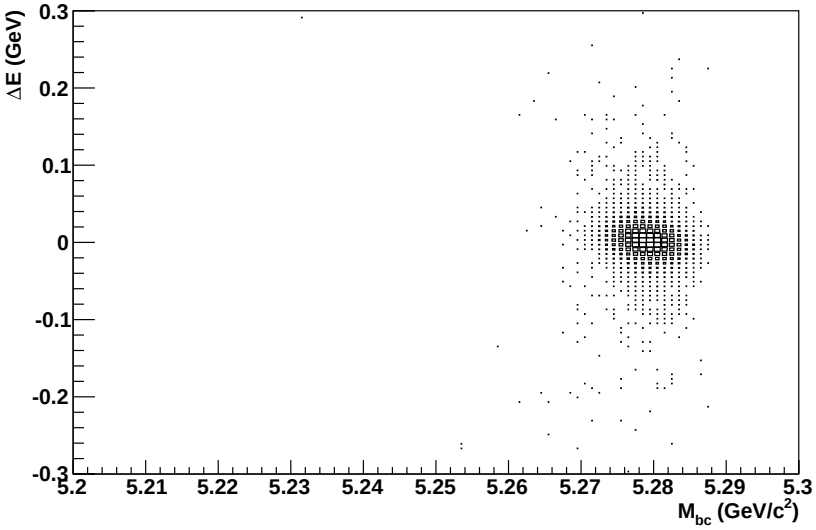

Figure 5.3: 2-D scatter plot for M_{bc}-ΔE distribution of signal.

5.2.2 PDFs for Continuum Background

Since the continuum process is the dominant background, many continuum events remain in the real data even after the continuum suppression. We model the M_{bc} and ΔE distributions for continuum background using an ARGUS function [55] [56] and a second-order polynomial, respectively. The ARGUS function is

$$f(x;\chi,c) = \frac{\chi^3}{\sqrt{2\pi}\Psi(\chi)} \cdot \frac{x}{c^2}\sqrt{1-\frac{x^2}{c^2}}\exp\left(-\frac{1}{2}\chi^2\left(1-\frac{x^2}{c^2}\right)\right) \tag{5.3}$$

where $0 \leq x < c$, $\Psi(\chi) = \Phi(\chi) - \chi\phi(\chi) - \frac{1}{2}$. Here χ is the "shape" parameter, which affects the curvature of the function; c is the "cutoff" parameter that determines the location where the function decreases to 0; and $\Phi(\chi)$ and $\phi(\chi)$ are the cumulative distribution and probability density functions of the standard normal distribution, respectively. The distributions of $M_{\rm bc}$ and ΔE for continuum are shown in FIG 5.4 and 5.5.

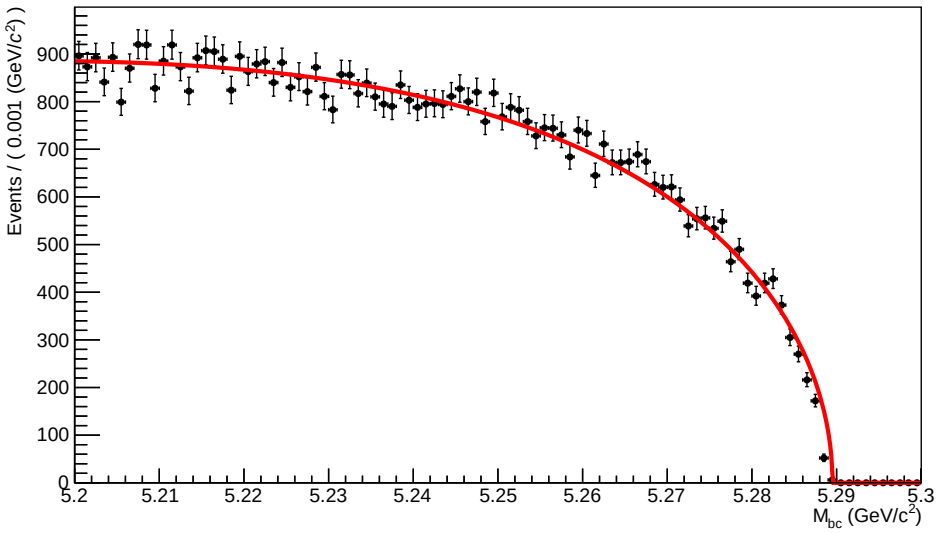

Figure 5.4: PDF for M_{bc} of continuum background

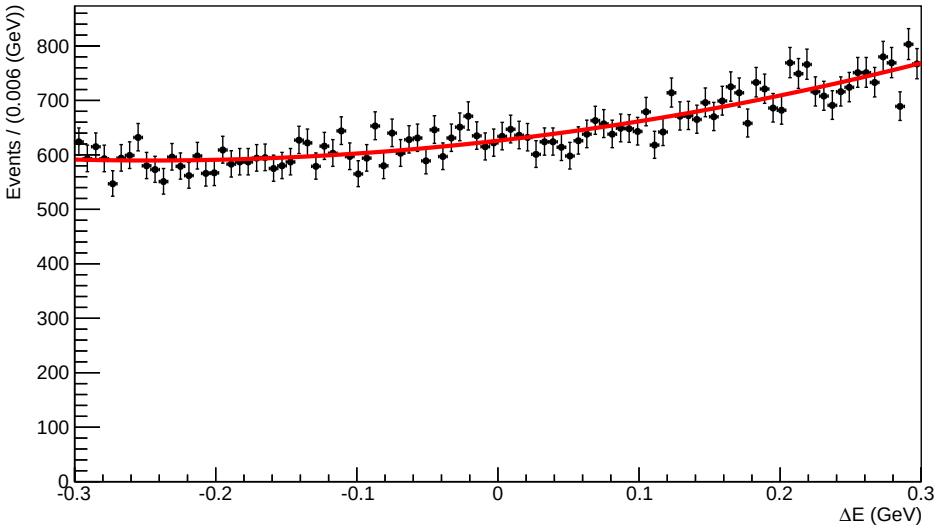

Figure 5.5: PDF for ΔE of continuum background

The 2-D scatter plot for M_{bc}-ΔE of continuum background is shown in FIG 5.6. Since there is no correlation between M_{bc} and ΔE, we use the product of M_{bc} PDF and ΔE PDF

to model the continuum.

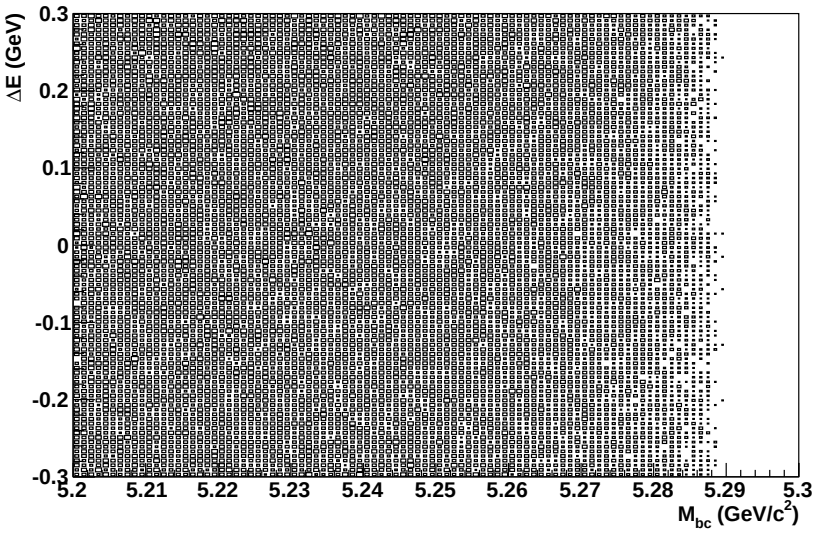

Figure 5.6: 2-D scatter plot for M_{bc}-ΔE distribution of continuum background.

5.2.3 PDFs for rare B Background

The rare B background is the convolution of many rare decay modes. The distributions for charged and neutral rare B decay modes are shown in FIG 4.10 and FIG 4.10. The ad hoc fitting functions that model these distributions for M_{bc} and ΔE are shown in TABLE 5.2. Since there is some correlation between M_{bc} and ΔE for rare-B distribution, we use the PDF sampled from 2-D histogram of M_{bc}-ΔE instead of product of 1-D histogram. The 2-D scatter plots for M_{bc}-ΔE of charged and neutral rare-B are shown in FIG 5.7 and 5.8.

Table 5.2: Configuration of fitting functions for rare B decay modes

Mode	Components of the PDF
M_{bc} of charged rare-B	2 asymmetric Gaussians
ΔE of charged rare-B	asymmetric Gaussian + 2 Gaussians
M_{bc} of neutral rare-B	ARGUS + asymmetric Gaussian + 3 Gaussians
ΔE of neutral rare-B	5 Gaussians

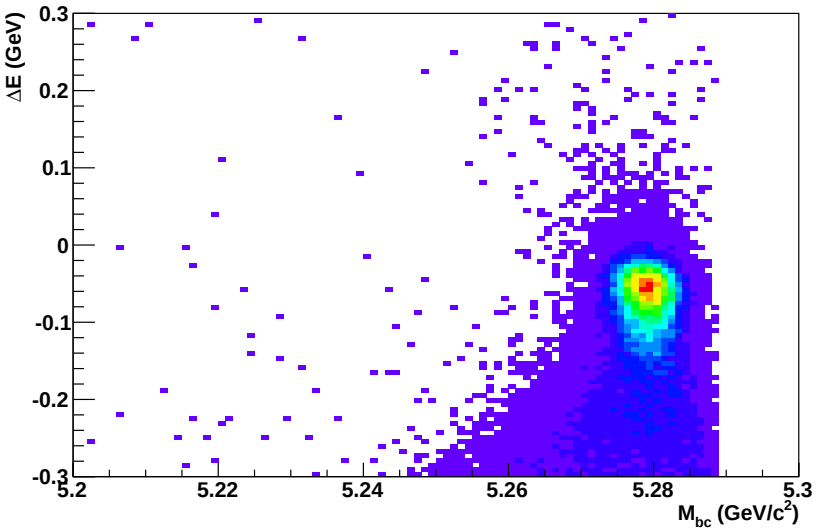

Figure 5.7: 2-D scatter plot for M_{bc}-ΔE distribution of charged rare-B background.

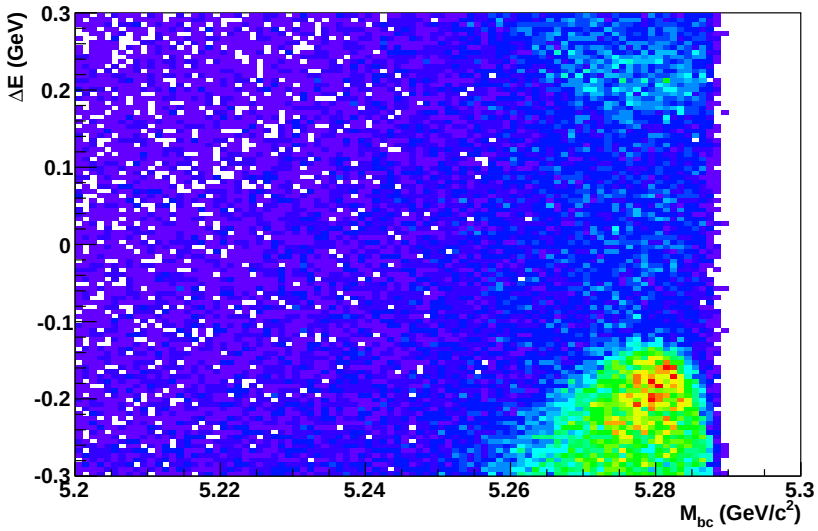

Figure 5.8: 2-D scatter plot for M_{bc}-ΔE distribution of neutral rare-B background.

5.3 Signal Extraction

The signal yield is extracted by fitting the number of events for signal and background from experiments 7 to 13, which contains $(31.769 \pm 0.348) \times 10^6$ $B\bar{B}$ pairs, with the PDFs described in the last section. This subset of data was chosen to match the original Belle analysis of this mode (using a pseudo-two-body final state $\rho\pi$) to verify that the results from our procedure are consistent with those from the original analysis. The signal yield is extracted using an unbinned maximum-likelihood fit. The likelihood function [12] is given by

$$\mathcal{L} = e^{-N} \times \prod_{J}^{N_e} \left(\sum_{k} N_k \mathcal{P}_k^j(M_{bc}, \Delta E, q_B) \right), \tag{5.4}$$

where N is equal to $\sum_k N_k$, N_k is the yield for the event category k, N_e is the total number of event in the data sample, and $\mathcal{P}_k^j$ is the 2-D PDF for the category k for event j. The function $-2\ln\mathcal{L}$ is minimized in a fit to the data.

The fitting result for B^+ and B^- are shown in TABLE 5.3 and TABLE 5.4, respectively.

The signal efficiency is estimated by a study of signal Monte Carlo sample. For the SVD1 subsample, the overall cut efficiencies for B^+ and B^- are 11.36% and 10.95%, respectively.

Table 5.3: Fitting result and signal yield for $B^+ \to \pi^+\pi^-\pi^+$ in experiments 7-13

Mode	Fitting result
$B^+ \to \pi^+\pi^-\pi^+$	$18.5^{+6.7}_{-5.8}$
continuum background	2291^{+57}_{-57}
charged rare-B background	3^{+10}_{-9}
neutral rare-B background	100^{+36}_{-34}

Table 5.4: Fitting result and signal yield for $B^- \to \pi^+\pi^-\pi^-$ in experiments 7-13

Mode	Fitting result
$B^- \to \pi^+\pi^-\pi^-$	$14.6^{+5.9}_{-5.2}$
continuum background	2018^{+54}_{-52}
charged rare-B background	16^{+12}_{-10}
neutral rare-B background	97^{+33}_{-32}

Chapter 6

Systematic Uncertainty

6.1 PID Systematic Error

The PID systematic error arises from π/K and electron identification involved in this analysis.

6.1.1 Systematic Error from π/K Identification

The π/K efficiency are obtained from the study of the decay $D^{*+} \to D^0\pi^+$ followed by $D^0 \to K^-\pi^+$ [57] [58]. Note that the true kaon's charge is opposite that of the grandparent D^{*+}. The kinematics of the two successive two-body decays, particularly with the slow pion from the D^{*+}, allows the event to be reconstructed with excellent signal/noise ratio without relying on explicit PID information. The kaon identification efficiency ϵ_K is defined as

$$\epsilon_K = \frac{\text{number of } K \text{ tracks identified as } K}{\text{number of } K \text{ tracks}} \tag{6.1}$$

while the pion mis-identification rate f for the kaon identification is defined as

$$f_K = \frac{\text{number of } K \text{ tracks identified as } K}{\text{number of } \pi \text{ tracks}} \tag{6.2}$$

K/π identification is then applied to each track using the likelihood ratio based on the likelihood information from the ACC, TOF, and CDC. Since the efficiency and fake rate depend upon the momentum magnitude and direction of the tracks, four values and their uncertainties (i.e., KID efficiency for K, KID mis-identification rate for π, π ID efficiency for π and π ID mis-identification rate for K) are tabulated for 384 momentum and $\cos\theta$ bins as well as 9 thresholds for the K/π likelihood ratio (likelihood ratio $> 0.1, 0.2, \cdots, 0.9$).

For a given π/K likelihood ratio threshold, three quantities are tabulated for each momentum and angular bin: MC efficiency $\epsilon^{\rm MC}$, data efficiency $\epsilon^{\rm data}$, and efficiency ratio $r = \epsilon^{\rm data}/\epsilon^{\rm MC}$. The efficiency ratio for our analysis is estimated by taking the weighted mean:

$$R = \sum_l n_l R_l / \sum n_l, \tag{6.3}$$

where l is the bin index, R_l is the efficiency ratio in bin l obtained from the D^* sample, and n_l is the number of tracks that fall in the bin l in our signal mode.

For the π/K likelihood ratio cut in our analysis of $\mathcal{L}_{\pi/K} > 0.6$, we obtain an efficiency correction of 0.954 ± 0.018.

6.1.2 Systematic Error from Electron Identification

The correction and the systematic error of the electron identification efficiency is obtained by the study of $\gamma\gamma \to e^+e^-$ [59] [60]. The efficiency (ϵ) is the number of electrons which satisfy the electron ID (eID) cut. divided by the total number of electrons [61]. The efficiency in several categories is calculated:

- 5 eID thresholds: 0.1, 0.5, 0.6, 0.8, and 0.9;
- 10 momentum (p) bins of 0.5 GeV/c width from 0 to 5 GeV/c in the laboratory frame;
- 7 polar angle (θ) regions in the laboratory frame:
  $(18°, 25°)$, $(25°, 35°)$, $(40°, 60°)$, $(60°, 125°)$, $(125°, 132°)$, $(132°, 151°)$.

For each p, θ bin and eID threshold, the statistical efficiency error is calculated as

$$\sigma_{(\mathrm{stat})i} = \sqrt{\epsilon_i \cdot (1-\epsilon_i)/N_i} \tag{6.4}$$

where N_i is the total number of electrons in the bin i before applying the electron ID cut.

For the electron ID cut for each track in our analysis of $eID < 0.9$, we obtain an efficiency correction of 0.975 ± 0.081.

6.2 Likelihood Ratio Systematic Error

The efficiency correction for the continuum suppression likelihood ratio cut is obtained by using $B \to D^0\pi$, $D^0 \to K\pi$ decay in Monte Carlo simulation and real data [61]. These decay can be selected with good signal to noise using invariant mass cuts ($|m_{ij} - m_{D^0}| < 1\mathrm{MeV}$) and π/K identification. The effect of the likelihood ratio cut in data and MC is determined by extracting the M_{bc} yield before and after the continuum suppression for both MC and data. FIGs 6.1 and 6.2 shows the likelihood ratio cut effects on M_{bc} distributions in the MC and data, respectively. The efficiencies in MC and data and their ratio are:

$$\epsilon^{\mathcal{R}}_{\mathrm{MC}} = 0.360 \pm 0.008, \quad \epsilon^{\mathcal{R}}_{\mathrm{data}} = 0.373 \pm 0.029, \quad \frac{\epsilon^{\mathcal{R}}_{\mathrm{data}}}{\epsilon^{\mathcal{R}}_{\mathrm{MC}}} = 1.04 \pm 0.08 \tag{6.5}$$

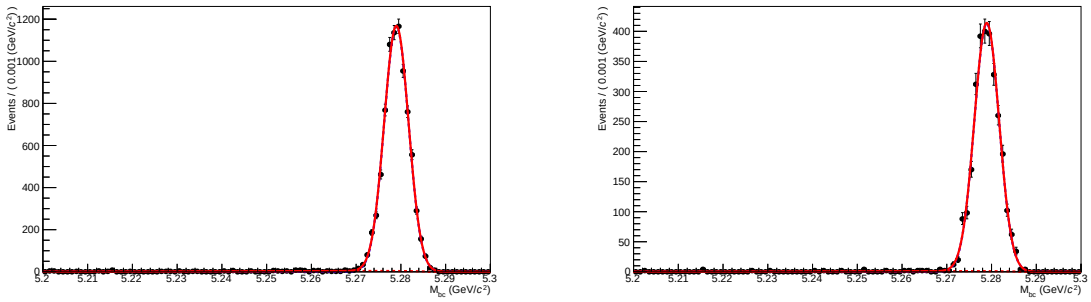

(a) (b)

Figure 6.1: The M_{bc} distributions for $B \to D^0\pi, D^0 \to K\pi$ events in MC before (left) and after (right) the continuum suppression likelihood ratio cut has been applied.

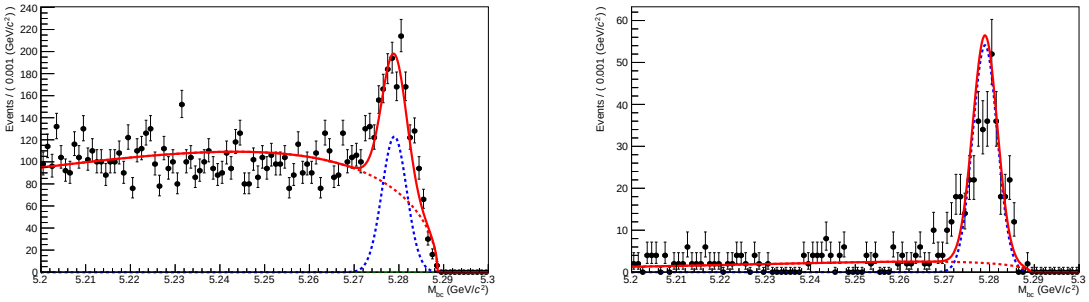

(a) (b)

Figure 6.2: The M_{bc} distributions for $B \to D^0\pi, D^0 \to K\pi$ events in data before (left) and after (right) the continuum suppression likelihood ratio cut has been applied.

6.3 Systematic Error from Fitting Parameters

The uncertainties of the background shapes in the fitting procedure give rise to some systematic error in the extracted signal yield. The error is obtained by varying the fixed shape parameters by $\pm 1\sigma$ and repeating the fit. TABLE 6.1 shows the change of the signal yield caused by each such movement of the parameters in the continuum PDFs.

Table 6.1: Change of signal yield caused by adjusting the parameters for the continuum PDFs by $\pm 1\sigma$.

Parameter	$-1\sigma(B^+)$	$+1\sigma(B^+)$	$-1\sigma(B^-)$	$+1\sigma(B^-)$
Continuum M_{bc} ARGUS threshold	0.016%	0.039%	−0.002%	−0.006%
Continuum M_{bc} ARGUS shape	−0.251%	0.201%	-0.288%	0.282%
Continuum ΔE Polynomial a_0	0.279%	−0.207%	0.202%	0.080%
Continuum ΔE Polynomial a_1	−0.512%	0.594%	−0.270%	0.457%

Similarly, there are 53 parameters for the rare B background PDFs. The change of signal yield caused by 1σ fluctuation of those parameters are shown in Appendix D. After

combining the errors in the table in quadrature, the fitting systematic errors for B^+ and B^- are (-3.2%, $+2.7\%$) and (-2.8%, $+3.1\%$), respectively.

6.4 Other Systematic Errors

The tracking uncertainty is evaluated from the study of high momentum tracks with $P_T > 200$ MeV/c [62]. The track finding efficiency is measured by comparing the number of partially and fully reconstructed D^* decays; the related efficiency ratio is

$$\frac{\epsilon^{\rm trk}_{\rm data}}{\epsilon^{\rm trk}_{\rm MC}} = 0.9987 \pm 0.009 \tag{6.6}$$

The uncertainty on the number of $B\bar{B}$ events is 1.37%, based on the data of $(772\pm11)\times10^6$ $B\bar{B}$ pairs. For the partial data set (experiments 7–13) that we use to extract the signal, the uncertainty is 1.1%: we have $(31.77 \pm 0.35) \times 10^6$ $B\bar{B}$ pairs. The branching fraction for $\Upsilon(4S) \to B^+B^-$ is $51.4 \pm 0.6\%$ [1]. Therefore, the number of charged $B\bar{B}$ pairs before the decay is $16.33 \pm 0.26 \times 10^6$.

Chapter 7

Conclusions

The study of signal MC shows that the efficiency of all the cuts for B^+ and B^- are 11.4% and 10.9%, respectively. From the systematic error study, we obtain the efficiency ratios $r = \epsilon_{\rm data}/\epsilon_{\rm MC}$ for KID, eID, likelihood ratio ($\mathcal{R}$), and track finding (trk), as summarized in TABLE 7.1.

Table 7.1: Summary of efficiency ratios from the study of systematic error.

$r_{\rm KID}$	0.954 ± 0.018
$r_{\rm eID}$	0.975 ± 0.081
$r_{\mathcal{R}}$	1.036 ± 0.084
$r_{\rm trk}$	0.9987 ± 0.0009

TABLE 7.2 shows the signal yield for B^+ and B^-, including statistical and systematic errors. The systematic error for the fitting result is obtained by varying the fixed shape parameters by $\pm 1\sigma$ and repeating the fit, as described in Section 6.3. The cut efficiency for data is adjusted according to these efficiency ratios as

$$\epsilon_{\rm data} = \epsilon_{\rm MC} \times r_{\rm KID} \times r_{\rm eID} \times r_{\mathcal{R}} \times r_{\rm trk}, \tag{7.1}$$

and its systematic error is calculated accordingly.

Table 7.2: Fitting result and signal yield for $B^{\pm} \to \pi^+\pi^-\pi^{\pm}$

Mode	Signal Yield	Efficiency
$B^+ \to \pi^+\pi^-\pi^+$	$18.5^{+6.7}_{-5.8}(\text{stat.})^{+0.5}_{-0.6}(\text{syst.})$	$(10.9 \pm 1.3)\%$
$B^- \to \pi^+\pi^-\pi^-$	$14.6^{+5.9}_{-5.2}(\text{stat.}) \pm 0.4(\text{syst.})$	$(10.5 \pm 1.2)\%$

TABLE 7.3 shows the branching fraction and raw asymmetry $\mathcal{A}_{CP}$ for $B^{\pm} \to \pi^{\pm}\pi^+\pi^-$ based on the signal yield and efficiency. The branching fraction is calculated as

$$\mathcal{B} = \frac{N^{B^+}_{\text{yield}}/\epsilon^{+}_{\text{data}} + N^{B^-}_{\text{yield}}/\epsilon^{-}_{\text{data}}}{N^{0}_{B^+B^-}}, \tag{7.2}$$

where $N^{B^{\pm}}_{\text{yield}}$ and $\epsilon^{\pm}_{\text{data}}$ are the signal yield and efficiency, respectively; $N^{0}_{B^+B^-}$ is the number of charged $B\bar{B}$ pairs before decay, as in Section 6.4. The asymmetry $\mathcal{A}_{CP}$ is calculated as

$$\begin{aligned} \mathcal{A}_{CP} &= \frac{N^{B^-}_{\text{yield}}/\epsilon^{-}_{\text{data}} - N^{B^+}_{\text{yield}}/\epsilon^{+}_{\text{data}}}{N^{B^-}_{\text{yield}}/\epsilon^{-}_{\text{data}} + N^{B^+}_{\text{yield}}/\epsilon^{+}_{\text{data}}} \\ &= \frac{N^{B^-}_{\text{yield}}/\epsilon^{-}_{\text{MC}} - N^{B^+}_{\text{yield}}/\epsilon^{+}_{\text{MC}}}{N^{B^-}_{\text{yield}}/\epsilon^{-}_{\text{MC}} + N^{B^+}_{\text{yield}}/\epsilon^{+}_{\text{MC}}}. \end{aligned} \tag{7.3}$$

Table 7.3: Branching fraction and $\mathcal{A}_{CP}$ for $B^{\pm} \to \pi^{\pm}\pi^+\pi^-$

$\mathcal{B}(B^{\pm} \to \pi^{\pm}\pi^+\pi^-)$	$\left(18.9^{+5.1}_{-4.5}(\text{stat.}) \pm 1.7(\text{syst.})\right) \times 10^{-6}$
$\mathcal{A}_{CP}$	$-0.10^{+0.27}_{-0.24}(\text{stat.}) \pm 0.02(\text{syst.})$

The result of previous Belle analysis of with the same experiments 7 to 13 data set is $\mathcal{B}(B^{\pm} \to \rho^0\pi^{\pm}) = \left(8.0^{+2.3+0.7}_{-2.0-0.7}\right) \times 10^{-6}$ [61]. According to PDG [1], the branching fraction for $\mathcal{B}(B^{\pm} \to \pi^{\pm}\pi^+\pi^-) = \left(15.2 \pm 0.6^{+1.3}_{-1.2}\right) \times 10^{-6}$. The result of our analysis is consistent with those studies.

Appendices

Appendix A

Continuum Background Suppression: Study of Correlation among Variables

A.1 Correlations between klr, $\cos\theta_B$, Δz, and $q \cdot r$

To study the correlation between a pair of variables selected from klr, $\cos\theta_B$, Δz, and $q \cdot r$, we classify the events into 5 bins of one variable and then obtain the distribution of the other variable in each bin, as shown in FIGs A.1 to A.6. If they do not change significantly in the different ranges, these 2 variables are not correlated. The χ^2 between each normalized distributions and the normalized distribution among the whole range is close to 1 in each case. Therefore, we conclude that klr, $\cos\theta_B$, Δz, and $q \cdot r$ are uncorrelated to each other.

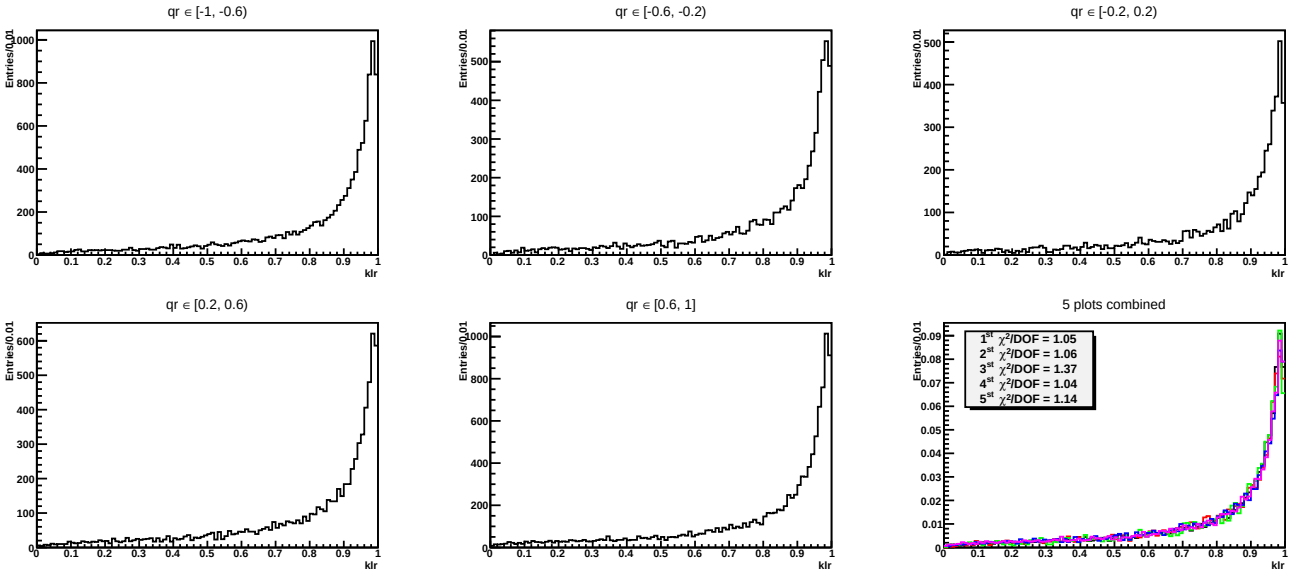

Figure A.1: The distributions of klr in 5 $q \cdot r$ ranges. The sixth figure shows the 5 normalized distributions combined. The χ^2 is calculated between each normalized distribution and the normalized distribution among the whole range.

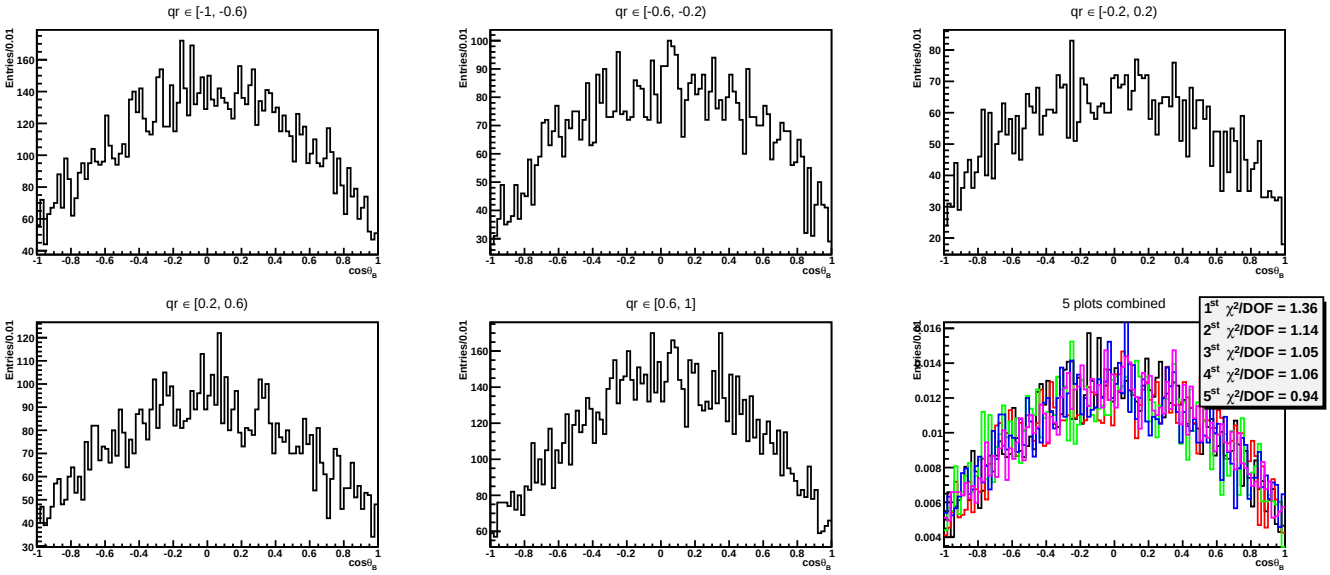

Figure A.2: The distributions of $\cos\theta_B$ in 5 $q \cdot r$ ranges. The sixth figure shows the 5 normalized distributions combined. The χ^2 is calculated between each normalized distribution and the normalized distribution among the whole range.

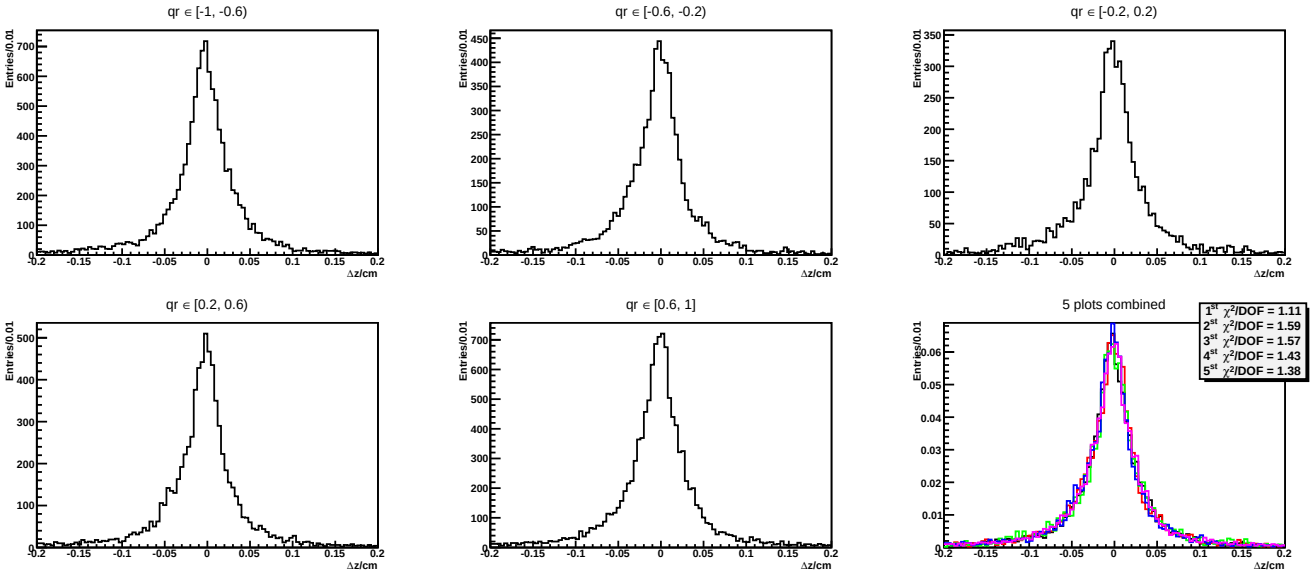

Figure A.3: The distributions of Δz in 5 $q \cdot r$ ranges. The sixth figure shows the 5 normalized distributions combined. The χ^2 is calculated between each normalized distribution and the normalized distribution among the whole range.

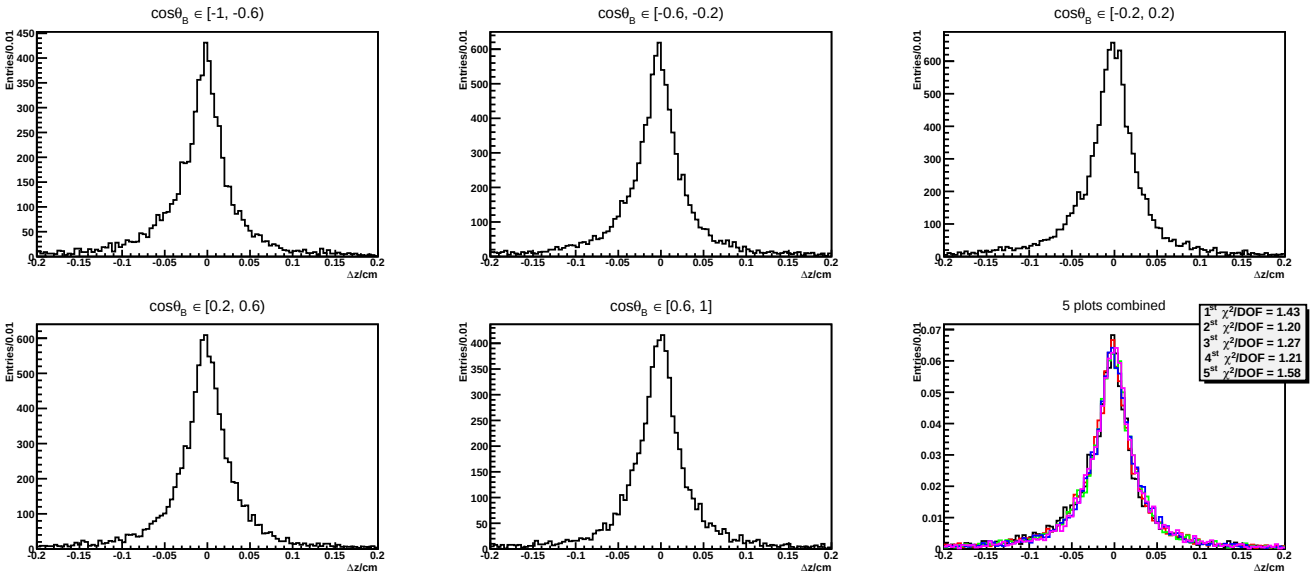

Figure A.4: The distributions of Δz in 5 $\cos\theta_B$ ranges. The sixth figure shows the 5 normalized distributions combined. The χ^2 is calculated between each normalized distribution and the normalized distribution among the whole range.

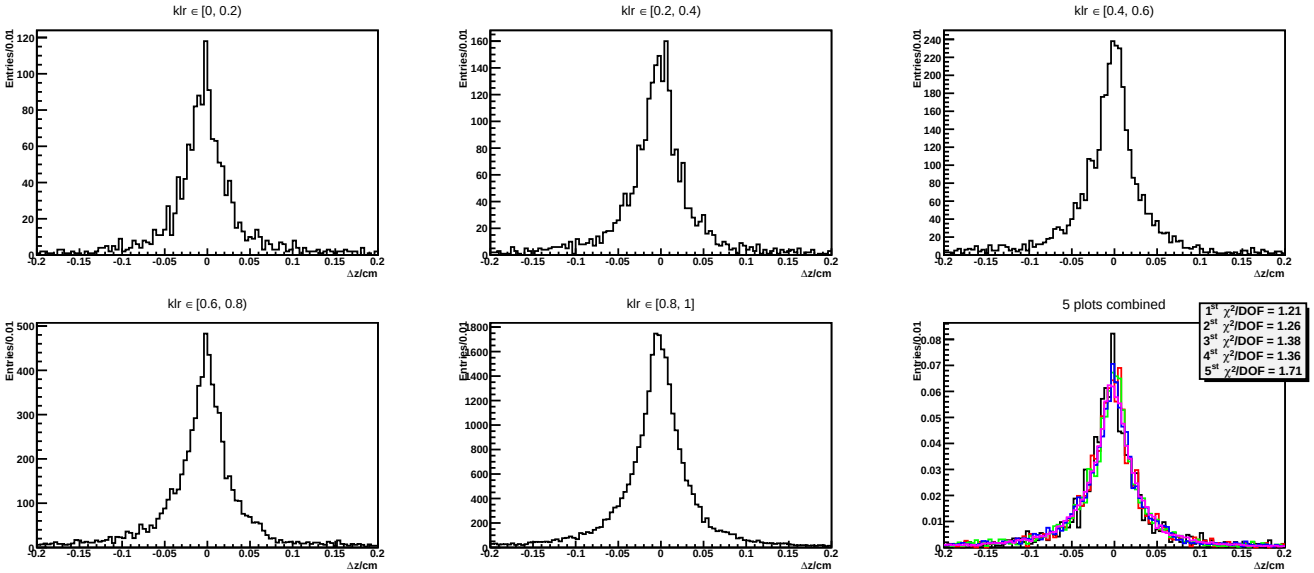

Figure A.5: The distributions of Δz in 5 klr ranges. The sixth figure shows the 5 normalized distributions combined. The χ^2 is calculated between each normalized distribution and the normalized distribution among the whole range.

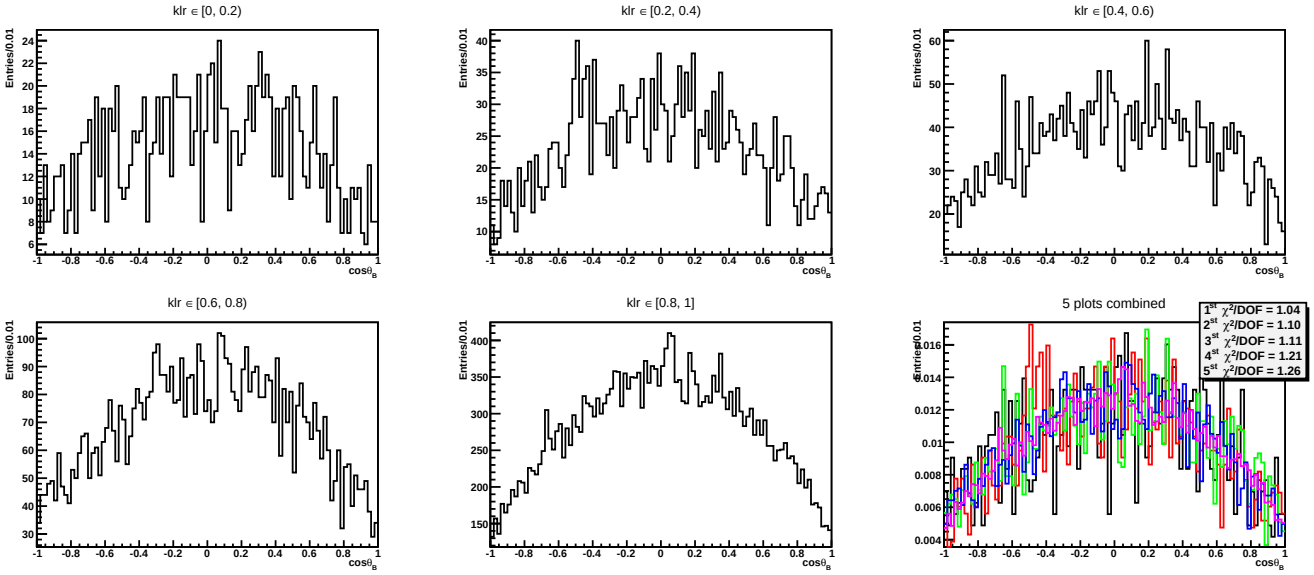

Figure A.6: The distribution of $\cos\theta_B$ in 5 klr ranges. The sixth figure shows the 5 normalized distributions combined. The χ^2 is calculated between each normalized distribution and the normalized distribution among the whole range.

A.2 Correlation between klr and $\cos\theta_T$

The correlation between klr and $\cos\theta_T$ is shown in FIG A.7. Again, we classify the events into 5 $\cos\theta_T$ bins and compare the klr distributions. As shown in FIG A.8, $\chi^2 \gg 1$ for each sub-range normalized klr distribution comparing with the normalized klr distribution in the whole range. Thus, there is strong correlation between klr and $\cos\theta_T$.

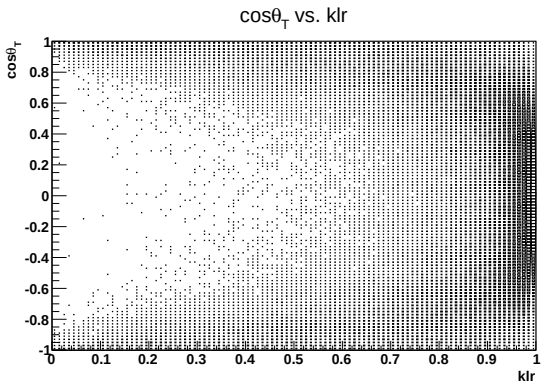

Figure A.7: The distribution of $\cos\theta_T$ vs. klr, , illustrating the strong correlation between these two measures.

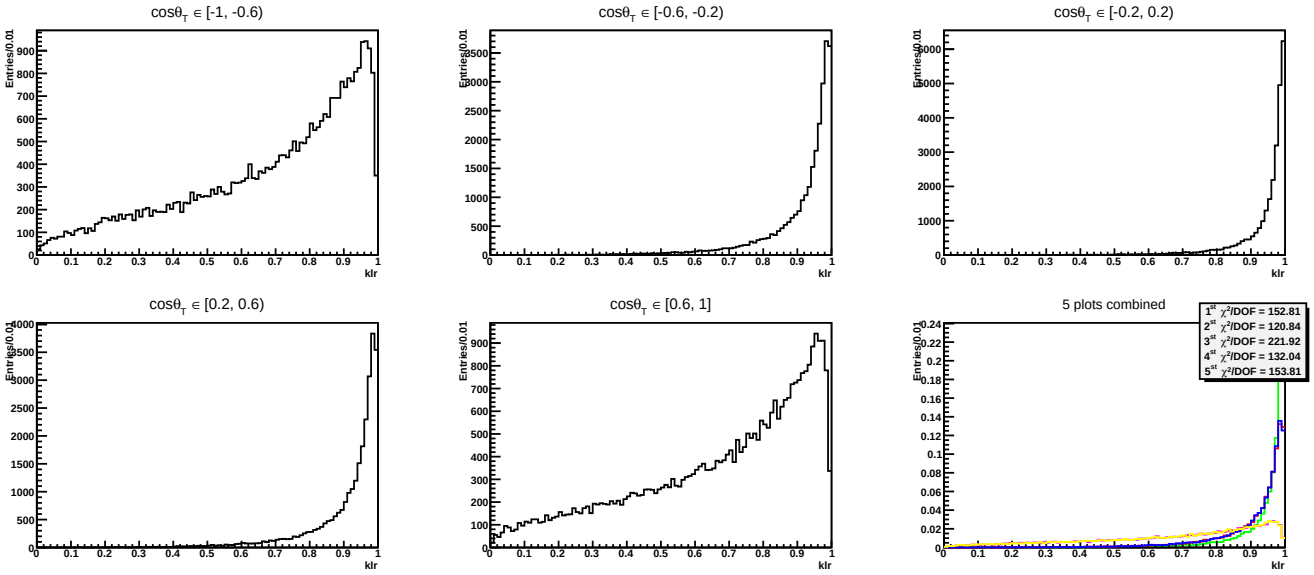

Figure A.8: The distribution of klr in 5 $\cos\theta_T$ ranges. The sixth figure shows the 5 normalized distributions combined. The χ^2 is calculated between each normalized distribution and the normalized distribution among the whole range.

Appendix B

$B\bar{B}$ Background PDFs

B.1 $B^{\pm} \to \bar{D}^0 h^{\pm}$

The distributions of Dalitz plot, M_{bc}, and ΔE for $B^{\pm} \to \bar{D}^0 h^{\pm}$ are shown in FIG B.1. The Dalitz plot can be divided into 4 parts: a horizontal $\pi\pi\pi$ band, a vertical $\pi\pi\pi$ band, a vertical $\pi\pi K$ band, and the other components including the curved band. The first 3 bands can be described by the product of the functions from the projections on m_{12}^2 and m_{23}^2 axis (as shown in FIG B.2 and B.3) since there is no correlation between m_{12}^2 and m_{23}^2. The fourth part can be described by RooHistPdf (PDF sampled from histogram), as shown in FIG B.3.

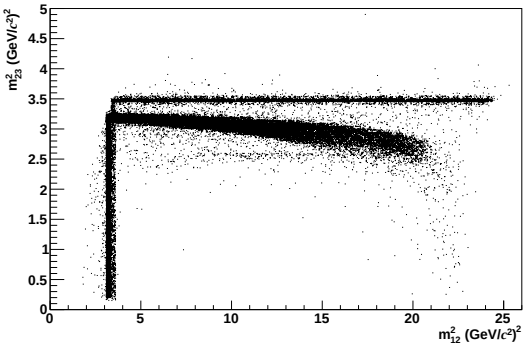

(a)

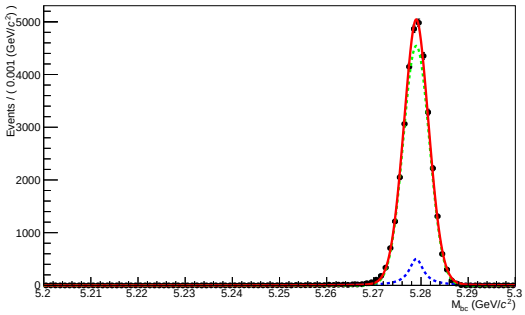

(b)

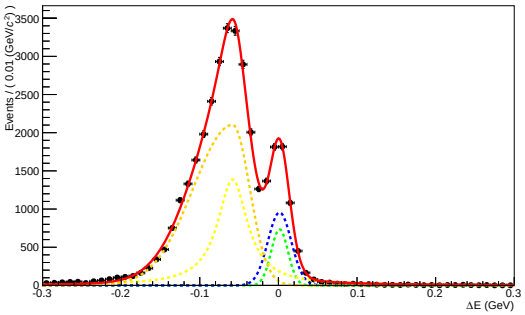

(c)

Figure B.1: $B^{\pm} \to \bar{D}^0 h^{\pm}$: (a) Dalitz plot; (b) M_{bc} and its fitting function; (c) ΔE and its fitting function.

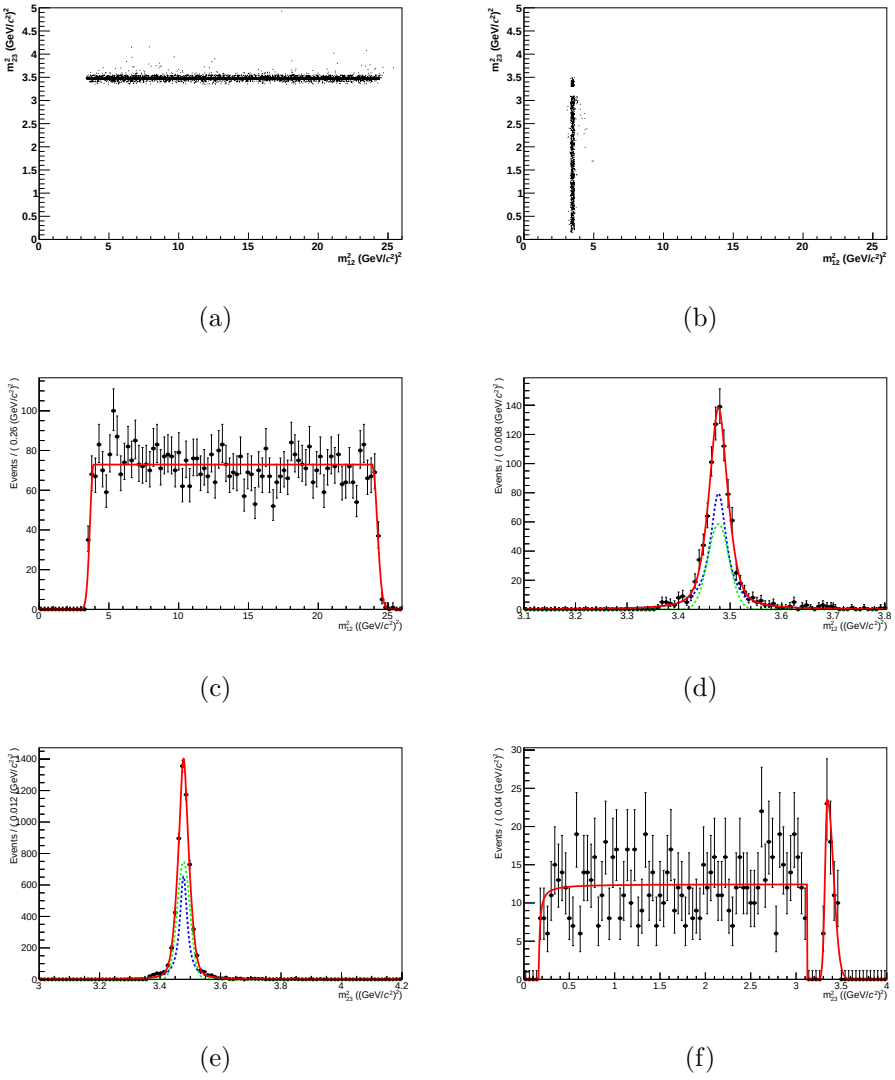

Figure B.2: $B^{\pm} \to \bar{D}^0 h^{\pm}$: (a) the horizontal $\pi\pi\pi$ band in the Dalitz plot; (b) the vertical $\pi\pi\pi$ band in the Dalitz plot, with the gap near the top of the band due to elimination of the crossing horizontal $\pi\pi K$ band; (c) the projection of the horizontal $\pi\pi\pi$ band on the m_{12}^2 axis and its fitting function; (d) the projection of the vertical $\pi\pi\pi$ band on the m_{12}^2 axis and its fitting function; (e) the projection of the horizontal $\pi\pi\pi$ band on the m_{23}^2 axis and its fitting function; (f) the projection of the vertical $\pi\pi\pi$ band on the m_{23}^2 axis and its fitting function.

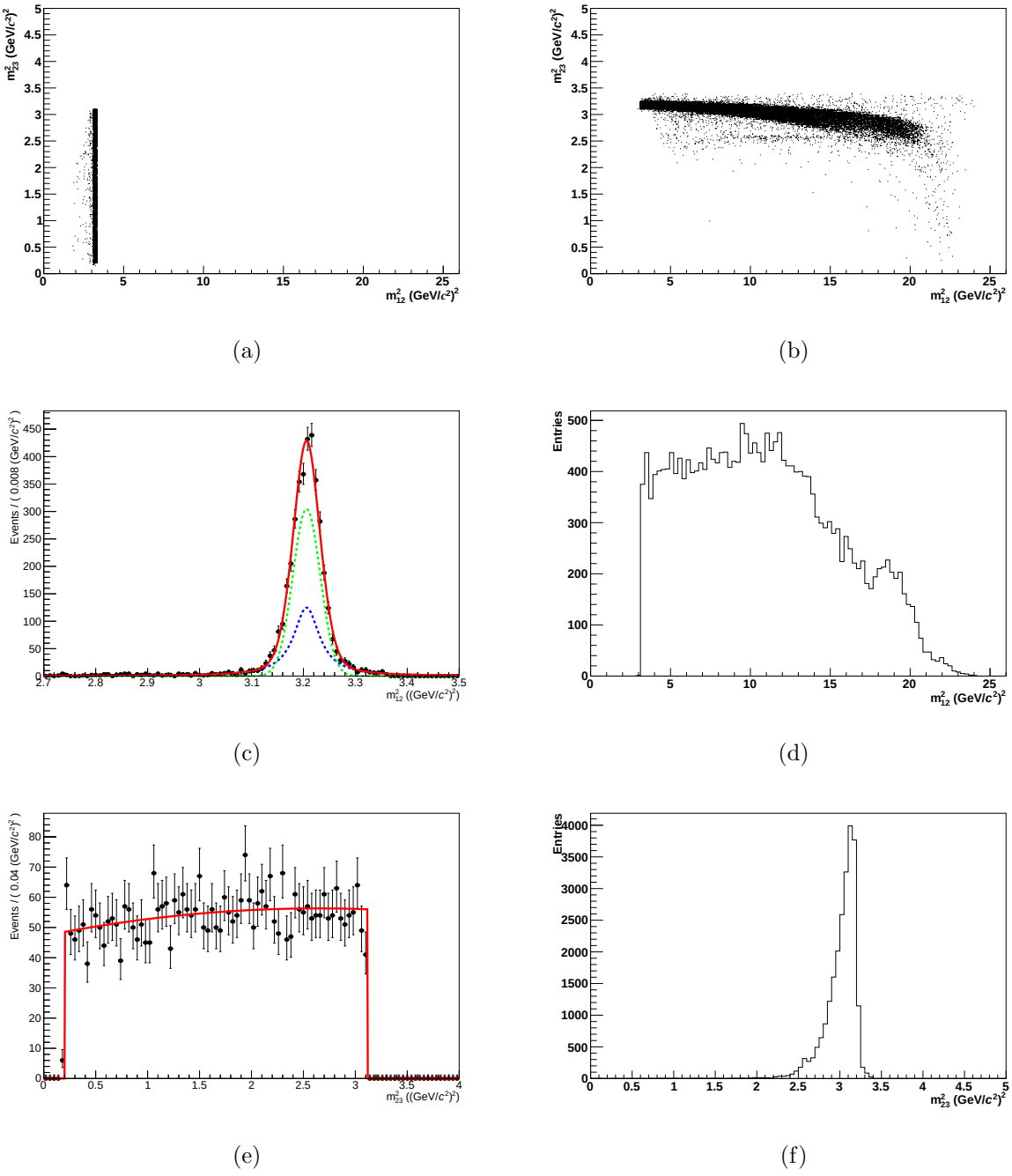

Figure B.3: $B^{\pm} \to \bar{D}^0 h^{\pm}$: (a) the vertical $\pi\pi K$ band in the Dalitz plot; (b) the other components in the Dalitz plot; (c) the projection of the $\pi\pi K$ vertical band on the m^2_{12} axis and its fitting function; (d) the other components projected on the m^2_{12} axis; (e) the projection of the $\pi\pi K$ vertical band on the m^2_{23} axis and its fitting function; (f) the other components projected on the m^2_{23} axis.

B.2 $B^{\pm} \to J/\psi h^{\pm}$

The distributions of Dalitz plot, M_{bc}, and ΔE for $B^{\pm} \to J/\psi h^{\pm}$ are shown in FIG B.4. The Dalitz plot can be divided into a horizontal band and a vertical band. Both bands can be described by the product of the functions from the projections on m_{12}^2 and m_{23}^2 axis as shown in FIG B.5 .

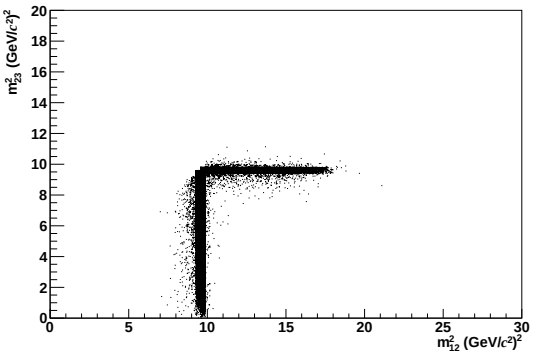

(a)

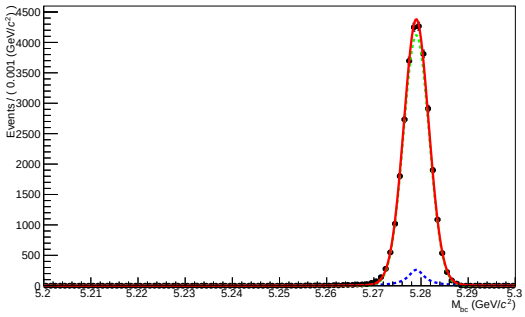

(b)

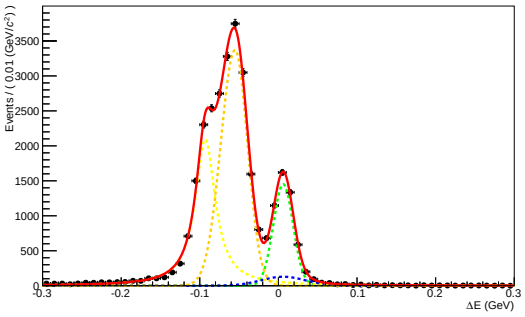

(c)

Figure B.4: $B^{\pm} \to J/\psi h^{\pm}$: (a) Dalitz plot; (b) M_{bc} and its fitting function; (c) ΔE and its fitting function.

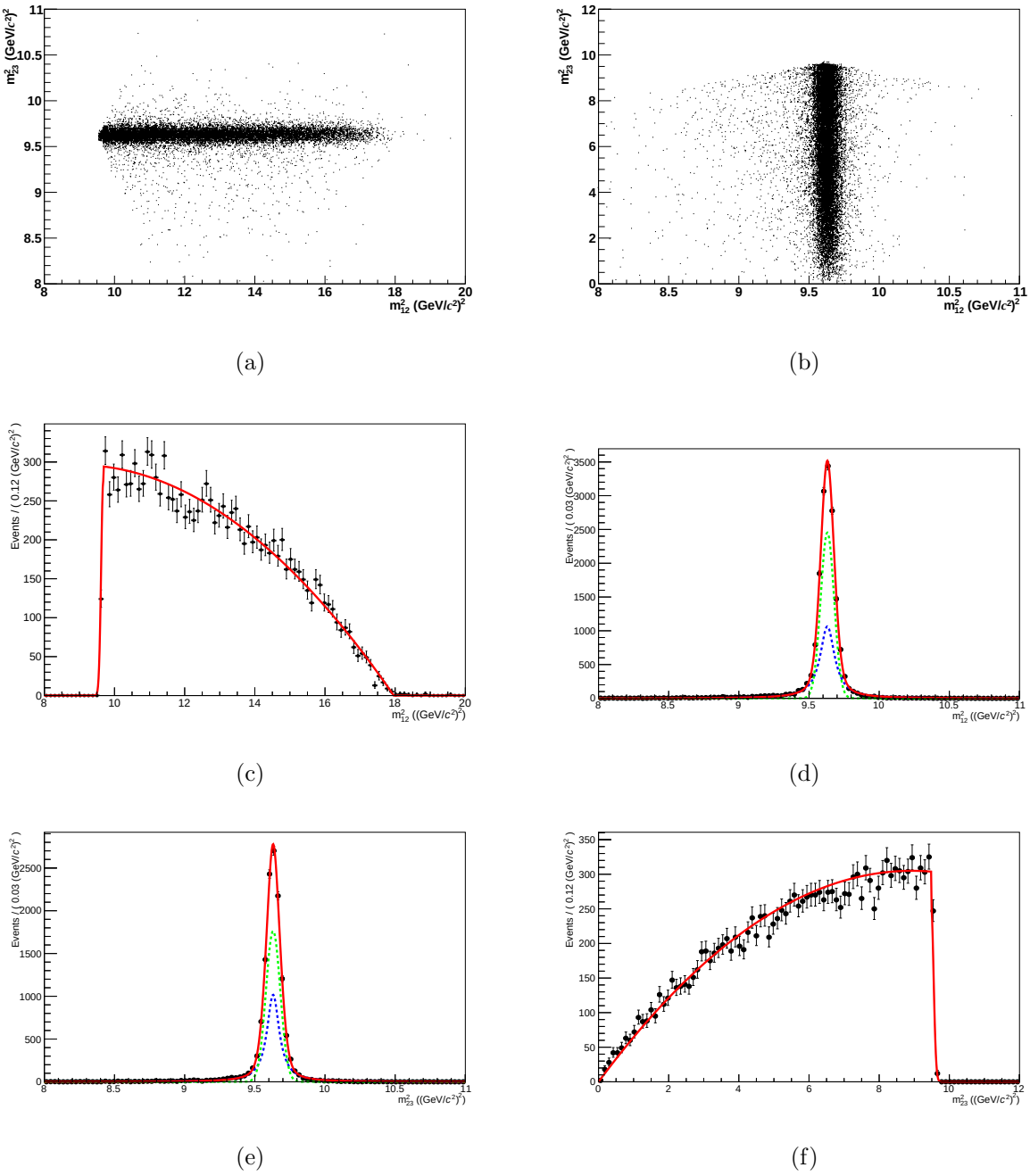

Figure B.5: $B^{\pm} \to J/\psi h^{\pm}$: (a) the horizontal band in the Dalitz plot; (b) the vertical band in the Dalitz plot; (c) the projection of the horizontal band on the m_{12}^2 axis and its fitting function; (d) the projection of the vertical band on the m_{12}^2 axis and its fitting function; (e) the projection of the horizontal band on the m_{23}^2 axis and its fitting function; (f) the projection of the vertical band on the m_{23}^2 axis and its fitting function.

B.3 $B^{\pm} \to \psi(2S)h^{\pm}$

The distributions of Dalitz plot, M_{bc}, and ΔE for $B^{\pm} \to \psi(2S)h^{\pm}$ are shown in FIG B.6. The Dalitz plot is a vertical band which can be described by the product of the functions from the projections on m_{12}^2 and m_{23}^2 axis.

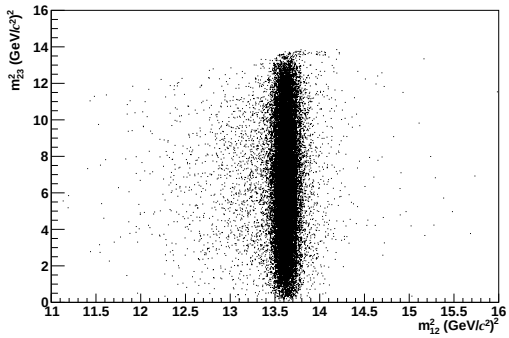

(a)

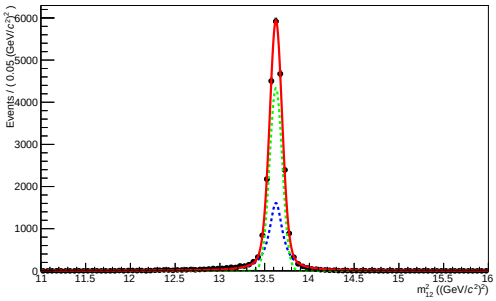

(b)

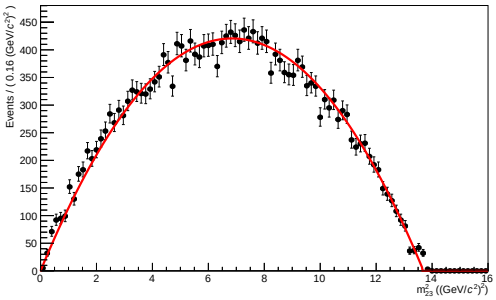

(c)

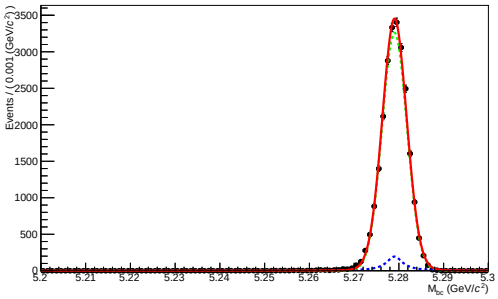

(d)

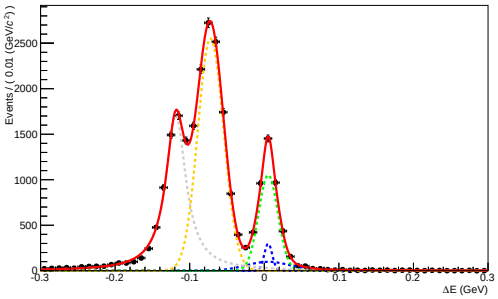

(e)

Figure B.6: $B^{\pm} \to \psi(2S)h^{\pm}$: (a) Dalitz plot; (b) projection on the m^2_{12} axis and its fitting function (a Gaussian and a Breit-Wigner function); (c) projection on the m^2_{23} axis and its fitting function (a piecewise quadratic polynomial); (d) M_{bc} and its fitting function; (e) ΔE and its fitting function.

B.4 $B^{\pm} \to K^0_S h^{\pm}$

The distributions of Dalitz plot, M_{bc}, and ΔE for $B^{\pm} \to K^0_S h^{\pm}$ are shown in FIG B.7. The Dalitz plot is a horizontal band which can be described by the product of the functions from the projections on m^2_{12} and m^2_{23} axis.

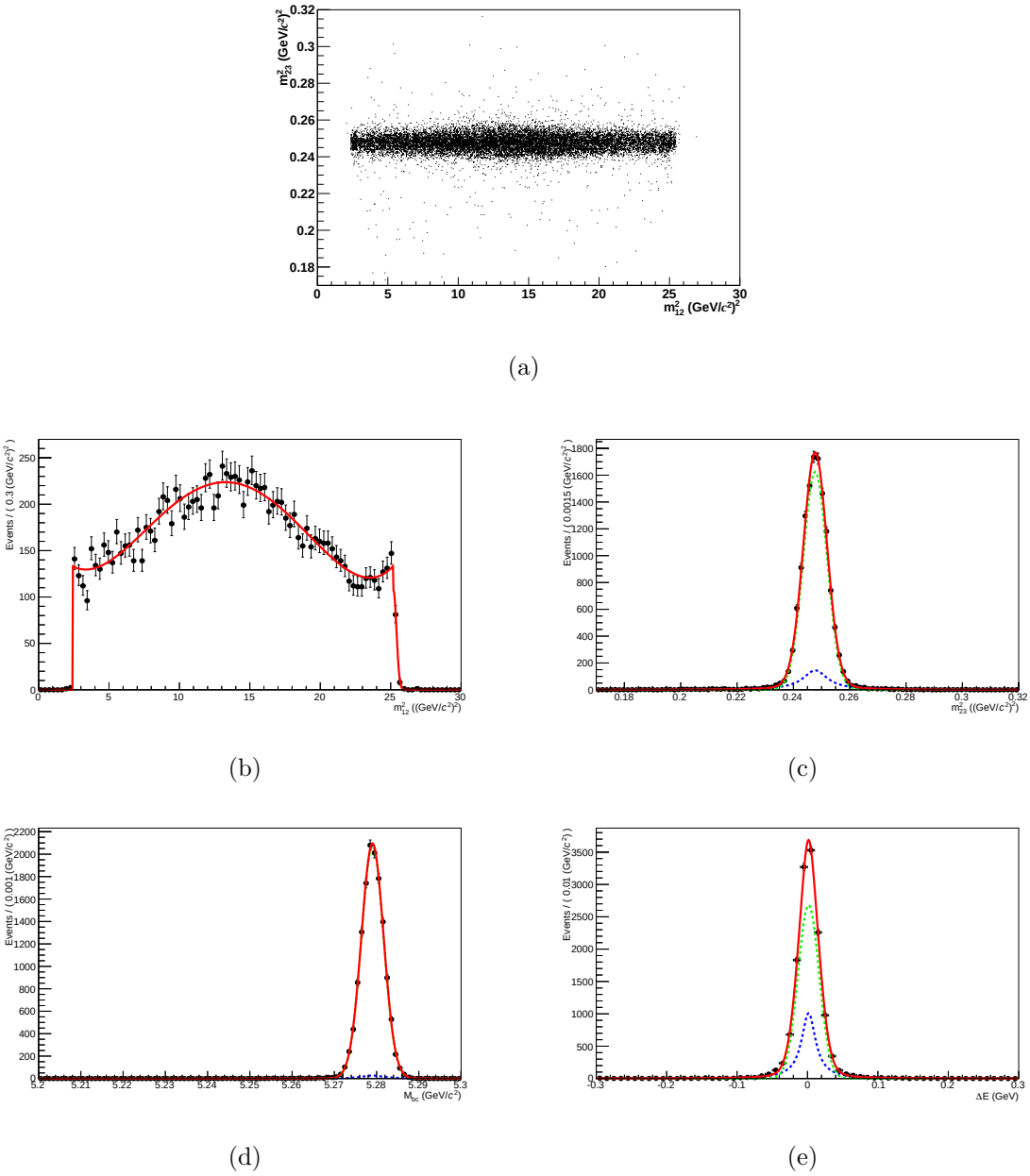

Figure B.7: (a) $B^{\pm} \to K^0_S h^{\pm}$ Dalitz plot; (b) projection on the m^2_{12} axis and its fitting function (a piecewise quartic polynomial); (c) projection on the m^2_{23} axis and its fitting function (a Gaussian and a Breit-Wigner function); (d) M_{bc} and its fitting function; (e) ΔE and its fitting function.

Appendix C

Rare B Background

There are 7 modes involved in charged rare B decay that have a peak at $\Delta E = 0$, as shown in FIG C.1. These modes are removed by hand from the charged rare B sample to avoid duplication of this component's PDF with that of the signal.

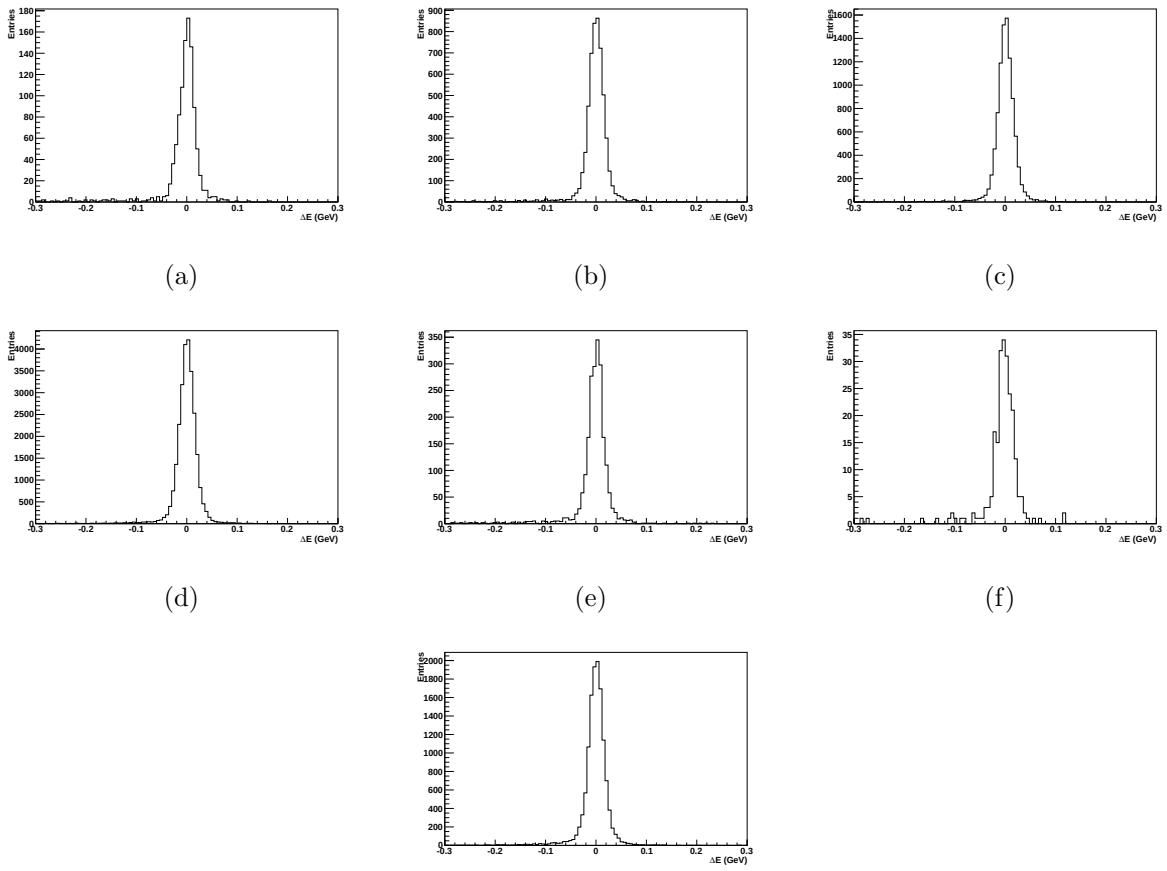

(a) (b) (c)

(d) (e) (f)

(g)

Figure C.1: ΔE distributions for some modes in charged rare B decay: (a) $f_0(1710)$, (b) $f_0(1370)$, (c) $f_0(600)$, (d) $\rho(770)^0$, (e) $\rho(1450)^0$, (f) $\rho(1700)^0$, (g) $f_2(1270)$.

Appendix D

Fitting Systematics

Parameter	-1σ (B^+)	+1σ (B^+)	-1σ (B^-)	+1σ (B^-)
chargedrare_mbc_mean1	-0.029%	0.028%	-0.006%	0.010%
chargedrare_mbc_mean2	-0.035%	0.087%	-0.107%	0.390%
chargedrare_mbc_widthL1	0.010%	-0.011%	-0.001%	0.002%
chargedrare_mbc_widthL2	0.106%	-0.049%	0.339%	-0.070%
chargedrare_mbc_widthR1	-0.010%	0.010%	0.003%	-0.006%
chargedrare_mbc_widthR2	-0.022%	0.049%	-0.096%	0.096%
n_chargedrare_mbc_bigauss1	-0.009%	0.006%	-0.024%	0.024%
n_chargedrare_mbc_bigauss2	0.003%	-0.004%	0.011%	-0.010%
chargedrare_de_bw_width	0.000%	0.000%	0.000%	0.000%
chargedrare_de_g_width	0.000%	0.000%	0.000%	0.000%
chargedrare_de_mean	0.000%	0.000%	0.000%	0.000%
chargedrare_de_mean1	0.078%	-0.033%	0.465%	-0.191%
chargedrare_de_mean2	-0.011%	0.034%	0.177%	-0.179%
chargedrare_de_mean3	0.162%	-0.131%	1.446%	-1.406%
chargedrare_de_width2	-0.041%	0.038%	0.310%	-0.076%
chargedrare_de_width3	0.142%	-0.099%	0.803%	-0.696%
chargedrare_de_widthR1	0.105%	-0.056%	0.800%	-0.529%
n_chargedrare_de_bigauss1	-0.062%	0.087%	-0.507%	0.648%
n_chargedrare_de_bw	0.000%	0.000%	0.000%	0.000%
n_chargedrare_de_g	0.000%	0.000%	0.000%	0.000%
n_chargedrare_de_gauss2	0.024%	-0.023%	0.222%	0.043%
n_chargedrare_de_gauss3	0.012%	-0.003%	0.577%	-0.238%

Figure D.1: Change of signal yield caused by floating fit parameters for charged rare B PDFs by 1σ.

Parameter	-1σ (B^+)	+1σ (B^+)	-1σ (B^-)	+1σ (B^-)
mixedrare_mbc_argk	0.023%	0.039%	-0.007%	0.008%
mixedrare_mbc_argpar	0.059%	0.127%	0.037%	0.162%
mixedrare_mbc_mean	0.050%	0.000%	0.014%	0.018%
mixedrare_mbc_mean1	-0.019%	0.093%	-0.024%	0.026%
mixedrare_mbc_mean2	0.086%	-0.045%	0.077%	-0.067%
mixedrare_mbc_mean3	-0.034%	0.145%	0.194%	0.038%
mixedrare_mbc_width	0.002%	0.028%	0.140%	0.058%
mixedrare_mbc_width2	-0.018%	0.083%	-0.009%	0.022%
mixedrare_mbc_width3	-0.073%	0.064%	0.101%	0.008%
mixedrare_mbc_widthL1	-0.164%	0.218%	-0.172%	0.143%
mixedrare_mbc_widthR1	-0.057%	0.072%	-0.023%	0.023%
n_mixedrare_mbc_argus	-0.099%	0.116%	0.158%	0.069%
n_mixedrare_mbc_bigauss1	0.151%	-0.062%	0.048%	-0.042%
n_mixedrare_mbc_bw	0.112%	-0.015%	0.217%	-0.187%
n_mixedrare_mbc_bw2	0.110%	-0.037%	0.031%	-0.029%
n_mixedrare_mbc_bw3	0.094%	0.060%	0.061%	-0.022%
mixedrare_de_mean1	0.023%	0.008%	0.023%	0.267%
mixedrare_de_mean2	0.003%	0.032%	0.000%	0.000%
mixedrare_de_mean3	0.101%	0.022%	0.160%	-0.028%
mixedrare_de_mean4	-0.011%	0.060%	-0.041%	0.046%
mixedrare_de_mean5	0.001%	0.027%	0.227%	0.031%
mixedrare_de_n1	-0.594%	0.613%	-0.225%	0.298%
mixedrare_de_n2	-0.039%	0.070%	0.271%	0.029%
mixedrare_de_n3	1.055%	-0.895%	0.753%	-0.561%
mixedrare_de_n4	-0.571%	1.082%	-0.390%	0.470%
mixedrare_de_n5	-0.659%	0.704%	-0.507%	0.691%
mixedrare_de_width1	0.152%	-0.113%	0.155%	0.001%
mixedrare_de_width2	-0.041%	0.034%	0.001%	-0.002%
mixedrare_de_width3	-2.703%	1.632%	-1.814%	1.390%
mixedrare_de_width4	-0.082%	0.174%	0.113%	0.168%
mixedrare_de_width5	0.090%	-0.012%	0.020%	-0.011%

Figure D.2: Change of signal yield caused by floating fit parameters for neutral rare B PDFs by 1σ.

Bibliography

[1] K. A. Olive *et al.* (Particle Data Group). 2014 Review of Particle Physics. *Chin. Phys. C*, 38, 090001, (2014).

[2] N. Cabibbo. Unitary Symmetry and Leptonic Decays. *Phys. Rev. Lett.*, 10, 531, (1963).

[3] M. Kobayashi and T. Maskawa. CP-Violation in the Renormalizable Theory of Weak Interaction. *Prog. Theor. Phys.*, 49, 652, (1973).

[4] L.L. Chau and W.Y. Keung. Comments on the Parametrization of the Kobayashi-Maskawa Matrix. *Phys. Rev. Lett.*, 53, 1802, (1984).

[5] L. Wolfenstein. Parametrization of the Kobayashi-Maskawa Matrix. *Phys. Rev. Lett.*, 51, 1945, (1983).

[6] A.J. Buras *et al.* Waiting for the Top Quark Mass, $K^+ \to {}^+\nu\bar{\nu}$, $B_s^0 - \bar{B}_s^0$ Mixing and CP Asymmetries in B-Decays. *Phys. Rev. D*, 50, 3433, (1994).

[7] J. Charles *et al.* (CKMfitter Group). CP Violation and the CKM Matrix: Assessing the Impact of the Asymmetric B Factories. *Eur. Phys. J. C*, 41, 1, (2005).

[8] A. Hocker *et al.* A New Approach to a Global Fit of the CKM Matrix. *Eur. Phys. J.*, C21, 225, (2001).

[9] G.P. Dubois-Felsmann *et al.* Sensitivity of CKM Fits to Theoretical Uncertainties and Their Representation. *hep-ph/0308262*, (2003).

[10] M. Bona *et al.* (UTfit Collaboration). The 2004 UTfit Collaboration Report on the Status of the Unitarity Triangle in the Standard Model. *JHEP*, 507, 28, (2005).

[11] M. Bona *et al.* Model-independent Constraints on Delta F=2 Operators and the Scale of New Physics. *JHEP*, 0803, 049, (2008).

[12] B. Aubert *et al.* Dalitz Plot Analysis of $B^{\pm} \to \pi^{\pm}\pi^{\pm}\pi^{\mp}$ Decays. *Phys. Rev. D*, 79, 072006, (2009).

[13] D. Schroeder M. Peskin. *An Introduction to Quantum Field Theory.* Westview Press, (1995).

[14] Ian J.R. Aitchison *et al.* The Scientific Heritage of Richard Henry Dalitz, FRS (1925-2006). *Nucl.Phys. A771*, 8-25, (2006).

[15] A. Abashian *et al.* The Belle Detector. *Nucl. Instr. Meth. A*, 479:117, (2002).

[16] D. Mohapatra. Observation of $b \to d\gamma$ Decays and Determination of $|V_{td}/V_{ts}|$. *PhD Thesis, Virginia Tech*, (2006).

[17] N. Satoyama. A Search for the Rare Leptonic Decays $B^+ \to \mu^+\nu_\mu$ and $B^+ \to e^+\nu_e$. *PhD Thesis, Shinshu University, Japan*, (2007).

[18] K. Vervink. Measurement of the C P -odd fraction and time-dependent CP violation in the decay $B^0 \to D^{*+}D^{*-}$ at Belle. *PhD Thesis, Universiteit Antwerpen, Belgique*, (2008).

[19] CFS Collaboration. Observation of a Dimuon Resonance at 9.5 GeV in 400-GeV Proton-Nucleus Collision. *Phys. Rev. Lett.*, 39(5):252-255, (1977).

[20] J. P. Alexander *et al.* Measurement of the Relative Branching Fraction of Upsilon(4S) to Charged and Neutral B Meson Pairs. *Phys. Rev. Lett.*, 86 (2737-2741), (2001).

[21] H. Ha *et al.* Trigger Summary Experiment 63 and Experiment 65. *Belle Note*, 1064, (2009).

[22] S. Kurokawa and E. Kikutani. Overview of the KEKB Accelerators. *Nucl. Instr. Meth. A*, 499, (2003).

[23] KEKB. Machine Parameters of the KEKB. `http://www-acc.kek.jp/KEKB/Commissioning/Machine%20param%202009Jun17.pdf`, (2009).

[24] D. Zhou *et al.* Simulations of beam-beam effect in the presence of general chromaticity. *Physical Review Special Topics*, 13, 021001, (2010).

[25] KEKB. Luminosity of KEKB Oct. 1999 - June 2010. `http://www-acc.kek.jp/kekb/History/KEKB_History.html`, (2010).

[26] K. Hosoyama *et al.* Development of the KEK-B Superconducting Crab Cavity. *11th European Particle Accelerator Conference*, pp.THXM02, (2008).

[27] S. Hashimoto *et al.* Letter of intent for KEK Super B Factory. *KEK-REPORT-2004-4*, (2004).

[28] N. Koch *et al.* The ARGUS Vertex Trigger. *Nucl. Instrum. Meth. A*, 373, (1996).

[29] H. Yasuyuki. First Evidence of the Suppressed B Meson Decay $B^- \to DK^-$ Followed by $D \to K^+\pi^-$ and Extraction of the CP-Violating Angle ϕ_3. *PhD Thesis, Tohoku University, Japan*, (2010).

[30] H. Aihara. The Belle Silicon Vertex Detector. *Nucl. Instrum. Meth. A*, 466, 268, (2001).

[31] O. Nitoh *et al.* Drift Velocity of Electrons in Helium-Based Gas Mixtures Measured with a UV Laser. *Jpn. J. Appl. Phys.*, 33, 5929, (1994).

[32] H. Hirano *et al.* A High Resolution Cylindrical Drift Chamber for the KEK B-Factory. *Nucl. Instrum. Meth. A*, 455, 294, (2000).

[33] T. Sumiyoshi *et al.* Silica Aerogel Cherenkov Counter for the KEK B-Factory Experiment. *Nucl. Instrum. Meth. A*, 433, 385, (1999).

[34] T. Iijima *et al.* Aerogel Cherenkov Counter for the Belle Detector. *Nucl. Instrum. Meth. A*, 453, 321, (2000).

[35] H. Kichimi *et al.* The Belle TOF System. *Nucl. Instrum. Meth. A*, 453, 315, (2000).

[36] A. Abashian *et al.* The K_L /μ Detector Subsystem for the Belle Experiment at the KEKB Factory. *Nucl. Instrum. Meth. A*, 449, 112, (2000).

[37] L. Antoiazzi *et al.* The E771 RPC Muon Detector. *Nucl. Instrum. Meth. A*, 307, 312, (1991).

[38] Y. Ushiroda *et al.* Development of the Central Trigger System for the Belle Detector at the KEK B-factory. *Nucl. Instr. and Meth. A*, 438, 460, (1999).

[39] M. Tomoto *et al.* Z-Trigger System with the Belle Central Drift Chamber. *Nucl. Instrum. Meth. A*, 447, 416-423, (2000).

[40] H. Ikeda *et al.* A Study of the Electromagnetic Calorimeter Trigger Signal for the Belle Experiment. *Journal of the Korean Physical Society*, 50, 1224-1228, (2007).

[41] S. Nishida. Trigger Efficiency. *Belle Note*, 350, 381, 423, 459, 504, 520, 548, 584, (2000-2002).

[42] H. Kakuno *et al.* Level 4 Software Trigger at Belle. *Belle Note*, 299, (2000).

[43] M. Nakao *et al.* Data Acquisition System for the Belle Experiment. *IEEE Trans. Nucl. Sci.*, 47, 5660, (2000).

[44] Ed. A.J. Bevan *et al.* The Physics of B Factories. *submitted to EPJC, SLAC-PUB-15968, KEK Preprint 2014-3*, (2014).

[45] S. Nagayama. PANTHER - Users Manual, Reference Manual and Primer. *Belle Note*, 132, (1996).

[46] B. Casey. HadronB. *Belle Note*, 390, (2001).

[47] R. Itoh. BASF User's Manual. *Belle Note*, 161, (1997).

[48] CLHEP. A Class Library for High Energy Physics. `http://proj-clhep.web.cern.ch/proj-clhep/`, (2015).

[49] CLEO. QQ Documentation Sources. `http://www.lns.cornell.edu/public/CLEO/soft/QQ/`, (1998).

[50] . The EvtGen Package. `http://www.slac.stanford.edu/~lange/EvtGen/`, (2003).

[51] M. Nakao and N. Katayama. Cabs3 User's Manual. *Belle Note*, 991, (2007).

[52] G. Fox and S. Wolfram. Observables for the Analysis of Event Shapes in e^+e^- Annihilation and Other Processes. *Phys. Rev. Lett.*, 41, 1581, (1978).

[53] K. Abe *et al.* Measurement of Branching Fractions for $B \to \pi\pi$, $K\pi$, and KK Decays. *Phys. Rev. Lett.*, 87, 101801, (2001).

[54] G. Breit and E. Wigner. Capture of Slow Neutrons. *Phys. Rev. 49*, 519, (1936).

[55] ARGUS collaboration H. Albrecht *et al.* Measurement of the polarization in the decay $B \to J/\psi K*$. *Phys. Lett. B*, 340,3, (1994).

[56] I. Dunietz *et al.* How to extract CP-violating asymmetries from angular correlations. *Phys. Rev. D*, 43, 2193, (1991).

[57] S.Nishida. Study of Kaon and Pion Identification Using Inclusive D^* Sample. *Belle Note*, 779, (2005).

[58] H. Hamasaki *et al* (KID group). Kaon Identification in Belle. *Belle Note*, 321, (2000).

[59] L. Hinz *et al.* Lepton ID efficiency correction and systematic error. *Belle Note*, 954, (2006).

[60] K. Hanagaki *et al.* Electron identification in Belle. *Nucl. Instrum. Meth. A*, 485,490, (2002).

[61] A. Gordon *et al.* Search for three-body B meson decays with pion final states at Belle. *Belle Note*, 484, (2002).

[62] B. Bhuyan. High P_T Tracking Efficiency Using Partially Reconstructed D^* Decays. *Belle Note*, 1165, (2010).